University of Southampton Research Repository

UNIVERSITY OF SOUTHAMPTON

FACULTY OF PHYSICAL SCIENCE AND ENGINEERING

Electronics and Computer Science
Nano Research Group

Ytterbium doped tantalum pentoxide nanowire waveguide lasers

by

Xingzhao Yan

A thesis submitted for PhD

June 2017

UNIVERSITY OF SOUTHAMPTON

ABSTRACT

FACULTY OF PHYSICAL SCIENCE AND ENGINEERING
Electronics and Computer Science

A thesis submitted for PhD

YTTERBIUM DOPED TANTALUM PENTOXIDE NANOWIRE WAVEGUIDE LASERS

By Xingzhao Yan

Ytterbium (Yb) has been widely studied in several host materials and device forms due to its broad gain bandwidth, long excited-state lifetime, and simple quasi-three energy level structure. Yb doped tantalum pentoxide (Yb:Ta_2O_5) waveguides are favorable for laser applications since Ta_2O_5 has promising optical properties including high refractive index (≈2.1), wide transmission spectrum (350 nm to 9 µm) and suitability to host rare-earth ions.

In this work, a nanowire waveguide design with taper and coupler section was demonstrated. Thin Yb:Ta_2O_5 films were fabricated by plasma assisted reactive magnetron sputtering (PARMS) from high purity (99.999%) Ta metal and Yb metal targets at low temperature (< 70°C). The PARMS process allows Yb doping concentration to be easily adjusted, leading to a new flexible deposition method for not only Yb:Ta_2O_5 but other doped materials.

Nanoscale waveguide fabrication processes of strip loaded and buried channel waveguides on SiO_2 using electron beam lithography and inductively couple plasma reactive ion etching (RIE-ICP) were demonstrated and the first Yb:Ta_2O_5 anisotropic RIE-ICP etching process was developed. Buried channel waveguide in polymer fabricated by nano-imprint was also demonstrated, offering low-cost and mass production of nanoscale waveguide.

A 6.7 mm long strip loaded Yb:Ta_2O_5 nanowire waveguide laser with 1.25 atomic percentage Yb doping concentration was demonstrated with a laser cavity formed of bare polished end facets only, with 12% Fresnel reflectivity. Single mode lasing was observed between 1015 nm and 1030 nm in strip loaded waveguides with nanowire of 400 nm width when end pumped by a 977 nm laser diode. The launched power threshold and the slope efficiency were measured to be ≈ 12 mW and ≈ 38%. The lasing wavelength of such waveguide can be switched by tuning the pump coupling position at the coupler section, implying a potential tuning mechanism.

The results presented in this work demonstrate the capability of Yb:Ta_2O_5 for being a waveguide laser, show the great potential for being used in mass-producible, CMOS compatible integrated optical circuits.

List of Publications

Journal Publications

Xingzhao Yan, Stuart J. Pearce, Armen Aghajani, James S. Wilkinson and Martin D. B. Charlton, "*Ytterbium doped tantalum pentoxide nanowire waveguide laser fabricated by CMOS compatible process*", Optica (in submission process).

Nikolaos Matthaiakakis, Xingzhao Yan, Hiroshi Mizuta and Martin D. B. Charlton, "*Tuneable Strong Optical Absorption in A Graphene Based Triply Resonant Plasmonic Device*", Scientific Report (under review), (2017).

Ruomeng Huang, Xingzhao Yan, Sheng Ye, Reza Kashtiban, Richard Beanland, Katrina A. Morgan, Martin D. B. Charlton and C. H. (Kees) de Groot, "*Compliance-Free $ZrO_2/ZrO_{2-x}/ZrO_2$ Resistive Memory with Controllable Interfacial Multistate Switching Behaviour*", Nanoscale Research Letters **12**:384 (2017).

Ruomeng Huang, Xingzhao Yan, Katrina A Morgan, Martin D. B. Charlton and C H (Kees) de Groot, "*Selection by current compliance of negative and positive bipolar resistive switching behaviour in ZrO_{2-x}/ZrO_2 bilayer memory*", J. Phys. D: Appl. Phys. **50** 175101 (2017).

Conference Publications

Xingzhao Yan, Stuart J. Pearce, James S. Wilkinson and Martin D. B. Charlton, "*Anisotropic Etching of Yb-doped Ta_2O_5 channel Waveguide Laser Device*", 42th Micro and Nano Engineering, Vienna, 19-23 September 2016.

Ruomeng Huang, Xingzhao Yan, Reza Kashitiban, Richard Beanland, Katrina A Morgan, Martin D. B. Charlton and C H (Kees) de Groot, "*Switching behaviour of ZrOx-based bi-layer and tri-layer resistive memory*", Non-Volatile Memory Technology Symposium, Aachen, Germany, 30 August 2017 (submitted).

Ruomeng Huang, Xingzhao Yan, Katrina A. Morgan, Martin D. B. Charlton, C H (Kees) de Groot, "*Tuneable ZrOx resistive memory with multistate switching behaviour*", 42th Micro and Nano Engineering, Vienna, Austria, 19-23 September 2016.

Xingzhao Yan, Stuart J. Pearce and Martin D. B. Charlton, "*Rare earth doped up/down conversion waveguide laser*", UK-Japan Si Nanoelectronics and Nanotechnology Symposium, Southampton, UK, 9-10 July 2015.

Table of Contents

Chapter 5: Yb:Ta_2O_5 Thin Film Properties 89

Chapter 6: Yb:Ta_2O_5 Strip Loaded Nanowire Waveguide Laser on Silicon 101

List of Tables

List of Figures

Declaration of Authorship

I, Xingzhao Yan declare that this thesis entitled "*Ytterbium doped tantalum pentoxide nanowire waveguide lasers*" and the work presented in it are my own and has been generated by me as the result of my own original research.

I confirm that:

1. This work was done wholly or mainly while in candidature for a research degree at this University;
2. Where any part of this thesis has previously been submitted for a degree or any other qualification at this University or any other institution, this has been clearly stated;
3. Where I have consulted the published work of others, this is always clearly attributed;
4. Where I have quoted from the work of others, the source is always given. With the exception of such quotations, this thesis is entirely my own work;
5. I have acknowledged all main sources of help;
6. Where the thesis is based on work done by myself jointly with others, I have made clear exactly what was done by others and what I have contributed myself;
7. Parts of this work have been published as: [please list references below]:
    A. Xingzhao Yan, Stuart J. Pearce, James S. Wilkinson and Martin D. B. Charlton, "Anisotropic Etching of Yb-doped Ta2O5 channel Waveguide Laser Device", 42th Micro and Nano Engineering, Vienna, 19-23 September 2016.
    B. Xingzhao Yan, Stuart J. Pearce and Martin D. B. Charlton, "Rare earth doped up/down conversion waveguide laser", UK-Japan Si Nanoelectronics and Nanotechnology Symposium, Southampton, UK, 9-10 July 2015.

Signed:

Date:

Acknowledgements

I would like to begin by my thanking my supervisor, Martin D B Charlton, Stuart J Pearce and James S Wilkinson for being a fantastic mentor and giving me this opportunity to work on this fascinating project. Without your help and guidance, my PhD could not have happened.

I would like to show my appreciation to my colleagues Ruiqi Chen, Michael Pollard and M. Firdaus Abdul Muttablib for their helps and comments. You taught me a lot useful skills about fabrication and laboratory experiment.

I would like to extend my gratitude to Nikolaos Matthaiakakis, Chirenjeevi Krishnan and Jingxing Shi for useful discussions about my project.

Finally, I would like to thank my wife and my parents for giving me the tremendous support during my life and giving me the drive to succeed during the good and bad times.

Definitions and Abbreviations

Al	Aluminium
As	Arsenic
ASE	Amplified spontaneous emission
Ce	Cerium
CMOS	Complementary metal-oxide-semiconductor
Co	Cobalt
Cr	Chromium
CW	Continuous wave
DBR	Distributed Bragg reflector
DFB	Distributed feedback
DI	De-ionized
E-beam	Electron ebeam
EDFA	Erbium doped fibre amplifier
EDWA	Erbium doped waveguide amplifier
EM	Electromagnetic
Er	Erbium
ESA	Excited state absorption
FDTD	Finite-difference time-domain
Fe	Iron
FNA	Fuming nitride acid
FWHM	Full width half maximum
FWM	Four wave mixing
FP	Fabry-Perot

GaAs	Gallium Arsenide
Ga	Gallium
GdCOB	Gadolinium Calcium Oxoborate
GGG	Gadolinium gallium garnet
GSGG	Gadolinium scandium aluminium garnet
HeNe	Helium Neon
Ho	Holmium
In	Indium
InGaAs	Indium gallium arsenide
InP	Indium Phosphide
IOG10	Alkali-zinc-silicate glass
IPA	Isopropanol alcohol
KGW	Potassium Gadolinium Tungstate
KYW	Potassium Yttrium Tungstate
LPE	Liquid phase epitaxy
Nd	Neodymium
Nd: YAG	Neodymium doped yttrium aluminium garnet
N-doped	Phosphorus doped
OC	Output coupler
OMS	Optical monitoring system
OPD	Optical path difference
P	Phosphor
PARMS	Plasma assisted reactive magnetron sputtering
PL	Photoluminescence

Pr	Prasesodymium
RIE-ICP	Inductively coupled plasma reactive ion etching
RE	Rare earth
RF	Radio frequency
RPM	Round per minute
sccm	Standard cubic centimetre per minute
Ti	Titanium
Ti: Sapphire	Titanium doped sapphire
Tm	Thulium
ULI	Ultrafast laser inscription
XPM	Cross phase modulation
XPS	X-ray photoelectron spectroscopy
Ta_2O_5	Tantalum penxoxide
YAB	Yttrium Aluminium Borate
YAG	Yttrium aluminium garnet ($Y_3Al_5O_{15}$)
Yb	Ytterbium
Yb: Ta_2O_5	Ytterbium doped tantalum penxoxide
YCOB	Yttrium Calcium Oxoborate
YLF	Yttrium lithium fluoride
ZBLAN	Fluoride glass made with ZrF_4-BaF_2-LaF_3-AlF_3-NaF
at.%	Atomic percentage

Dedicated to my family

Chapter 1: Introduction

Over the last few decades, the study of laser has attracted a lot of interest because of its ability of generating an intense beam of coherent monochromatic light [1]. Laser devices can be distinguished by their amplifying medium, for instance, gas, solid state, semiconductor, organic dye, etc [2-5]. Among those, solid state lasers play an important role, owing to their small size and low maintenance requirements.

As solid state lasers are made by doping elements that provide light amplification into solid host like glasses or crystals, they can be divided into two parts: transition metal ion doped laser or rare-earth element doped laser by classifying the type of the dopants [6]. In this project, we are focused typically in the rare-earth element doped solid state lasers because of the growing demands for this kind of laser.

Rare-earth elements belong to a series of seventeen elements consisting of fifteen lanthanides, yttrium, and scandium. They are indispensable in various different areas like electrical applications (e.g. permanent magnets in motors and electrode in batteries), chemical applications (e.g. catalysts for vehicle/industrial exhaust or petroleum refining) and optical applications (e.g. imaging phosphors, lasers, fibre communications and specialized glasses) [6].

With different rare-earth dopants, the solid state laser shows different emission characteristics. In recent years, the interest in rare-earth doped lasers has been mostly concentrated on erbium (Er), neodymium (Nd) and ytterbium (Yb) dopants. With the rapid growth of optical communication, Er doped laser attracts a lot of attention owing to its emission band around 1.53 μm which matches the low loss window of optic fibre, located at approximately 1.5 μm [7,8]. Er doped laser emission at 550 nm, produced by upconversion process, is also under investigation for colour display and undersea communication [9-12]. Nd doped lasers can provide tens of kW of output power at wavelengths around 1064 nm and it has been used for cutting and drilling in material processing or medical purposes. Yb doped laser is another candidate for high power application. Multi-kW Yb lasers are now available on the market and higher output power Yb doped lasers are under investigation.

1.1 Motivation

Rare-earth doped solid state lasers can be made into different forms. The most commonly used forms are rod, thin disk, fibre and waveguide [11]. The rod laser usually has a radius of few millimetres and a length from tens to hundreds millimetre. Its large size allows simple and efficient diode pumping but requires a complex cooling system. The thin disk laser is like a slice of a rod, it has a radius of few millimetre and a thickness of only hundreds of micrometre to a few millimetres. Due to the short optical path length, the doping concentration of the thin disk laser is quite high, and consequently causes problems like concentration quenching that limits its performance. Compared with the rod and thin disk lasers, fibre lasers have a much smaller radius that varies from several hundred nanometres to hundreds of micrometres but lengths can reach the kilometre scale. The advantage of this long distance is that the concentration of the dopants can be maintained at a low value so that concentration quenching can be suppressed. Another advantage of the fibre laser is its property of bending, which allows a long fibre laser to be rolled and stored in a small space. The waveguide laser can be made with an equivalent radius (as they are usually made in rectangular shape) of a few micrometres. The main advantage of the waveguide is its small size which leads to on-chip capability and high power density. The small size also results in a large surface-to-volume ratio that offers a high thermal immunity [13].

With the development of integrated optical circuits, there is a growing requirement for the lasers to be scaled down to on-chip size. Due to their small dimensionality and high thermal immunity, waveguide lasers provide a way of scaling down the laser device size. By using waveguide lasers, the erbium doped fibre amplifier (EDFA) can be replaced with a small erbium doped waveguide amplifier (EDWA) as well as having the laser surgery knife made into a portable box and the laser projector scaled to pocket size. Another advantage for using chip size waveguide laser devices is that it is easy to maintain them. As the waveguide laser is a passive laser device, there is a potential of making a system with exchangeable waveguide laser chips. Once the waveguide is broken or reaches its lifetime, it can be replaced easily.

Although the waveguide laser is a very promising form of laser, it still has the disadvantage of requiring a complex fabrication process. To fabricate a waveguide, one has to first deposit the waveguide material layer, followed by the deposition of bottom cladding. Then a mask pattern has to be deposited on top of the waveguide layer and then the pattern needs to be etched in the waveguide material layer. At last, the mask needs to be removed and a top cladding layer can be added if necessary. During this fabrication process, patterning is the most challenging and costly step as it can often result in defects.

However, thanks to the invention of the optical polymer [14-15], the complex optical patterning process can be replaced by nano-imprinting technology. The imprinting technology uses a stamp to imprint the inverse shape of the waveguide on the polymer. The waveguide material will then be deposited into the trench that has been imprinted. Hence, the whole lithography process and waveguide etching are avoided. As a result, mass production is possible. What's more, as long as the stamp used for imprinting is designed carefully, the fabrication quality of the waveguide will be maintained.

The ytterbium ion has been the basis of a number of solid-state lasers, but its usefulness has been limited because the trivalent ytterbium ion has only one excited 4f manifold located at approximately 10,000 cm^{-1}, the next higher level being in the 5d configuration, which begins near 100,000 cm^{-1}. The lack of higher lying states means that the broadband pump source like flash lamps will not be able to pump it efficiently. This problem has been solved with the breakthrough of the mass production of indium gallium arsenide (InGaAs) laser diodes that provide lasing around the 980 nm wavelength, which brings the attention back to Yb laser. The lack of higher lying levels now turns into advantages because it eliminates the problem of excited state absorption (ESA) and upconversion and reduces the concentration quenching which the other rare-earth ions have. Besides, Yb has low quantum defects because of its closely laid Stark levels, resulting in low thermal dispense when lasing. With the even increasing demands of high power laser in both academic and industrial area, Yb has become a favourable candidate for achieving a high power laser device owing to its properties. In this project, we will investigate the ability of ytterbium doped tantalum pentoxide ($Yb:Ta_2O_5$) for achieving a mass producible, high power, compact, on-chip waveguide laser.

1.2 Project Objectives

The aim of this work is to achieve a nanoscale ytterbium doped tantalum pentoxide ($Yb:Ta_2O_5$) waveguide laser device. The objectives of this work can be summarized to:

- Design and simulation of different types of $Yb:Ta_2O_5$ waveguide device
- Investigation of the $Yb:Ta_2O_5$ thin film properties
- Demonstration of new fabrication processes that allows to flexible doping concentration control
- Demonstration of $Yb:Ta_2O_5$ nanowire waveguide lasers

1.3 Thesis Structure

This thesis starts with a review of the background theory as well as different forms of lasers. Chapter 2 introduces the working mechanisms of the solid-state laser and reviews the recent development for ytterbium doped laser devices.

Chapter 3 presents the design considerations of the waveguide including the loss mechanisms and the factor that affects them. The low loss waveguide configuration designed based on the considerations is therefore introduced. Three different types of waveguide are proposed together with their simulation results showing effective confinement of the Yb emission.

Chapter 4 describes the fabrication procedures of strip loaded and buried channel waveguide on Si using conventional CMOS technologies and buried channel waveguide on polymer using nano imprint technique. The first anisotropic $Yb:Ta_2O_5$ reactive ion etching recipe is developed to contribute to Si based buried channel waveguide fabrication.

Chapter 5 presents the experimental procedures used to characterize the properties of $Yb:Ta_2O_5$ thin film. Characterization results of refractive index, Yb concentration, photoluminescence strength and propagation loss of planar Ta_2O_5 and $Yb:Ta_2O_5$ layer are shown.

Chapter 6 describes the experimental procedures of measuring the performance of strip loaded nanowire waveguides. The results of loss measurements and excited lifetime measurement are shown in the chapter. Lasing action has been demonstrated with the threshold and slope efficiency measured.

Chapter 7 concludes this thesis with a brief outlook of what has been done in the project so far. It also provides a plan for the future work on measurements for the buried channel waveguide and the polymer based waveguide as well as improvement of the laser performance of strip loaded waveguide by etching gratings into the waveguide or attaching dielectric mirrors onto the end-facets.

Bibliography

[1] W. T. Silfvast, Laser fundamentals 2nd edition, Cambridge University Press (2008)

[2] M. Endo *et al.*, *Gas Lasers*, CRC Press (2006)

[3] B. Mroziewicz *et al.*, Physics of Semiconductor Lasers 1st Edition, North Holland (1991)

[4] M. I. Nathan, "Semiconductor Lasers", *Appl. Optics*, Vol **5**, No. 10, 1514 (1966)

[5] C. V. Shank, "Physics of dye lasers", *Rev. Mod. Phys.* **47**, 649 (1975)

[6] B. Denker, Handbook of Solid-State Lasers, Woodhead Publishing (2013)

[7] R. J. Mears *et al.*, "Low-noise erbium-doped fibre amplifier operating at 1.54µm", *Electronics Letters*, vol. **23**, no. 19, pp. 1026-1028 (1987)

[8] E. Desurvire *et al.*, "High-gain erbium-doped traveling-wave fiber amplifier", *Opt. Lett.* **12**, 888-890 (1987)

[9] R. Brede *et al.*, "Room-temperature green laser emission of Er:$LiYF_4$", *Appl. Phys. Lett.* **63**, 729 (1993)

[10] S. Heer *et al.*, "Blue, Green, and Red Upconversion Emission from Lanthanide-Doped $LuPO_4$ and $YbPO_4$ Nanocrystals in a Transparent Colloidal Solution", *Angewandte Chemie International Edition*, **42**: 3179–3182 (2003)

[11] W. P. Risk *et al.*, *Compact Blue-Green Lasers*, Cambridge University Press (2003)

[12] E. Downing *et al.*, "A three-color, solid-state, three-dimensional display", *Science*, **273.5279**, 1185, (1996)

[13] J. J. Degnan, "The waveguide laser: A review", *Appl. Phys.,* Vol. **11**, Issue 1, 1-33 (1976)

[14] L. Guo, "Recent progress in nanoimprint technology and its applications", *J. Phys. D: Appl. Phys.* **37** R123 (2004)

[15] Y. Wang *et al.,* "Nanoimprinted polymer lasers with threshold below 100 W/cm^2 using mixed-order distributed feedback resonators", *Opt. Express* **21**, 14362-14367 (2013)

Chapter 2: Background

2.1 Introduction of Lasers

LASER is the acronym for Light Amplification by Stimulated Emission of Radiation. It is a kind of device that emits light that is coherent through optical amplification process based on stimulated emission. It is one of the most important inventions as well as one of the most widely used technologies available.

The first working laser was a ruby laser which was developed in May 1960 by T. H. Maiman [1]. However, the ideas could be traced back to the theory of stimulated emission which Albert Einstein proposed in 1917 [2]. After the invention of the first laser, more and more kinds of lasers were built in the early 1960s. In December of the year 1960, A. Javan, W. Bennett and D. Herriot successfully made a Helium-Neon Laser, which was the first gas laser and the first continuous-wave (CW) laser [3]. In year 1962, Robert Hall created a revolutionary type of laser which is extensively used even nowadays – the Semiconductor Injection Laser [4]. In 1964, the first fibre laser and fibre laser amplifier was demonstrated by Elias Snitzer [5]. Later in the same year, the carbon dioxide laser, argon ion laser, and neodymium doped yttrium aluminium garnet (Nd:YAG) lasers were invented [6]. The first widely recognized commercial application of lasers was the bar code scanner in 1974.

With the development of material science, more and more different materials were found suitable for making different kinds of laser. As a result, lasers now have found use in many areas, such as industrial (marking, welding, cutting and drilling), medical (surgery and sensing), IT (communication) and military (target designation, ranging, defensive countermeasures).

2.2 Basic Concepts of Laser

Although there are many different types of lasers, they share the same working principle.

2.2.1 Absorption

If an electromagnetic (EM) wave with a frequency of ν passes through a medium (i.e. a group of atoms, molecules, etc.), there is a possibility of the EM wave being absorbed by an atom or molecule in ground state. The atom or molecule will then be excited to a state which has higher energy. The process is shown in *Figure 2.1*. In this process, the energy of the EM wave must be as the same as the energy difference between the ground state and the exited state. Otherwise, the EM wave will pass the medium without being absorbed. The following equation shows the relationship between the incident EM wave and the energies of different states.

$$h\nu = \Delta E = E_2 - E_1 \qquad Eq.2-1$$

where h and is the planck constant, ν is the frequency of the EM wave, E_1 and E_2 are the energy of the ground state and excited state, respectively.

This process can be described using Einstein's coefficient B_{12} (m^3/Js^2), which expresses the probability of the absorption process per unit time per unit spectral energy density [7]. The subscript "12" means it is the transition from state 1 with energy of E_1 to state 2 with energy E_2. Thus, the change of the atom density in state 1 ground state can be expressed as:

$$\left(\frac{dN_1}{dt}\right)_{absorption} = -B_{12}N_1\rho(\nu) \qquad Eq.2-2$$

At the same time as the depopulating state 1, the population in state 2 increases:

$$\left(\frac{dN_2}{dt}\right)_{absorption} = B_{12}N_1\rho(\nu) \qquad Eq.2-3$$

where N_1 and N_2 are the population densities of atoms in the ground state and excited state respectively, ν is the frequency of the incident EM wave, and $\rho(\nu)$ is the spectral energy density. As shown in the Eq. 2-2, the rate of absorption process is proportional to the spectral energy density of the EM wave and the population density in the ground state (N_1) [8].

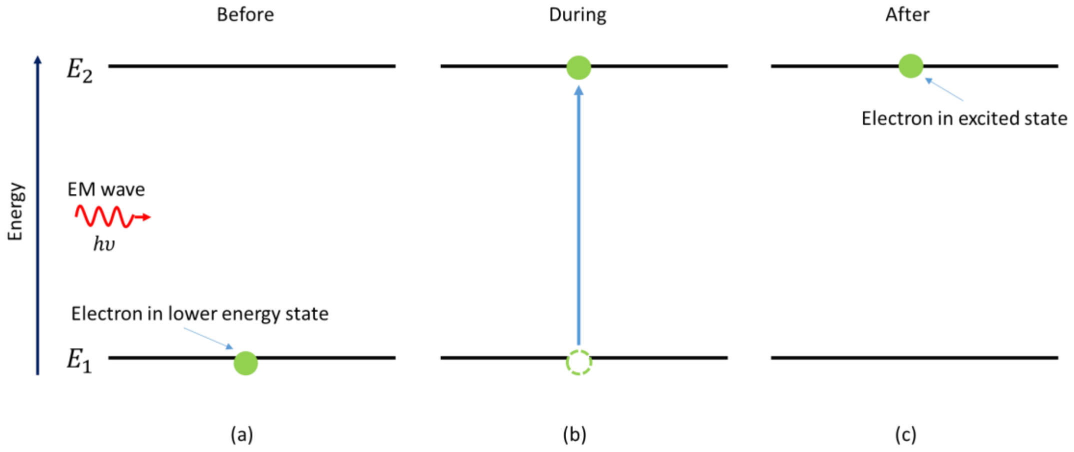

Figure 2.1 The process of absorption: (a) before the process starts; (b) during the process and (c) after the process finished

2.2.2 Spontaneous Emission

As mentioned in Section 2.1, the basis of a laser is stimulated emission. However, every lasing phenomenon starts from spontaneous emission.

The spontaneous emission is a process when a quantum system (e.g. atom, molecule, etc.) in an excited state decays to a lower energy state spontaneously and emits energy [8]. If the excited state has an energy level of E_2, the lower energy state has an energy level of E_1, after the decay, the emission energy is:

$$\Delta E = E_2 - E_1 \qquad Eq. 2-4$$

If the quantum system is a light source, then the emission would be a photon. Hence, Eq.2-4 becomes:

$$\Delta E = E_2 - E_1 = h\nu \qquad Eq. 2-5$$

Where h is the Planck constant and ν is the frequency of the emitted photon. Both the phase and the direction of the emitted photon are random. *Figure 2.2* illustrates the process of spontaneous emission.

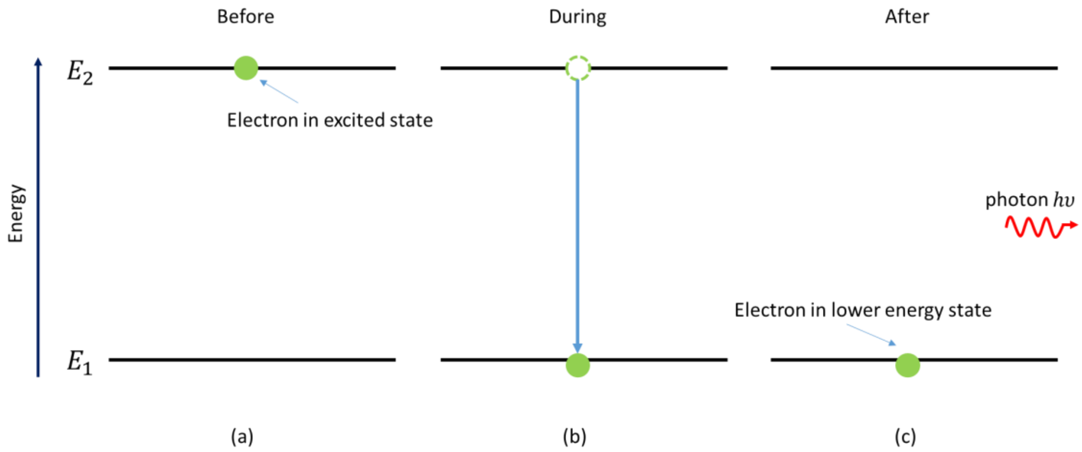

Figure 2.2 The process of spontaneous emission: (a) before the process starts; (b) during the process and (c) after the process finished

In this process, the Einstein coefficient $A_{21}(s^{-1})$ is introduced. Similarly as for the subscript of the Einstein coefficient B, the “21” means the transition is from state 2 to state 1. The coefficient A_{21} gives the probability per unit time that the spontaneous emission happens. The changes of population of atoms in different state are:

$$\left(\frac{dN_2}{dt}\right)_{spontaneous} = -A_{21}N_2 \qquad Eq.2-6$$

$$\left(\frac{dN_1}{dt}\right)_{spontaneous} = A_{21}N_2 \qquad Eq.2-7$$

where N_1 and N_2 are the population densities of atoms in the ground state and excited state respectively. Same as the absorption process, the rate of this process is proportional to the number of atoms or molecules in the excited state (N_2).

2.2.3 Stimulated Emission

The process of stimulated emission can be explained as an atom in excited state interacting with an electromagnetic (EM) wave (e.g. a photon) of a certain frequency, the atom may decay to a lower energy level similarly to spontaneous emission, releasing the energy which is the difference between the excited state and the lower energy level [8].

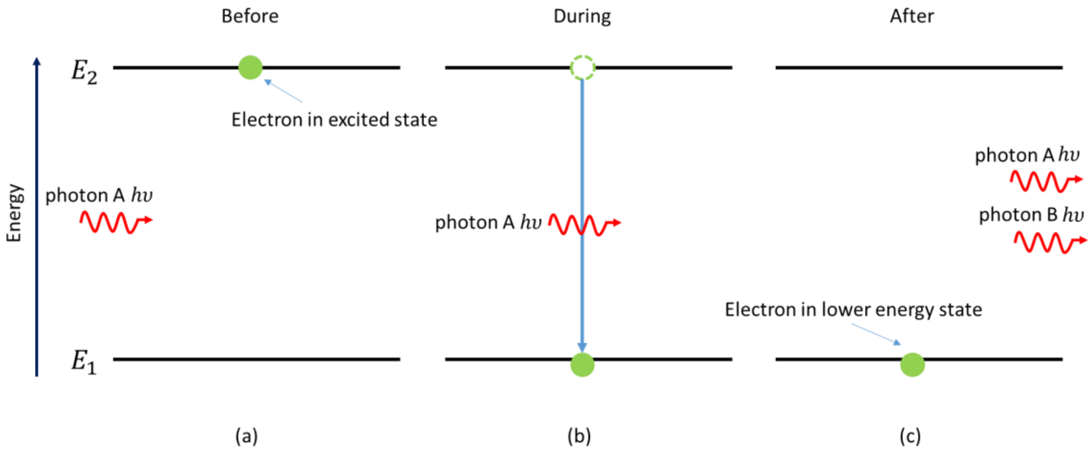

Figure 2.3 The process of stimulated emission. (a) Before the process starts; (b) During the process; (c) After the process finished.

Figure 2.3 shows the process of stimulated emission in an optical medium – an atom in excited state interacts with a photon of energy $h\upsilon$ (photon A), the atom then being stimulated to emit a second photon (photon B) with the same frequency, direction and phase as the incident photon whilst the atom drops to the lower energy level. These two photons could trigger another 2 stimulated emissions, producing four photons with the same frequency, direction and phase. The subsequent photons will then create an avalanche effect (i.e. the number of photons doubles after every successful stimulated emission) and a huge number of homogenous photons will be built up in the medium, therefore coherent light is generated.

This process can be characterized using the Einstein coefficient B_{21} (m^3/Js^2). The changes in atom densities of different states can be expressed as [7]:

$$\left(\frac{dN_2}{dt}\right)_{stimulated} = -B_{21}N_2\rho(\nu) \qquad Eq. 2-8$$

$$\left(\frac{dN_1}{dt}\right)_{stimulated} = B_{21}N_2\rho(\nu) \qquad Eq. 2-9$$

where N_1 and N_2 are the population densities of atoms in the ground state and excited state respectively, ν is the frequency of the incident EM wave, and $\rho(\nu)$ is the spectral energy density. Therefore, the rate of stimulated emission occurring is proportional to the population density of atoms at excited state (N_2) and the spectral energy density of the incident EM wave that triggers the process.

2.2.4 Transition Cross Sections

The transition cross sections are used to quantify the likelihood of optically induced transitions (absorption and emission). The absorption cross section (σ_a) quantifies the ability of a laser ion to absorb light and the emission cross section (σ_e) quantifies the ability of a laser ion to emit light. Both these two cross sections have a unit of cm^2 and are wavelength dependent [9].

According to the Beer-Lambert Law, the relationship between the intensity of the light before and after travelling through a material can be written as:

$$I(\lambda) = I_0(\lambda)\, exp[-\alpha_m(\lambda) \times L] \qquad Eq. 2-10$$

where $I(\lambda)$ and $I_0(\lambda)$ are the intensity of the transmitted light at the end of the medium and incident light at the beginning of the medium at wavelength λ, $\alpha_m(\lambda)$ is the material absorption coefficient (in cm^{-1}) related to optical transitions between energy levels at wavelength λ, L is the length of the sample, respectively. Since the relationship of absorption cross section and the material absorption coefficient can be expressed as:

$$\sigma_a = \alpha_m(\lambda) \,/\, N \qquad Eq. 2-11$$

where N is the atomic number density of the material. In this case, N is the same as the laser ion doping concentration ρ. Therefore, the absorption cross section can be expressed as:

$$\sigma_a(\lambda) = \frac{\alpha_m(\lambda)}{\rho} = \frac{ln\left(\frac{I_0(\lambda)}{I(\lambda)}\right)}{\rho \times L} \qquad Eq. 2-12$$

The emission cross section $\sigma_e(\lambda)$ can be calculated by the McCumber relation:

$$\sigma_e(\lambda) = \sigma_a(\lambda) \;/\; \exp\left(\frac{h\upsilon - E_0}{k_B T}\right) \qquad Eq.2-13$$

where h is the Planck's constant; υ is the frequency of the measured light (λ); E_0 is the “zero line” energy, which is the energy difference between the lowest energy levels of the two manifolds that are involved in the absorption and emission; k_B is the Boltzman constant and T is the temperature.

As the transition cross section quantifies the likelihood of the optically induced transition, the rate, R, of the transition is given as the production of the cross section and photon flux:

$$R = \sigma(\lambda) \times \frac{I(\lambda)}{h\nu} \qquad Eq.2-14$$

where $\sigma(\lambda)$ is the transition cross section (either absorption or emission), $I(\lambda)$ is the optical intensity of the light propagates in the medium at wavelength λ, h is the Planck's constant and υ is the frequency of the incoming light (λ).

Once the absorption and emission cross section are known, the gain coefficient of the laser gain material $g(\lambda)$ (in cm^{-1}) at wavelength λ is given as:

$$g(\lambda) = \sigma_e(\lambda)N_2 - \sigma_a(\lambda)N_1 \qquad Eq.2-15$$

where N_2 and N_1 is the population density of upper laser level and lower laser level, respectively.

2.2.5 Lasing Condition

Figure 2.4 shows the basic operation of a laser device. The light oscillates in the gain medium (or the active medium) with the help of two mirrors attached on the end facets of the gain medium. There is also a pumping source that keeps injecting energy into the gain medium to maintain lasing.

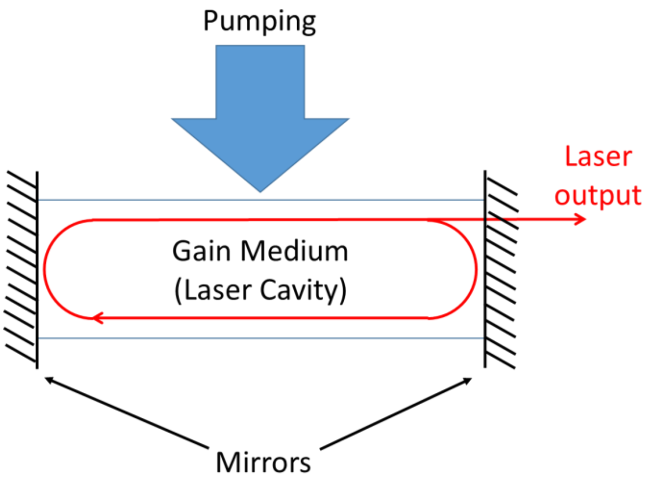

Figure 2.4 Simplified schematic of laser device operation

As introduced in Section 2.2.3, repeating stimulated emission can produce a large number of homogenous photons, which generates a laser emission. However, to establish a laser in real device, there are two conditions that must be satisfied: the net round trip gain equals to one and the total phase shift in a single round trip equals to a multiple of 2π.

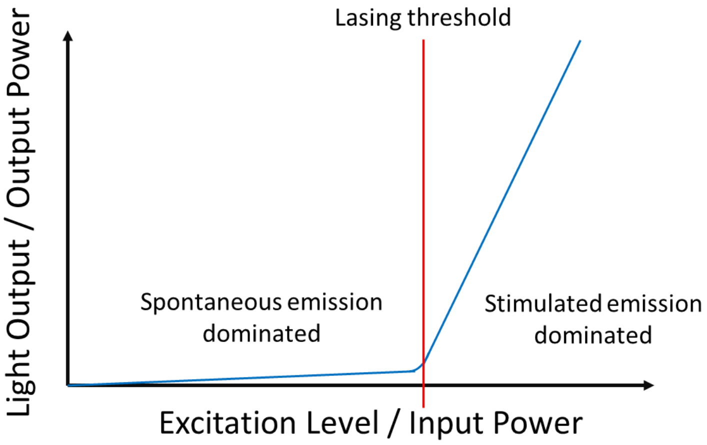

Figure 2.5 Light output with respect of excitation level

The threshold of lasing is the lowest excitation level that allows stimulated emission to dominate the laser output. *Figure 2.5* shows the light output versus excitation level curve of a typical laser device. Below the threshold, the laser device is dominated by spontaneous emission and its output power increases slowly with increasing of excitation level. Once the threshold is reached, stimulated emission dominates the emission of the device, and the light output increases dramatically with increasing input power. Only above the threshold, the laser can be said to be lasing. The slope of the curve after threshold is known as the slope efficiency of a laser and describes the power conversion efficiency of the laser beyond threshold [8].

Figure 2.6 illustrates a simplified schematic of laser operation. Assuming the laser is in steady-state operation, for a gain medium with gain coefficient of g which includes the losses due to optical transitions between energy levels and cavity loss coefficient of α that presents all the losses inside the cavity except the losses caused by optical transitions and transmission losses cause by end facet mirrors, the single trip gain G_{single} of a gain medium with length l is given as [8]:

$$G_{single} = \exp(gl)\exp(-\alpha l) \qquad Eq. 2-16$$

If the light travels a round trip in the cavity, apart from the loss of the gain medium, light experiences losses in intensity when reflected by the two mirrors at the end of the cavity. Thus, the round trip gain is:

$$G_{RTG} = R_1 R_2 \exp(2gl)\exp(-2\alpha l) \qquad Eq. 2-17$$

where R_1 and R_2 are the mirror reflectivity values of the two end facet mirrors, g is the gain of the gain medium, α is the loss of the medium, and l is the length of the medium.

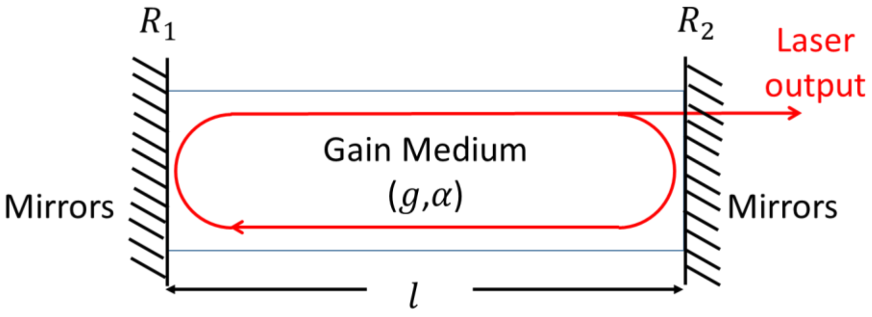

Figure 2.6 Schematic of laser operation

When lasing at threshold, the round trip gain of the laser equals to one, in other words the total gain of the laser medium is exactly balanced by the total loss of the laser. Hence,

$$G_{RTG} = R_1 R_2 \exp(2gl)\exp(-2\alpha l) = 1 \qquad Eq. 2-18$$

This means the light inside the laser cavity has a steady intensity – it neither decays nor grows after each round trip. If the round trip gain is smaller than one, the intensity of the light will keep decreasing inside the medium and will finally disappear. If the round trip gain is greater than unity, the radiation increases exponentially on each successive round trip and will eventually form a coherent oscillation inside the cavity.

The threshold gain $g_{threshold}$ coefficient for achieving lasing can be obtained by rearranging the Eq. 2-18.

$$g_{threshold} = \frac{1}{2l}\ln\left(\frac{1}{R_1R_2}\right) + \alpha \qquad Eq. 2-19$$

Hence, the threshold gain coefficient increases with decreasing mirror reflectivity and increasing of the medium loss.

The second condition of lasing requires that the total phase shift of a single round trip must be a multiple of 2π [8]. According to the wave interference theory, constructive interference occurs only when two waves are in-phase. If the two waves are not in phase, destructive interference happens, reducing the energies of both waves. Therefore, to gain a positive optical feedback, the reflected wave must have the same phase that matches the original input wave, in the other word, the round trip phase shift equals to a multiple of 2π.

2.3 Working Mechanisms of Active Ions in Solid-state Lasers

Solid state lasers use a solid material (i.e. crystal, glass or amorphous materials) as their gain medium. Although semiconductor lasers are also in the solid-state, they are usually considered as a different class from solid-state lasers owing to their electronic pumping methods.

The gain medium of a solid-state laser consists of two parts, the host and the dopant. The host is used for holding the dopant at a certain position in the lattice. The host is usually formed by a glass or crystalline material and it can affect the performances of the laser such as laser threshold and slope efficiency. The dopant, which provides the optical gain, is normally chosen from rare-earth (RE) elements like neodymium (Nd) and erbium (Er) or some transition metals like chromium (Cr) and titanium (Ti) [10].

As the host materials and dopants vary, there are hundreds of different solid-state lasers designs. Among those lasers, the most widely used are the Nd-doped, Yb-doped yttrium aluminium garnet (YAG) or glass laser. These combinations can offer a very high output power which could be used for both industrial and military purposes.

Active ions (or the dopants) in solid state lasers do not only work as individuals but also interact with other ions. Depending on the purpose of the laser, some of the ion interactions are very desirable and others stop the lasing process. For instance, the resonant multi-photon absorption is highly desirable for upconversion laser systems which produces laser output with higher frequency than its input, but acts as a loss scheme if it appears in a standard laser system. Another example is the co-operative upconversion. In a sensitizer-co-doped upconversion laser, it is a mechanism allowing the sensitizer ion that absorbs the pump light which laser active ion can hardly absorb and transferring this energy to the laser active ion. However, in most other laser systems, it has been regarded as a loss mechanism due to the increased probability of non-radiative decay that it introduces [8].

2.3.1 **Single-ion performance**

2.3.1.1 **Standard Laser process**

Downconversion process, also known as the basis of standard optical pumped lasers, is an emission scheme where the wavelength of photon emission is longer than that of the pump light. The scheme of the process is shown in *Figure 2.7*.

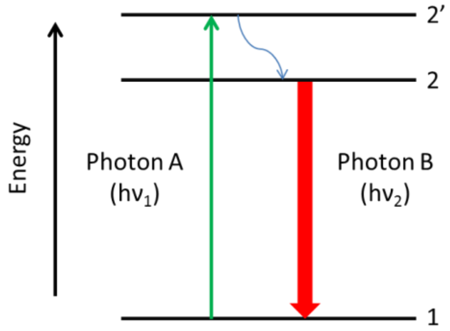

Figure 2.7 Schematic of downconversion process

To make this process easy to understand, the system demonstrated here is a simplified three-level system while the real system may be more complicated. The process is quite straight forward: the active ion has been promoted to a higher energy level (level 2') by absorbing a pump photon A, then non-radiatively drops to level 2 by releasing heat, and emits photon B through radiative decay [8].

2.3.1.2 **Resonant Multi-photon Absorption**

Resonant multi-photon absorption is the main mechanism of upconversion. Opposite to downconversion process, upconversion is a type of non-linear process which can up convert the frequency of the pump light. By applying different mechanisms of upconversion, the photon energy of the output can be larger than that of the pump source [11].

Resonant multi-photon absorption is the most intuitive upconversion process which uses sequential absorption of more than one photon through different intermediate states of the ion. The schematic of this mechanism can be explained through the figure below.

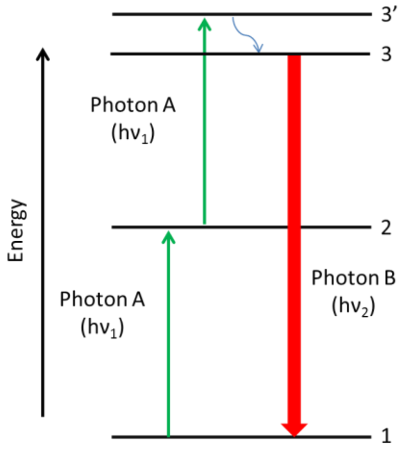

Figure 2.8 Schematic of resonant multi-photon absorption process

Figure 2.8 shows the fundamental resonant multi-photon absorption process – two-photon sequential absorption. As shown, the upper state is populated by the sequential absorption of two photons. In the first step of this upconversion process, the ion absorbs the pump photon A and gets excited from ground level 1 to the metastable level 2. In the second step of this process, the ion will further absorb a pump photon and will be excited to the upper laser level. The second step is also known as excited state absorption (ESA). Due to the presence of the multi-phonon non-radiative decay, the ion in level 3’ will relax to the level 3 rapidly and eventually radiatively decays to the ground state.

This non-linear process is desired when building an upconversion laser. However, for a standard laser (i.e. a laser that has a desired lasing level at level 2), multi-photon absorption will depopulate the desired lasing level and cause unwanted luminescence.

2.3.2 **Multi-ions interactions**

A characteristic of solid state active ions is that they have a tendency of having ion-ion interactions. These interactions can happen either between the ions of the same rare-earth element or between the ions of different rare-earth elements. The former lead to losses in the material as it increases the non-radiative decay or luminescence from unwanted transitions. However, the latter can constitute an efficient pumping scheme. The excitation is provided by one rare-earth ion and then transferred to another ion of a different rare-earth element. By employing this scheme, a wider selection of pumping sources is allowed. The following sections introduce the three most important ion interactions [12].

2.3.2.1 **Co-operative Upconversion**

The co-operative upconversion happens between 2 ions in the metastable state. As expressed in *Figure 2.9*, Ion A, which is at metastable level, decays to the ground state and promotes Ion B which is as well in the metastable state to a higher level. Once Ion B has been promoted into the higher state, it may decay radiatively to ground state, or more likely return to the ground state rapidly and non-radiatively. There is also a possibility that a radiative emission will occur when the ion returns to metastable level [11].

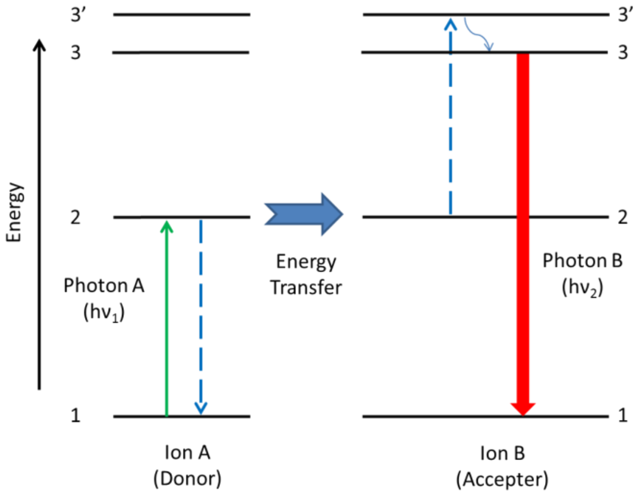

Figure 2.9 Schematic of cooperative upconversion process

Since this interaction occurs between 2 ions at the metastable level, it reduces the lifetime of the metastable states. In addition, when this interaction happens in the oxide glass hosts, the relaxation of the Ion B is non-radiative. Therefore, the co-operative upconversion actually forms a loss mechanism when in the case of happening between ions of the same type [11, 12].

2.3.2.2 **Energy Migration**

Different to the co-operative upconversion, energy migration happens between a metastable state ion and a ground state ion. *Figure 2.10* displays the energy migration happening between two ions. The process can be described as follows: an ion in the metastable state (Ion A) decays to the ground state and excites another ion (Ion B) to the metastable level. After being excited to the metastable level, Ion B will drop to the ground level most probably through fast non-radiative decay.

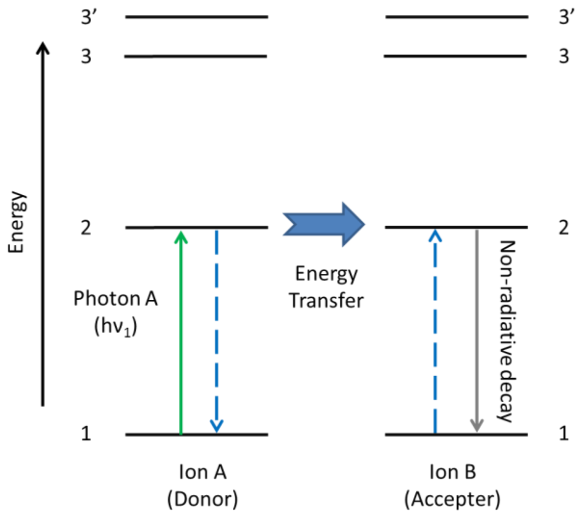

Figure 2.10 Schematic of energy migration process

As a result of this, every successive energy transfer will increase the probability of the non-radiative decay of metastable states, which increases the loss of the system. This process is also unwanted in downconversion laser systems as it increases the threshold of lasing [11].

2.3.2.3 **Cross-relaxation**

Cross relaxation is an interaction between ions in the highly excited state and ions in the ground state. As illustrated in *Figure 2.11*, ion A, laying on the higher excited state, drops to the metastable state non-radiatively and transfers the energy to a nearby ground state ion B, promoting it from ground state to the metastable state [11].

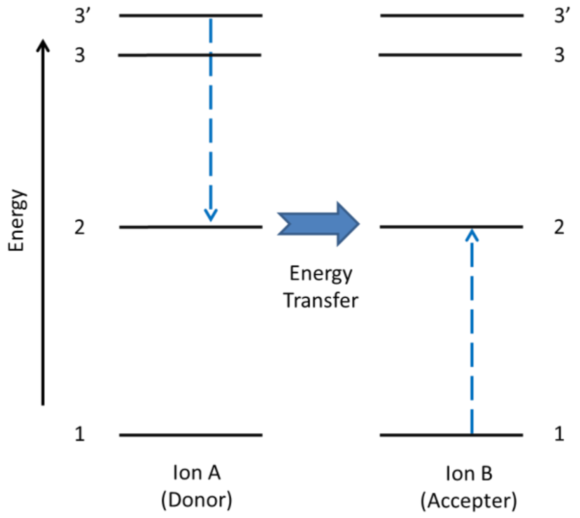

Figure 2.11 Schematic of cross-relaxation process

For an upconversion laser, this process is a loss mechanism as the cross-relaxation depopulates the higher excited level (level 3’) through non-radiative decay. The cross-relaxation occurs more frequently when the concentration of the active ion reaches a high level. Frequent occurrence of cross-relaxation quenches the light that is emitted from the active ion and hence make lasing impossible.

2.3.2.4 Co-operative Emission

The co-operative emission, also known as co-operative luminescence, is a process by which a pair of ions emits one photon by simultaneous depopulation from their excited states. *Figure 2.12* shows the schematic of a co-operative emission process. Both ion A and ion B are in excited states, instead of decaying to ground state individually, there is a probability that they will decay simultaneously as a pair, emitting a photon that has the energy equals to the sum of the energy difference between the excited state and ground state for both ions. [13]

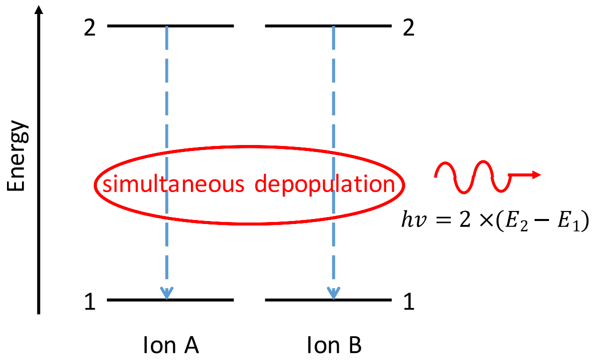

Figure 2.12 Schematic of co-operative emission process

Similar to the other multi-ion interactions, co-operative emission acts as a loss mechanism when employing standard laser as it depopulates the upper energy level. On the other hand, for upconversion laser, it offers another route of producing higher energy photon with lower energy photon pumping.

2.4 Dopants of Gain Medium in Solid-state Lasers

As introduced in Section 2.3, the gain medium, or so called laser active medium of a solid-state laser is formed by a host and a dopant. In these two parts, the dopant can provide optical gain and thus build up a laser. The dopant can be chosen from either transition metal elements or rare-earth (RE) elements.

2.4.1 Transition Metal Ions

The most commonly used transition metals are chromium (Cr) and titanium (Ti). All transition metals have optical transitions involving electrons in the 3d shell. With different valence situation (i.e. Cr^{2+} or Cr^{3+}), the transition metals can have different emission wavelengths. Divalent iron (Fe^{2+}) and cobalt (Co^{2+}) have also been used as the active ions in transition metal gain media but not as commonly as Ti and Cr. From the table above, one can find that transition metal ions have the common property, they all have a broad emission bandwidth. This makes them desirable for tuneable lasers [14-16].

Table 2.1 Typical emission wavelength range of transition metals [10]

Ion	*Typical Emission Wavelengths*
Cr^{2+}	1.9 – 3.4 µm
Cr^{3+}	0.7 – 0.9 µm
Cr^{4+}	1.1 – 1.65 µm
Ti^{3+}	0.65 – 1.1 µm
Fe^{2+}	3.7 – 5.1 µm

2.4.2 Rare-earth Ions

In the last few decades, rare-earth (RE) elements have received an increasing interest as they are natural candidates for active ions in solid state laser. Due to the natural properties of the $4f$ electron shell of the RE elements, their trivalent ions all exhibit intense narrow-band luminescence in a large range of different hosts. With proper pumping, these elements can emit light covering the ultraviolet to near infrared range, allowing them to be applied in both scientific and commercial fields [12].

Currently, the RE elements that have been most frequently used as dopants are neodymium (Nd), ytterbium (Yb), erbium (Er), thulium (Tm), holmium (Ho), prasesodymium (Pr) and cerium (Ce) [17]. Compared with transition metals, rare earth ions have narrower emission bandwidths, which makes them ideal for interferometric sensing, optical frequency metrology and etc.

Table 2.2 Typical emission wavelength range of rare-earth ions [18]

Ion	*Typical Emission Wavelengths*
Nd^{3+}	0.9 – 0.95 µm, 1.03 – 1.1 µm, 1.32 – 1.35 µm
Yb^{3+}	1.0 – 1.1 µm
Er^{3+}	0.55 µm, 1.5 – 1.6 µm, 2.7 µm
Tm^{3+}	0.48 µm , 0.8 µm , 1.45 – 1.53 µm, 1.7 – 2.1µm
Ho^{3+}	2.1 µm, 2.8 – 2.9 µm
Pr^{3+}	0.49 µm, 0.52 µm, 0.6 µm, 0.635 µm, 1.3 µm
Ce^{3+}	0.28 – 0.33 µm

2.5 Amorphous Hosts of Gain Medium in Solid-state Lasers

Due to the solid-state lasers being mostly optical pumped, the host material should be as much optically transparent as possible at the pumping wavelength. Otherwise, the pumping will be absorbed by the host rather than the dopants which provide the optical gain. Therefore, choosing the host material is very important for building up a solid-state laser.

The host can be chosen to be crystalline or amorphous. In selecting a suitable material for a laser active ion host, several key criteria must be considered:

a). The material must have good optical properties. It needs to be highly transparent, which means low absorption and scattering in the both pump and laser emitting wavelength range. The material must not have variations in the refraction index as that will lead to poor beam quality.

b). The phonon energy of the material must be low. Phonons with large energy will strongly increase the non-radiative transitions of ions, such as multi-phonon transitions. In most of cases, these non-radiative transitions lead to the quenching of the upper-state population, therefore lowering the quantum efficiency of the laser, and at worst case, even make lasing impossible.

c). The material also needs to have a good mechanical and thermal performance. The material needs to have a good thermal conductivity to permit high power operation as both pump and the laser itself will produce a lot of heat. It must have high enough fracture strength and hardness to overcome the strain and stress caused by the heat.

d). The refractive index of the material must be high enough to create a high contrast between the lasing part and the protective cladding. If the refractive index is comparable to the cladding, the pumping power will be spread all over the device rather than only inside the lasing cavity.

2.5.1 **Glasses**

Glass is an important class of host materials for some rare earth elements. The outstanding advantage of glass compared to other host materials is the tremendous size capability (from millimetres to hundreds of centimetres) for high energy applications [19-20]. However, the drawbacks of the glass host material are also quite obvious. The lattice sites which can accept the laser active ions are not uniformly distributed in the glass, resulting in a broad fluorescent line width and relatively high laser threshold (i.e. more pump power is needed to generate a laser). Rather than the drawback of lattice sites, the main defect of the glass host materials is the low thermal conductivity which leads to stress inside the glass. The stress results in a strain birefringence which makes the refractive index polarization dependent (i.e. the glass host is now anisotropic media). Therefore, an optical distortion is induced. Common glasses that used as solid state laser hosts are silicate glasses, phosphate glasses and fluoride glasses. Silicate glasses are glasses that based on SiO_2. As the name stated, phosphate glasses are based on P_2O_5. Compared to the silicate glasses, phosphate glasses have better optical properties such as extended transparent range and better ability of accepting rare-earth ions. However, its poor chemical durability (compared to silicate glasses) added some limitation when competing with silicate glasses. The most known fluoride glass is ZBLAN (ZrF_4-BaF_2-LaF_3-AlF_3-NaF) which possesses properties like large transparent range (0.3 – 7 μm), low dispersion and low phonon energy of 600 cm^{-1} (where silicate glass is 1100 cm^{-1} and phosphate glass is 1300 cm^{-1}). [25-28]

2.5.2 **Oxides**

Oxides are a large group of solid state hosts. The typical hosts are aluminium oxide (Al_2O_3 or sapphire), yttrium oxide (Y_2O_3), zirconium oxide (ZrO_2), titanium oxide (TiO_2) and tantalum pentoxide (Ta_2O_5).

All these 5 host material have similar properties, such as very good thermal conductivity, good hardness and wide transmittance bandwidth which make them a good host. However, there are still some differences between them allowing them to be used for different applications.

Al_2O_3 host is usually doped with Ti, forming a large wavelength range tuneable Ti: Sapphire laser. It also can be doped with rare earth elements [21-23]. Compared with the Al_2O_3, Y_2O_3 has a higher refractive index (~1.7 - 1.9 compared with ~1.6 - 1.7 for Al_2O_3). Its low phonon energy and similar structure with Er_2O_3 make doping of rare earth ions (especially Er^{3+}) very easy[24]. The high refractive indices of both TiO_2 and Ta_2O_5 across the visible wavelength range make them into the most desired host for visible lasers like the infrared-to-visible upconversion laser [29-32].

2.6 Material Selection

2.6.1 **Choice of Dopant**

As mentioned in Section 2.4, compared to transition metal ions, rare-earth ions have narrower emission line width. Therefore, only two rare-earth ions Yb and Nd, which can provide emission around the wavelength of 1 μm, have been considered.

Compare to its already established competitor Nd, Yb possesses a number of advantages owing to its 2-level simple energy band structure. Due to the lack of higher lying level in Yb, excited state absorption in Yb has been eliminated where Nd still suffers. The 2-level energy band structure also leads to a low quantum defect (i.e. the difference between energy of pumping photon and energy of signal photon), allowing a higher optical to optical efficiency and the capability of forming a high power laser. Therefore, in this work, Yb has been picked as the dopant for the solid state laser device. [33-34]

2.6.2 **Choice of Host**

Ta_2O_5 has been chosen as the host material. There are several reasons for picking this material.

First of all, the Ta_2O_5 has a large band gap varying from 3.8 eV to 5.3 eV. The band gap depends on the method of manufacturing and the more amorphous the Ta_2O_5 is, the greater the band gap is[35-39]. This large band gap makes Ta_2O_5 a transparent material for most of the optical wavelengths (i.e. the photon will be absorbed only when its energy is larger than the Ta_2O_5 band gap, for 3.8 eV, the equivalent photon wavelength is 326 nm).

Secondly, compared to the other amorphous oxide hosts, Ta_2O_5 has the lowest maximum phonon energy (~450 cm^{-1}) [40], where TiO_2, ZrO_2, Al_2O_3 and Y_2O_3 has phonon energy of 876 cm^{-1}, 748 cm^{-1}, 870 cm^{-1} and 600 cm^{-1}, respectively[41-44], This property helps to avoid the non-radiative transitions caused by phonon bridging, where the phonons act as a bridge to help the excited state relaxes non-radiatively. Thirdly, the Ta_2O_5 has a crystallization temperature of 650 °C, which is high enough for undertaking high power operations.

2.7 Yb Doped Solid-state Lasers

The first lasing action of Yb^{3+} ions has been found in a silicate glass in 1962 [45]. Compared with the other rare-earth ions, the Yb^{3+} ion has a simple energy diagram consisting of only two energy manifolds $^2F_{5/2}$ and $^2F_{7/2}$ that contains several different sub energy levels. The energy band diagram of Yb^{3+} ion is shown in *Figure 2.13*.

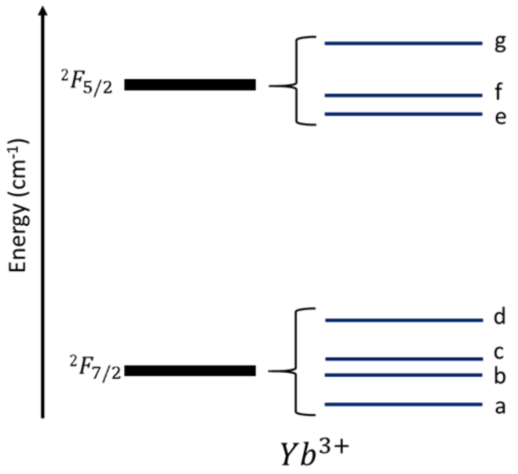

Figure 2.13 Energy band diagram and emission wavelengths of Yb^{3+}, a-d sub band forms $^2F_{7/2}$ manifold and e-g sub band forms $^2F_{5/2}$ manifold

After the demonstration of the first Yb^{3+} laser, the Yb^{3+} ion attracted a lot of attention. However, it is not because of its property to lase but due to its ability of acting as a sensitizing ion. The Yb^{3+} absorbs pumping photons over a wide spectrum and transfers the absorbed energy to the laser active ions that have been co-doped with other rare-earth ions like Er^{3+}, Ho^{3+} or Tm^{3+} [46-48].

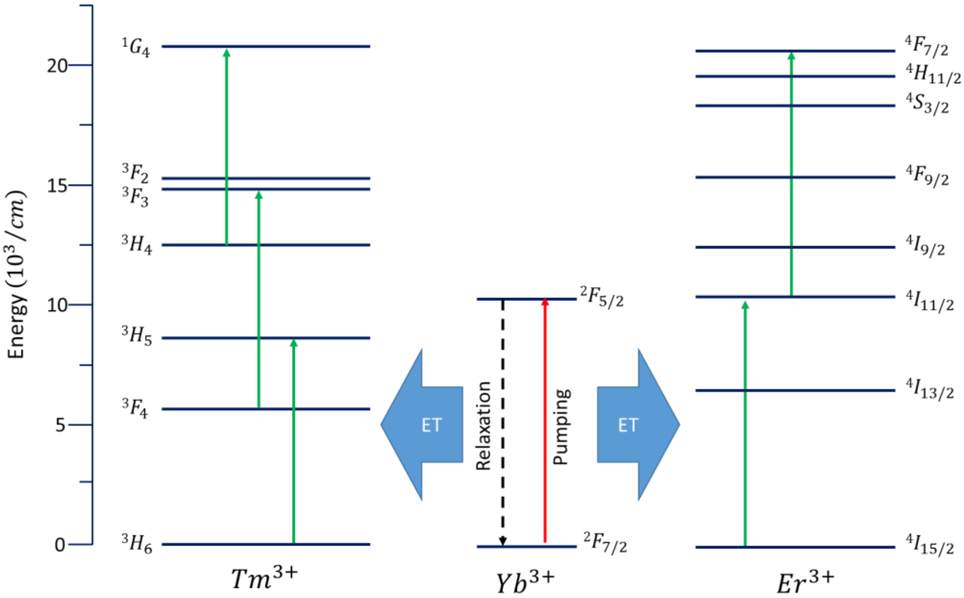

Figure 2.14 Energy transfer diagram of Yb^{3+} (donor), Tm^{3+} (acceptor) and Er^{3+} (acceptor)

Figure 2.14 illustrates the process of the energy transfer between Yb^{3+} ion and Tm^{3+}/Er^{3+} ions. The green lines shown in Tm^{3+} and Er^{3+} energy levels are the possible transitions of each ion when accepting energy transferred from the Yb^{3+} ions.

The reason that most of the attentions of Yb^{3+} ion were on its sensitization ability rather than its lasing is that it has been overshadowed by the Nd^{3+} ion. The Yb^{3+} ion has a similar emission wavelength domain compared with the Nd^{3+} ion – Yb^{3+} is centred at 1030 nm and Nd^{3+} is centred at 1060 nm. However, unlike the four-level system of Nd^{3+} ion, the Yb^{3+} ion has a quasi-three level system.

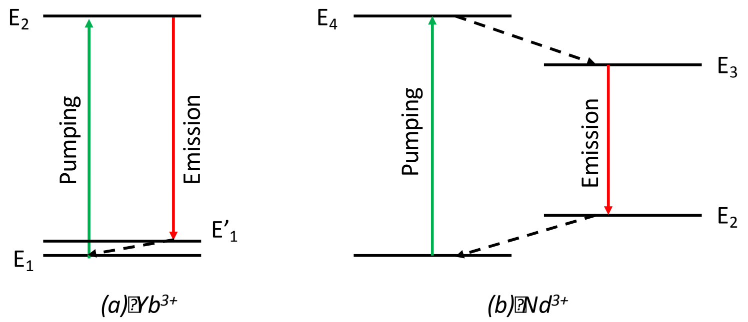

Figure 2.15 (a) Quasi-three level system of Yb^{3+} *and (b) Four level system of* Nd^{3+}

The schematic of quasi-three level system is shown in *Figure 2.15 (a)*. Different from the four-level system shown in *Figure 2.15 (b)*, the lower laser level of quasi-three-level system is very close to the ground state. As a consequence, the quantum defect is much lower in the Yb^{3+} system, meaning the energy difference between the pumping photon and emission photon is smaller in Yb^{3+} system, yielding a higher optical to optical efficiency. However, due to the lower laser level is very close to the ground level, an appreciable population will be built up in Yb^{3+} system, which causes reabsorption at the laser wavelength and hence increases the threshold.

Moreover, the Yb^{3+} ion has only one excited $4f^{13}$ shell state $^2F_{5/2}$ which is centred at the 950nm wavelength domain. This fact limits the use of a wide spectrum pumping source, which made the efficient pumping of Yb^{3+} doped laser system hard to achieve before 1990s.

The turning point came in year 1992. With the popularization of the high power Indium gallium arsenide (InGaAs) laser diode which has laser wavelengths covering from 0.9 µm to 1.1 µm, an efficient pumping in terms of higher pump absorption can be achieved [49]. With efficient pumping, the drawback of only one existing manifold in Yb^{3+} turns into an advantage. Owing to the existence of only one excited manifold, neither excited state absorption (ESA) nor cross-relaxation occurs at high dopant concentrations and high pump powers [50-53]. This property makes the Yb^{3+} doped laser a candidate of non-Nd high power lasers.

As mentioned in Section 2.3, the performance of the solid state laser systems also counts on the host material. With different host materials, some optical characteristics like absorption and emission peaks of the laser active ions and fluorescence lifetime will change.

Table 2.3 Yb^{3+} ion performance in different host materials.

Host	**Conc. /10^{20} cm^{-3}**	$\sigma_{ap}/10^{-20}\,cm^2$	$\sigma_{ep}/10^{-20}\,cm^2$	$\sigma_e/10^{-20}\,cm^2$	$\sigma_a/10^{-20}\,cm^2$	λ_p /nm	λ_e /nm	τ / µs	**Ref**
YAG	8.97	0.8	0.159	2.3	0.149	942	1029	951	[33]
YCOB	8.97	1	0.959	0.36	0.026	976.4	1032	2280	[33]
GdCOB	8.97	1.1	1.12	0.5	0.027	975	1035.3	2500	[33]
YAB	8.97	3.4	2.99	0.8	0.04	975	1040.3	680	[33]
KGdW	8.97	12	14.6	2.7	0.289	981	1023.3	600	[33]
KYW	8.97	13.3	16	3	0.299	981.2	1025.3	600	[33]
Sc_2O_3	8.97	4	4	1.2	0.05	975	1041	800	[53]
Y_2O_3	8.97	2.4	2.3	0.85	0.06	975	1031	850	[53]
Lu_2O_3	8.97	3	2.9	1.07	0.07	975	1032	820	[53]
Ta_2O_5	0.6	2.8	2.9	N/A	N/A	975	1030	260	[54]

σ_{ap}: Absorption cross section at pump wavelength

σ_{ep}: Emission cross section at pump wavelength

σ_a: absorption cross section at emission wavelength

σ_e: emission cross section at emission wavelength

λ_p: pump wavelength

λ_e: emission wavelength

τ: excited state lifetime

Table 2.3 shows the optical property differences between the most promising hosts doped by Yb. These differences will lead to a different lasing performance of the Yb systems, for example, slope efficiency and laser threshold. In *Table 2.3*, most of the host materials are crystalline except the Ta_2O_5 which is amorphous. The main difference between amorphous host and crystalline host is the crystalline host has a uniform lattice structure while the amorphous has non-uniform lattice structure. Consequently, the laser with amorphous host will have broader emission and absorption range compared to crystalline host laser. Ideally, a laser system should have large absorption cross section and small emission cross section at pump wavelength to maximize the absorption of the pump energy. It is contrary at emission wavelength that the emission cross section is expected to be large and absorption needs to be small so that the reabsorption of emitted light is minimum. Under these criteria, all the hosts possess a good emission property as their emission cross section at emission wavelength is at least one order magnitude larger than their absorption cross section at the same wavelength. Considering about the cross sections at pump wavelength, YAG shows better performance (absorption cross section is ~6 times larger than emission cross section), which makes it a great host for Yb.

Yb doped solid-state lasers can be made into different formats, for example: thin disk, rod, planar waveguide, etc. In this work, the waveguide laser format has been chosen. Compared with the other forms of laser, waveguide lasers have certain advantages. The most attractive property of the waveguide laser is its compact structure that allows integration with other on-chip devices, especially for optical applications. Other properties like good optical confinement and high degree of thermal immunity also make waveguide a promising format of solid state laser. Combining with the advantages of the ytterbium, Yb doped waveguide laser has attracted a lot of attention from the scientific community.

The first Yb doped waveguide laser was a Yb:YAG planar waveguide laser reported by D. C. Hanna *et al.* [55] The doping was achieved with ion implantation, leaving a ~1.5 μm thick, 6.5 atomic percent (at.%) doped layer located 6 μm under the surface of the YAG planar layer. Lasing at 1030 nm was obtained through a 10 mm long device with an 83% reflectivity mirror on one side and a high reflective mirror on the other. The slope efficiency and threshold power were measured to be 19% and 30mW respectively.

Table 2.4 shows the survey of the recent work of Yb waveguide laser that have been carried out. Similar work of Yb:YAG laser has been done by D. Pelenc *et al.* in 1995 [56]. Instead of using ion implantation, they utilized liquid phase epitaxy to fabricate the Yb:YAG planar waveguide. This resulted in a slope efficiency up to 77%. With a 2% output coupler, the threshold power could be lowered to 43 mW and high laser power of 275 mW at 1048 nm could be obtained. In the same year, J. K. Jones *et al.* demonstrated Yb lasing in a new material - lithium niobate ($LiNbO_3$) [57]. The laser device was made into channel waveguide via diffusion. The threshold for Yb: $LiNbO_3$ was measured to be as low as 15 mW with a 7% output coupler. However, with the coupler mounted on, the output power was not stable.

In 1999, A. A. Lagatsky demonstrated CW lasing in Yb doped potassium gadolinium tungstate ($KGd(WO_4)_2$ or KGW) and Yb doped potassium yttrium tungstate ($KY(WO_4)_2$ or KYW) which brought this new group of host material into sight [58]. Both tungstate bulk crystal lasers can achieve a high slope efficiency of 52% with a 1.1% output coupler and a wide lasing spectral range from 1026 nm to 1044 nm. Lasing near 1 μm was reported with a maximum output power of 290 mW and a record high slope efficiency of 80% under the assist of a 6.2% output coupler in 2006 [59]. 3 years later, F.M. Bain *et al.* reported a liquid phase epitaxy-grown (LPE-grown) monolithic Yb:KYW planar waveguide laser in microchip format. The output power was 148 mW and slope efficiency was 62%

[60]. In the same year, F.M. Bain *et al.* also demonstrated channel waveguide in Yb:KGW [61]. The channel waveguide was realized by applying ultrafast laser inscription to LPE-grown planar layers with maximum output of 18.6 mW and threshold of 100 mW. The slope efficiency was measured to be a very low level of 13.8%.

While exploring the new host material with Yb dopants, the potential of Yb:YAG waveguide lasers still being tested. Jorg Siebenmorgen *et al.* reported a Yb:YAG channel waveguide produced by direct femtosecond laser writing also known as ultrafast laser inscription [62]. Due to the nonlinear absorption process, the femtosecond laser focused inside the YAG crystal leads to a stress induced birefringence, causing a refractive index change and forming a virtual waveguide without a physical boundary. Owing to the smooth interface, the Yb:YAG channel waveguide laser reported in Jorg Siebenmorgen *et al.* work achieved a record high slope efficiency of 75% for monolithic laser devices. The maximum output of this laser was measured to be 800 mW and the threshold 245 mW. With the same fabrication technique, a DBR channel waveguide laser with a slightly lower slope efficiency of 68% but an ultrahigh output power of 2.35 W was demonstrated [63].

Glass is also a favourable host for Yb waveguide lasers. A monolithic Yb doped phosphate glass waveguide laser with a Bragg grating acting as a distributed feedback (DFB) resonator was created using femtosecond laser direct writing in a single step [64]. The output power of this device maximized at 102 mW with a slope efficiency of 17%. In 2012, R. Mary *et al.* achieved lasing in Yb doped bismuthate glass channel waveguide [65]. By using ultrafast laser inscription, a high slope efficiency of 79% was achieved and the laser threshold was found to be as low as 43 mW. For the silicate glass, Guido Palmer *et al.* demonstrated the first Yb:IOG10 (a silicate glass from Schott) channel waveguide laser fabricated by femtosecond laser direct writing [66]. The performance of 72 mW maximum output power and 25% slope efficiency was achieved. The first Yb:ZBLAN (fluorozirconate glass) channel waveguide laser was reported by Guido Palmer *et al.*, with a highest ever slope efficiency of 84% in Yb doped waveguide laser and a maximum lasing power of 170 mW [66].

With the ever-growing demand of compact, integrated waveguide lasers on silicon substrates, lasers using CMOS compatible amorphous films have drawn many attentions. A distributed Bragg reflector (DBR) channel in Yb:Al_2O_3 was realized using re-active co-sputtering, photolithography and reactive ion etching, forming a highly efficient (67%) waveguide laser with 10 mW threshold [67]. Recently, A. Aghajani *et al.* reported an Yb doped Ta_2O_5 rib waveguide laser fabricated by RF sputtering and ion beam milling. The laser threshold of this waveguide device was found to be 29 mW with a slope efficiency of 27% [54].

*Table 2.4 Survey of different Yb doped lasers (*refractive index is measured at 800 nm wavelength otherwise specified in individual cell)*

Host	**KY(WO$_4$)$_2$ [59]**	**Bismuthate glass[65]**	**YAG crystal [56]**	**Al$_2$O$_3$ [67]**	**YAG ceramic [68]**	**Ta$_2$O$_5$ [54]**	**Silicate glass [71]**	**Y$_2$O$_3$ [72]**	**Phosphate glass[64]**	**LiNbO$_3$ [57]**	**Gd$_3$Ga$_5$O$_{12}$ [69]**	**(Gd,Lu)$_2$O$_3$ [70]**
Refractive index*	2	2.03@1304 nm	1.81	1.65	1.829	2.1	1.53	1.91	N/A	2.25	1.95	N/A
Waveguide type	Planar	Channel	Planar	Rib	Channel	Rib	Channel	N/A	Channel	Channel	Rib	Rib
Fabrication method	Liquid phase epitaxy	Ultrafast laser inscription	Liquid phase epitaxy	Reactive ion etch	Fs laser direct write	Ion beam milling	Fs laser direct write	N/A	Fs laser direct write	Diffusion	Ion beam milling	Reactive ion etch
Doping conc.	1.8 at.%	1.6×10^{26}	6.2 at.%	5.8×10^{20}	15 at.%	0.6×10^{20}	8% wt	1.85 at.%	9% wt.	1×10^{20}	N/A	3 at.%
λ_{Pump} / nm	980	975	941	976	945	977	974	965	976	956	941	905
λ_{Laser} / nm	1000	1030	1048	1021	1030	1020 - 1025	1029	1030	1032	1008, 1030, 1060	1025	976
Slope efficiency	80%	79%	77%	67%	65%	27%	25%	20%	17%	16%	13.6%	6.7%
Threshold / mW	80	35	43	10	245	29	44	N/A	116	15	80	17
Year published	2006	2012	1995	2011	2011	2015	2013	2014	2009	1995	1996	2009

Host	YAG crystal [55]	KGd(WO$_4$)$_2$ [58]	KY(WO$_4$)$_2$ [49]	KY(WO$_4$)$_2$ [60]	KGd(WO$_4$)$_2$ [61]	YAG [62]	YAG [63]	IOG10 [66]	ZBLAN[66]
Refractive index*	N/A	N/A	N/A	N/A	N/A	N/A	N/A	N/A	N/A
Waveguide type	Planar	Planar	Planar	Planar	Channel	Channel	Channel	Channel	Channel
Fabrication method	Liquid phase epitaxy	Liquid phase epitaxy	Liquid phase epitaxy	Liquid phase epitaxy	Fs laser direct write	Fs laser direct write	Fs laser direct write	Fs laser direct write	Fs laser direct write
Doping conc.	6.5 at.%	5 at.%	5 at.%	3 at.%	5 at.%	7 at.%	7 at.%	2.5at.%	8% wt.
λ_{Pump} / nm	980	980	980	980	980	941	940/970	974	974
λ_{Laser} / nm	1030	1026 - 1044	1026 - 2044	1040	1023	1063	1029	1030	1030
Slope efficiency	19%	53%	52%	62%	13.8%	75%	68%	25%	84%
Threshold / mW	30	340	251	40	100	245	183	44	25
Year published	1993	1999	1999	2009	2009	2010	2011	2013	2013

2.8 Summary

In this chapter, an overview of laser is presented. Three fundamental optical transitions between energy levels (absorption, spontaneous emission and stimulated emission) and their Einstein equations are demonstrated. The transition cross sections that quantifying the probability of absorption and emission are then introduced. Following by this, the general lasing conditions are discussed.

Further to the basic concepts of laser, different working mechanisms of active ion in solid state lasers are discussed. Depending on different purposes of lasers, one ion interaction may be desirable for one laser system where the other systems see it as loss mechanism. The standard laser process is an exception because it is the cornerstone of lasing – without this process, there will be no emission. The other single ion process, resonant multi-photon absorption, is desired in upconversion laser system but is not wanted in standard laser system. Among the multi-ion interactions, co-operative upconversion and co-operative emission are favourable in upconversion laser systems while cross-relaxation is regarded as loss mechanism. Energy migration is the key for laser systems that co-doped with sensitizers but introduces loss in the other types of laser system.

After explaining the mechanisms of the active ion, an introduction of commonly used active ions and amorphous hosts for solid state lasers is given. Among the transition metals and rare-earth elements, ytterbium (Yb) has been chosen as the active ion for this work because around 1 μm emission wavelength, Yb possesses the advantages of no upconversion, low quantum defects and narrow emission line width. Owing to the wide transparent range, great compatibility of hosting rare-earth elements and low phonon energy, tantalum pentoxide (Ta_2O_5) has been picked as the host material for hosting the Yb.

At the end of this chapter, recent development of Yb doped solid state waveguide laser has been reviewed. The highest slope efficiency ever found is 84%, reported by Guido Palmer *et al.*, from an Yb:ZBLAN waveguide with cross sectional diameter of 13 μm (equivalent to 132.66 μm^2). The lowest threshold to date is 10 mW, discovered in an Yb:Al_2O_3 waveguide with cross sectional area of 2.5 μm^2. In this work, the property of Yb:Ta_2O_5 will be investigated, seeking to achieve a state-of-art waveguide laser device.

Bibliography

[1] T. H. Maiman, "*Stimulated Optical Radiation in Ruby*", Nature **187**, 493 – 494 (1960)

[2] A. Einstein, "*Strahlungs-Emission und -Absorption nach der Quantentheorie*", Deutsche Physikalische Gesellschaft, **18**, 318-323 (1916)

[3] A. Javan *et al.*,"*Population Inversion and Continuous Optical Maser Oscillation in a Gas Discharge Containing a He-Ne Mixture*". Physics Review Letter **6,** No.3, 106–110 (1961)

[4] R. Hall *et al.*, "*Coherent Light Emission From GaAs Junctions*", Physical Review Letters. **9** (9): 366–369 (1962)

[5] C. J. Koester, "*Amplification in a Fiber Laser*", Appl. Opt. 3, 1182-1186 (1964)

[6] J. E. Geusic, "*Laser Oscillations in Nd-doped Yttrium Aluminum, Yttrium Gallium And Gadolinium Garnets*" Appl. Phys. Lett. 4, 182 (1964)

[7] R. C. Hilborn, "*Einstein coefficients, cross sections, f values, dipole moments, and all that*", American Journal of Physics 50, 982 (1982)

[8] W. T. Silfvast, Laser Fundamentals 2nd ed., Cambridge, 2004

[9] D. E. McCumber, "*Einstein Relations Connecting Broadband Emission and Absorption Spectra*", Phys. Rev. 136, A954 (1964)

[10] W. Koechner *et al.*, Solid-State Lasers - A Graduate Text, Springer (2003)

[11] W. P. Risk, Compact Blue-Green Lasers, Cambridge Press (2003)

[12] A.J. Kenyon, "*Recent developments in rare-earth doped materials for optoelectronics*", Progress in Quantum Electronics **26**, 225–284(2002)

[13] Wei-Ping Qin et al., "*Multi-ion cooperative processes in* Yb^{3+} *clusters*", Light: Science & Applications, **3**, page e193 (2014)

[14] S. B. Mirov, V. V. Fedorov, "*Recent Progress in Transition-Metal-Doped II–VI Mid-IR Lasers*", IEEE Journal of Selected Topics in Quantum Electronics, **13**, No. 3, 810 - 822 (2007)

[15] R. H. Page *et al.*, "Cr^{2+}*-doped sinc chalcogenides as efficient, widely tunable mid-infrared lasers*", IEEE Journal of Quantum Electronics, **33**, No. 4, 609–619 (1997)

[16] P. W. Roth *et al.*, "*Directly diode-laser-pumped Ti:sapphire laser*", Optics Letters, **34** (21), 3334 (2009)

[17] W. B. Bridges, "*Laser Oscillation In Singly Ionized Argon In The Visible Spectrum*", Appl. Phys. Lett. **4**, 128–130 (1964)

[18] E. V. Zharikov *et al.*, "*Stimulated emission from* Er^{3+} *ions in yttrium aluminum garnet crystals at* $\lambda = 2.94\ \mu m$", Soviet Journal of Quantum Electronics, **4**, 1039(1975)

[19] W. Seka *et al.*, "*Demonstration of high efficiency third harmonic conversion of high power Nd-glass laser radiation*", Optics Communications, **34**, 3, 469–473 (1980)

[20] G. N. van den Hoven *et al.*, "*Absorption and emission cross sections of* Er^{3+} *in* Al_2O_3 *waveguides*", Applied Optics, **36**, 15, 3338-3341 (1997)

[21] Z.W. Zhao *et al.*, "*Microstructural and optical properties of aluminum oxide thin films prepared by off-plane filtered cathodic vacuum arc system*", Journal of Vacuum Science & Technology A, **21**, 906-910 (2003)

[22] X. Multone *et al.*, "*Er-doped* Al_2O_3 *thin films deposited by high-vacuum chemical vapor deposition (HV-CVD)*", Materials Science and Engineering B, **146**, 35–40 (2008)

[23] O. P. Y Moll *et al.*, "Eu^{3+}*- and* Tm^{3+}*- Doped Yttrium Oxide Thin Films for Optical Applications*", Journal of Luminescence, **87-89**, 1115-1117 (2000)

[24] I. Hyppanen *et al.*," *Upconversion Properties of Nanocrystalline* ZrO_2:Yb^{3+}, Er^{3+} *Phosphors*", Journal of Nanomaterials, Article ID 16391, 8 pages (2007)

[25] Richard KBrow, "*Review: the structure of simple phosphate glasses*", Journal of Non-Crystalline Solids, Volumes 263–264, Pages 1-28 (2002)

[26] Catalin Florea *et al.*, "*Ytterbium-Doped Glass Waveguide Laser Fabricated by Ion Exchange*", JOURNAL OF LIGHTWAVE TECHNOLOGY, VOL. 17, NO. 9, (1999)

[27] K. V. Krishnaiah *et al.*, "*Development of ytterbium-doped oxyfluoride glasses for laser cooling applications*", Scientific Reports, **6**, Article number: 21905 (2016)

[28] V. Ter-Mikirtychev, Fundamentals of Fiber Lasers and Fiber Amplifiers, Springer (2013)

[29] A. Bahtata, M. Bouazaoui," *Upconversion fluorescence spectroscopy in* Er^{3+}: TiO_2 *planar waveguides prepared by a sol-gel process*", Journal of Non-Crystalline Solids, **202**, 16-22 (1996)

[30] R. Kapoor *et al.*, "*Highly efficient infrared-to-visible energy upconversion in* Er^{3+}:Y_2O_3", Optics Letters, **25**, 5, 338-340 (2000)

[31] S.J. Pearcea *et al.*, “*Structural characteristics and optical properties of plasma assisted reactive magnetron sputtered dielectric thin films for planar waveguiding applications*”, Surface and Coatings Technology, **206**, 23, 4930–4939 (2012)

[32] C. Li *et al.*, “*106.5 W high beam quality diode-side-pumped Nd:YAG laser at 1123 nm*”, Optical Express **18**, 8, 7923 (2010)

[33] A Brenier, “*A new evaluation of* Yb^{3+}*-doped crystals for laser applications*”, Journal of Luminescence, **92**, 3, 199-204(2001)

[34] J. Kong *et al.*, “*9.2-W diode–end–pumped Yb:Y2O3 ceramic laser*”, Applied Physics Letters 86, 161116 (2005)

[35] P. A. Murawala *et al.*, "*Structural and Electrical Properties of* Ta_2O_5 *Grown by the Plasma-Enhanced Liquid Source CVD Using Penta Ethoxy Tantalum Source*". Japanese Journal of Applied Physics, **32** (Part 1, No. 1B): 368–375 (1993)

[36] K. Kukli *et al.*, "*Properties of tantalum oxide thin films grown by atomic layer deposition*". Thin Solid Films **260**, 2, 135–142 (1995)

[37] H. Sawada *et al.*, "*Electronic structure of oxygen vacancy in* Ta_2O_5". Journal of Applied Physics, **86**, 2, 956-960 (1999)

[38] T. W. Huang *et al.*, “*Braodband Tunable 1060 nm Fiber Ring Laser Band on Hybrid Amplifier with 45 nm Tuning Range*” , IEEE Conference on Cross Strait Quad-Regional Radio Science and Wireless Technology, 270-273 (2011)

[39] P.S. Dobal *et al.*, “*Raman scattering study of a phase transition in tantalum pentoxide*”, Journal of Raman Spectroscopy, **31**, 1061-1065(2000)

[40] K. Kiura *et al.*, “*Fabrication of Tm-doped* Ta_2O_5 *thin films using a co-sputtering method*”, Results in Physics **Volume 4**, 2014, Pages 148-149

[41] G. N. van den Hoven *et al.*, “*Upconversion in Er-implanted* Al_2O_3 *waveguides*”, Journal of Applied Physics **79**, 1258 (1996)

[42] X. Zhao *et al.*, “*Phonons and lattice dielectric properties of zirconi*a”, PHYSICAL REVIEW B, **VOLUME 65**, 075105 (2002)

[43] R. J. Gonzalez *et al.*, “*Infrared reflectivity and lattice fundamentals in anatase* TiO_2”, PHYSICAL REVIEW B, **VOLUME 55**, Number 11 (1997)

[44] R. Lo Savio *et al.*, "*Concentration dependence of the* Er^{3+} *visible and infrared luminescence in* $Y_{2-x}Er_xO_3$ *thin films on Si*", Journal of Applied Physics **106**, 043512 (2009)

[45] C. A. Wang *et al.*, "*New materials for diode laser pumping of solid-state lasers*" , IEEE Journal of Quantum Electronics, **28**, 942-957 (1992)

[46] J.K Sahu *et al.*, "*A 103 W erbium–ytterbium co-doped large-core fiber laser*", Optics Communications, Vol. 227, **1-3**, 159-163 (2003)

[47] B. Peng *et al.*, "*Optical properties, fluorescence mechanisms and energy transfer in* Tm^{3+}, Ho^{3+} *and* Tm^{3+} -Ho^{3+} *doped near-infrared laser glasses, sensitized by* Yb^{3+}" , Optical Materials, Vol. 4, **6**, 787-810 (1995)

[48] L. Batay *et al.*, "*Efficient tunable laser operation of diode- pumped* Yb,Tm:KY(WO_4)$_2$ *around 1.9 µm*", Applied Physics B, **75**, 457 (2002)

[49] G. Liu *et al.*, Spectroscopic Properties of Rare Earths in Optical Materials, Springer

[50] X. Hou *et al.*, "*Investigation of the spectroscopic properties of highly transparent* Yb:$(Y_{0.97}Zr_{0.03})_2O_3$ *ceramic*", Optical Materials, **32**, 11, 1435–1440(2010)

[51] W. G. Perkins *et al.*, "*CrystalField Splitting in* Yb^{3+} *Chelates*", The Journal of Chemical Physics, **42**, 407 (1965)

[52] H. M. Pask *et al.*, "*Ytterbium-Doped Silica Fiber Lasers: Versatile Sources for the 1-1.2 µm Region*", IEEE Journal of Selected Topics in Quantum Electronics, **1**, 1, 2-13 (1995)

[53] A Brenier *et al.*, "*Overview of the best* Yb^{3+}*-doped laser crystals*", Journal of Alloys and Compounds, Volumes 323–324, 210-213(2001)

[54] A. Aghajani *et al.*, "*Waveguide lasers in ytterbium-doped tantalum pentoxide on silicon*", Optics Letters, **40**, No.11 2549 (2015)

[55] D. C. Hanna *et al.*, "*Quasi-three level 1.03 µm laser operation of a planar ion-implanted Yb:YAG waveguide*", Optics Communication, **99**, 211-215 (1993)

[56] D. Pelenc *et al.*, "*High slope efficiency and low threshold in a diode-pumped epitaxially grown Yb: YAG waveguide laser*", Optics Communication, **115**, 491-497 (1995)

[57] J. K. Jones *et al.*, "*Channel waveguide laser at 1 mm in Yb-indiffused* $LiNbO_3$", Optical Letters, **20**, No. 13, 1477 (1995)

[58] A.A. Lagatsky *et al.*, "*Diode-pumped CW lasing of Yb:KYW and Yb:KGW*", Optics Communication, **165**, 71-75 (1999)

[59] Y. E. Romanyuk *et al.*, "*Yb-doped $K(WO_4)_2$ planar waveguide laser*", Optical Letters, **31**, No. 1, 53 (2006)

[60] F.M. Bain *et al.*, "*Continuous-wave and Q-switched operation of a compact, diode-pumped $Yb^{3+}:KY(WO_4)_2$ planar waveguide laser*", Optical Express, **17**, No. 3, 1666 (2009)

[61] F.M. Bain *et al.*, "*Ultrafast laser inscribed $Yb:KGd(WO_4)_2$ and $Yb:KY(WO_4)_2$ channel waveguide lasers*", Optical Express, **17**, No. 25, 22417 (2009)

[62] J. Siebenmorgen *et al.*, "*Highly efficient Yb:YAG channel waveguide laser written with a femtosecond-laser*", Optical Express, **18**, No. 15, 16035 (2010)

[63] T. Calmano *et al.*, "*Diode pumped high power operation of a femtosecond laser inscribed Yb:YAG waveguide laser*", Optical Material Express, **1**, No. 3, 428 (2011)

[64] M. Ams *et al.*, "*Monolithic 100 mW Yb waveguide laser fabricated using the femtosecond-laser direct-write technique*", Optics Letters, **34**, No. 3, 247 (2009)

[65] R. Mary *et al.*, "*Compact, highly efficient ytterbium doped bismuthate glass waveguide laser*", Optics Letters, **37**, No. 10, 1691 (2012)

[66] G. Palmer *et al.*, "*High slope efficiency and high refractive index change in direct-written Yb-doped waveguide lasers with depressed claddings*", Optical Express, **21**, No. 14, 17413 (2013)

[67] E. H. Bernhardi *et al.*, "*Highly efficient, low-threshold monolithic distributed-Bragg-reflector channel waveguide laser in $Al_2O_3:Yb^{3+}$*", Optics Letters, **36**, No. 5, 603 (2011)

[68] T. Calmano *et al.*, "*Characterization of an Yb:YAG ceramic waveguide laser, fabricated by the direct femtosecond-laser writing technique*", Applied Physics B: Lasers and Optics, **103**, 1-4 (2011)

[69] M. Shimokozono *et al.*, "*Room-temperature operation of an Yb-doped $Gd_3Ga_5O_{12}$ buried channel waveguide laser at 1.025 µm wavelength*", Applied Physics Letters, **68**, 2177 (1996)

[70] H. Kühn *et al.*, "*Monocrystalline Yb^{3+}: $(Gd, Lu)_2O_3$ channel waveguide laser at 976.8 nm*", Optics Letters, **34**, No.18, 2718 (2009)

[71] C. Florea *et al.*, "*Ytterbium-Doped Glass Waveguide Laser Fabricated by Ion Exchange*", Journal of Lightwave Technology, Vol. **17**, No. 9, 1593 (1999)

[72] L. D. Merkle *et al.*, “*Temperature-dependent lasing and spectroscopy of Yb: Y_2O_3 and Yb: Sc_2O_3*”, Optics Communications, Vol. **281**, Issue 23 (2008)

Chapter 3: Device Design and Simulation

3.1 Introduction

There are several different variations of solid state lasers, e.g. thin disk, rod, planar waveguide, etc. Compared with the other available varieties, waveguide laser has several advantages such as compact structure, good optical confinement and high degree of thermal immunity.

In this chapter, the loss mechanisms such as coupling loss and waveguide loss that affects waveguide performance are discussed. Waveguide design that can minimize the discussed loss mechanisms are presented. Three different types of waveguides including strip loaded, SiO_2 buried channel and polymer based buried channel are proposed.

Mode simulation is carried out to confirm the spot size and confinement of the fundamental mode that propagates inside the different waveguides with different width. Following the mode simulation, a gain simulation is performed to simulate the waveguide gain as a function of launched pump power and the theoretical maximum gain of the waveguide.

3.2 Design consideration

To design a waveguide laser device, one has to consider not only the material that is used for light amplification but also the geometry of the waveguide that affects the loss and modes spot size of the waveguide.

The loss mechanisms of an optical pumped solid state waveguide laser system are coupling losses and waveguide losses[1].

3.2.1 **Coupling Loss**

The coupling loss consists of the Fresnel reflection and the mismatch between the pump beam profile and the effective mode of the waveguide. *Figure 3.1* gives the side view of how an incident beam is coupled into the waveguide via direct focusing by a lens and also marks the place where coupling loss occurs.

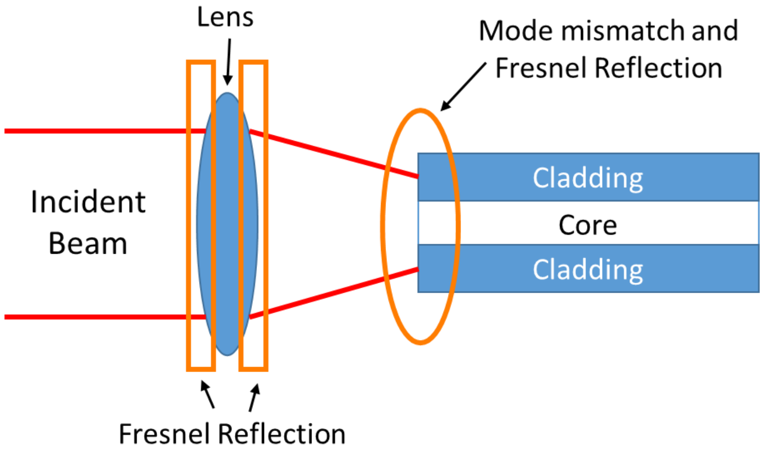

Figure 3.1 Schematic of coupling loss when pumping light into the waveguide

3.2.1.1 **Mode Mismatch**

The transfer of the pump beam energy to the waveguide mode is accomplished by matching the beam-field to the waveguide mode field. *Figure 3.2 (a)* shows an example of the mode mismatch. The orange ellipse is the incident beam mode, the grey rectangular is the waveguide and the blue ellipse is the mode that can propagate in the waveguide. *Figure 3.2 (b)* displays the mode intensity profile over the x-axis for the incident beam and the mode that propagates in the waveguide.

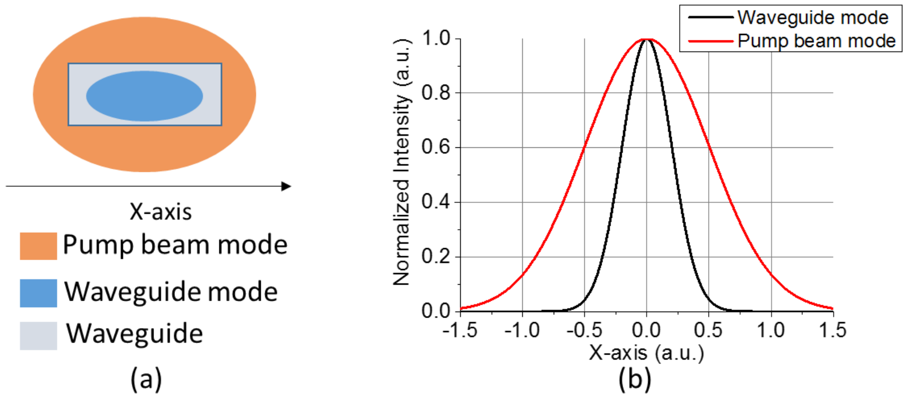

Figure 3.2 (a) Simplified example of mode mismatch; (b) Normalized mode intensity profile for incident beam and waveguide mode on x-axis

In the case of pump beam mode is larger than the waveguide mode, the overlay integral of the beam mode and waveguide mode reduces indicating that less energy is coupled into the waveguide. Therefore, the pump power needed for achieving lasing will increase.

Since the incident pump beam is coupled into the waveguide using a focusing lens, picking the right lens can minimize the mismatching. *Figure 3.3* shows the laser beam that would obtain when focused by an aspheric focusing lens with a focal length of z under the consideration of ray-optic assumption or the diffraction assumption.

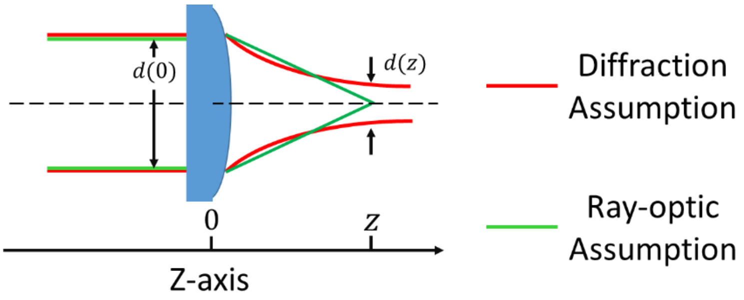

Figure 3.3 Gaussian beam path and ray-optic beam path after an aspheric focusing lens

In practical case, the focused beam spot is limited by diffraction. The relationship between the focused beam spot diameter $d(z)$ at focal point (distance z) and the unfocused beam spot diameter $d(0)$ can be expressed by[2]:

$$d(z) = \frac{4\lambda z}{\pi d(0)} \qquad Eq. 3-1$$

where λ is the wavelength of the incident beam.

Therefore, by applying the wavelength and the beam radius into the equation, one can estimate the radius of the focused beam spot for a certain focusing lens. Thus, the coupling loss can be minimized by matching the focusing lens and the waveguide design.

3.2.1.2 **Fresnel Reflection**

Fresnel reflection is caused by the change of refractive index on the light path which in our case is an air – focusing lens – air – laser medium. Due to the Fresnel reflection, only part of the incident light can enter the laser medium. *Figure 3.4* illustrates the light transmission and reflection at the interface of two different materials.

According to the Fresnel equations, the reflectance of the interface between two mediums with refractive index of n_1 and n_2 can be expressed as:

$$R_s = \left|\frac{\mathrm{n}_1 \cos\theta_i - \mathrm{n}_2 \cos\theta_t}{\mathrm{n}_1 \cos\theta_i + \mathrm{n}_2 \cos\theta_t}\right|^2 \qquad Eq. 3-2$$

$$R_p = \left|\frac{\mathrm{n}_1 \cos\theta_t - \mathrm{n}_2 \cos\theta_i}{\mathrm{n}_1 \cos\theta_t + \mathrm{n}_2 \cos\theta_i}\right|^2 \qquad Eq. 3-3$$

where R_s and R_p are the reflectance for s-polarization and p-polarization respectively, n_1 and n_2 are the refractive indices of the two different medium, θ_i is the incident angle of light, θ_t is the transmission angle of the light.

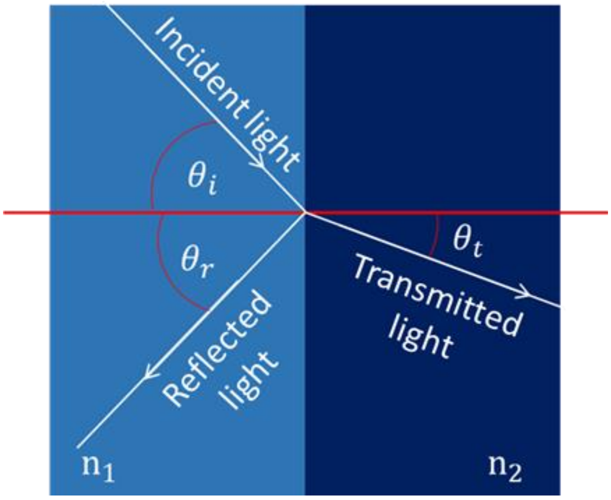

Figure 3.4 Schematic of Fresnel reflection

Therefore, the transmittances for s-polarization and p-polarization can be given by:

$$T_s = 1 - R_s \qquad Eq.3-4$$

$$T_p = 1 - R_p \qquad Eq.3-5$$

If the incident light is unpolarized, the reflectance yields:

$$R = \frac{R_s + R_p}{2} \qquad Eq.3-6$$

Thus, the total transmittance is:

$$T = 1 - R \qquad Eq.3-7$$

According to the Eq.3-2 and Eq.3-3, the Fresnel reflection loss depends on the refractive indices of the focusing lens and the laser medium. Therefore, transmittance could be improved by carefully choosing the material for the lens and laser medium or applying anti-reflection (AR) coating onto the interfaces.

3.2.2 **Waveguide Loss**

Waveguide loss is the loss that is caused by the defects or the properties of the waveguide itself (e.g. fabrication imperfections and waveguide materials). It can be divided into three categories: scattering loss, absorption loss and radiation loss.

3.2.2.1 **Scattering Loss**

There are two types of scattering loss in the optical waveguide: volume scattering and surface scattering. The basic schematic of these two scattering processes is shown in *Figure 3.5*.

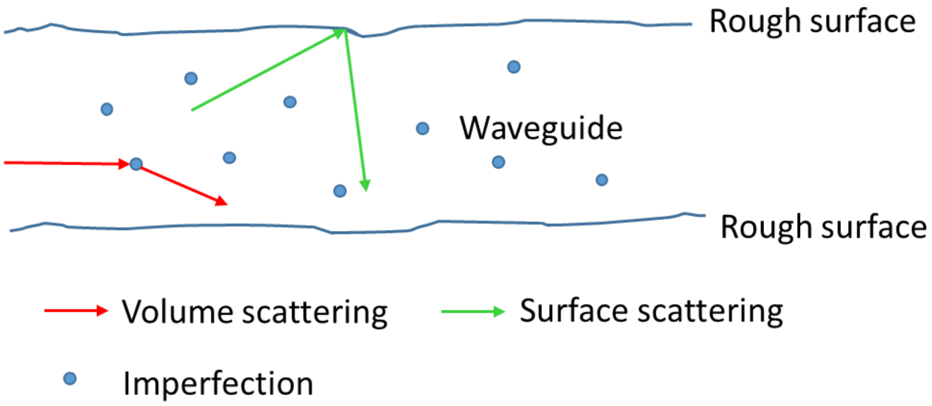

Figure 3.5 Schematics of volume and surface scattering

Volume scattering is caused by imperfections inside the waveguide. The imperfections can be contaminant atoms in the structure or crystalline defects. The volume scattering loss is proportional to the density of the imperfections. Volume scattering also strongly depends on the relative size of the imperfections in comparison with the wavelength of the light λ that is traveling within the waveguide. When the size of an imperfection is near or larger than λ, the volume scattering loss is significant. When the size of imperfection is much smaller than λ, the volume scattering loss is negligible.

The surface scattering loss is caused by the surface roughness of the waveguide. Thus, the more the propagating mode has contact with the rough surface, the higher the surface scattering loss it suffers. As a result, higher order modes that have larger mode surface will have higher loss compared to low order modes that propagates in the same waveguide.

3.2.2.2 **Absorption Loss**

Absorption loss is caused due to the absorption of light by the waveguide material. It contains two parts, the interband absorption and the intraband absorption. *Figure 3.6* is an example of possible transitions in the waveguide, with the interband absorption labelled as green and intraband absorption as red.

The interband absorption occurs when photons with energy that is larger than the bandgap energy of the waveguide material have been pumped into the waveguide. For detailed information about this absorption process one can refer to Section 2.2.1.

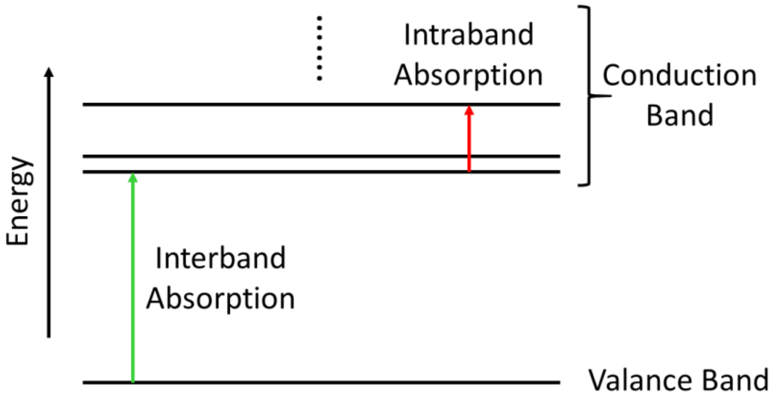

Figure 3.6 Schematics of interband absorption (green) and intraband absorption (red)

Intraband absorption occurs when a photon transfers its energy to an electron already in excited state and promotes the electron to higher state. This process is also known as excited state absorption (ESA).

As the absorption is related to the material, once the waveguide material has been determined, the absorption loss for certain wavelength is fixed. For most solid state lasers that are formed by a host and a dopant material, the absorption caused by the dopant is desired for bringing the laser into the excited state. The absorption from the host is regarded as loss, since the host is not providing any gain for the laser.

3.2.2.3 **Radiation Loss**

Radiation losses are the loss of optical energy caused by the electromagnetic wave escaping the waveguide cavity. This loss is usually significant when the waveguide is bent. However, for planar or straight channel waveguides, the radiation loss is negligible because of their well-confined modes.

3.3 Waveguide Design

The aim of this project is to realize a compact, high power solid state waveguide lasers. Recalling from the Section 3.1, the loss of a solid state waveguide laser can be divided into two groups: the coupling loss and the waveguide loss. Since the Fresnel reflection and absorption are fixed as the focusing optics and waveguide material are decided, the loss variables are the loss caused by mode mismatching and scattering losses. For a carefully fabricated waveguide, scattering losses can be significantly reduced. Because mode mismatching is related to the focused pump spot size and the waveguide size, the waveguide needs to be well-designed to achieve a low amount of losses.

3.3.1 **Waveguide Configuration**

Figure 3.7 (a) illustrates the top view of the waveguide design which has been previously proved to be low loss by M. F. A. Muttalib *et al.*[3]. The waveguide can be divided into three parts: the nanowire (part A), the coupler (part B) and the taper (part C). Each of these parts are designed for different purposes.

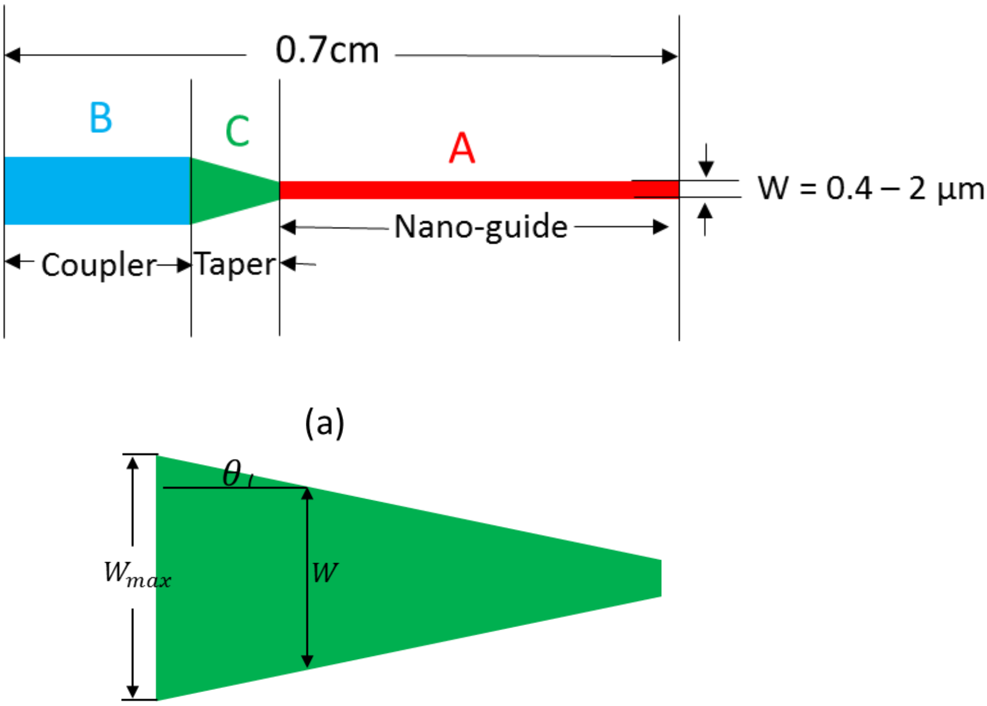

(a)

(b)

Figure 3.7 (a) Top view of the waveguide design and (b) Taper design parameters

The nanowire (Part A) is the key part of the waveguide design. It has been designed in a small scale in order to create a high power density which can effectively lower the laser threshold. The width of the nanowire varies from 400 nm to 2 μm with a step of 200 nm (i.e. 400 nm, 600 nm and so forth). The performance of these different sizes of nanowires will be investigated in order to find the best one for fabricating a high performance laser. The length of the nanowire varies from 1 mm to 2.5mm, which allows us to use the “cut back” method to deduce the loss of the nanowire.

As mentioned in Section 3.1.1, the mode mismatch is caused by the different size of the focused incident beam spot, and the waveguide mode. According to Eq. 3-1, The diameter of focused beam spot after the best aspheric lens (in terms of highest NA ~0.68 and shortest focal length ~3.1mm) that in stock is calculated to be 1.44 μm. As the size of most nanowire is smaller than this value, the mode mismatch is quite large, leading to a high coupling loss. Therefore, a coupler (Part B) with larger dimension that can reduce the mode mismatch when included into the design. The width of the coupler is designed to be 5 µm, leaving enough margin for any possible alignment error.

Similarly, the coupler and the nanowire cannot be connected directly as the size difference is large. Hence, a taper section (Part C) is added between the coupler and the nanowire in order to reduce the coupling loss between the coupler and the nanowire. The taper has been designed as a shallow taper with a ratio of 500:1 (i.e. for 1 unit length change in width, there will be a 500 unit change in length). The reason of having this ratio is to make the taper operate adiabatically. In other words, the lowest order mode that the waveguide can support must propagate through the waveguide without cumulative power transfer to higher order modes [8,9]. For adiabatic operation, the waveguide must comply to a design rule that:

$$\theta < \frac{\lambda_0}{2Wn_{eff}} \qquad Eq. 3-8$$

Where for a given position in the taper z, θ is the half angle of the trapezoid, W is the taper width, λ_0 is the light wavelength at vacuum and n_{eff} is the effective index of lowest order mode at position z. With 500:1 taper ration, the threshold angle θ is calculated to be 0.0572°. Taking λ_0 as 1.06 µm, the minimum angle that occurs at 5 µm width is 0.0575°, which is larger than the threshold angle, confirming the adiabatic operation is available in this taper design. Therefore, the coupling of fundamental mode from coupler to nano-guide is smooth.

3.3.2 **Waveguide Type**

Apart from the shape of the waveguide, the type of waveguide is also very important. In this section, three different types of waveguide were proposed.

Figure 3.8 shows the design of the strip loaded waveguide. In this design, the planar layer is made by an Yb:Ta_2O_5 thin film. The strip material has been chosen as pure Ta_2O_5 because Ta_2O_5 has a refractive index that is close to the core layer and there is an existing mature high profile etching process for it. Due to the strip being the only layer that needs etching, the challenge of Yb:Ta_2O_5 etching is bypassed. Both the top and bottom cladding have been chosen as SiO_2, creating a high refractive index contrast (~0.65) with the strip and the core. As mentioned in Section 3.3.1, the width of the waveguide w varies from 400 nm to 2 µm. Both core material layers have been designed to be 400 nm thick. This thickness has been chosen in order to allow high power density within the waveguide as well as maintaining good mode matching with the pump beam.

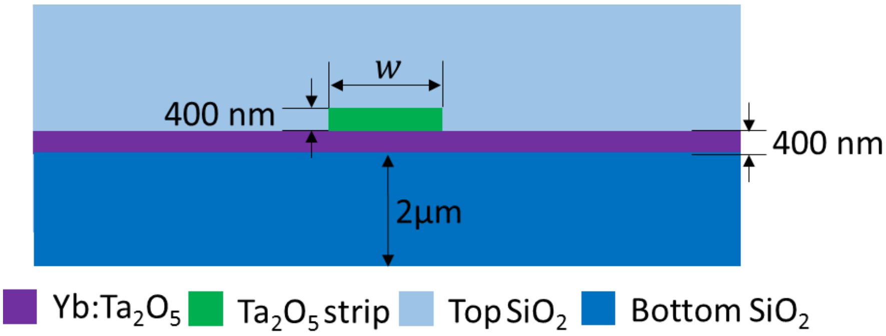

Figure 3.8 *Cross section view of strip loaded waveguide*

Figure 3.9 illustrates the design of the buried channel waveguide. The buried channel waveguide has an Yb:Ta_2O_5 channel waveguide buried into SiO_2 cladding. Due to the channel waveguide providing two-dimensional confinement, it offers more efficient restriction of light inside the waveguide, in other words, higher power density inside the waveguide.

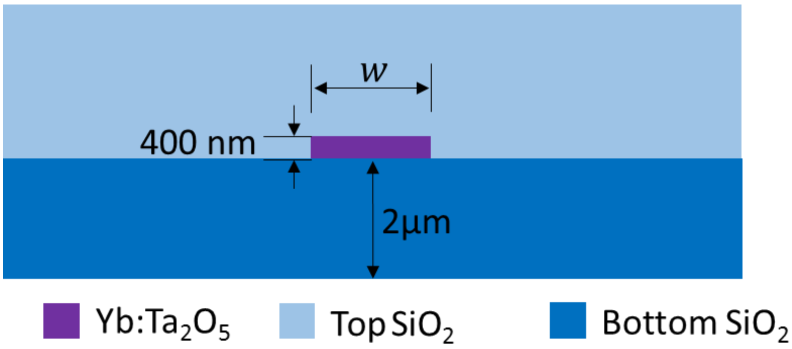

Figure 3.9 *Cross section view of buried channel waveguide*

Polymer based devices using nano-imprint technology have received a lot of attention due to their simplicity in providing an alternative fabrication method for those materials that are hard to pattern. The ability for mass production and its comparably low cost are also very attractive for industrial as well as academic applications.

By applying nano-imprint technology, the Yb:Ta_2O_5 etching process can be avoided. Instead of etching the core material, the core material has been deposited into the trench which is imprinted on the substrate. As the waveguide is still formed as a buried channel, the confinement is expected to be strong. Hence, using the nano-imprint method can reduce the losses caused by etching while still maintaining a strong confinement of the light propagating inside it.

Figure 3.10 displays the cross section of the designed buried channel waveguide geometry. Both the top and bottom cladding used is an inorganic-organic hybrid polymer called Ormocore. This material is a low loss (0.23 dB/cm at 1100nm) transparent polymer with a refractive index of ~1.54

at 1100 nm. To make the device comparable to the conventional Si-based buried channel waveguide, the thickness of the waveguide has been designed to be 400 nm.

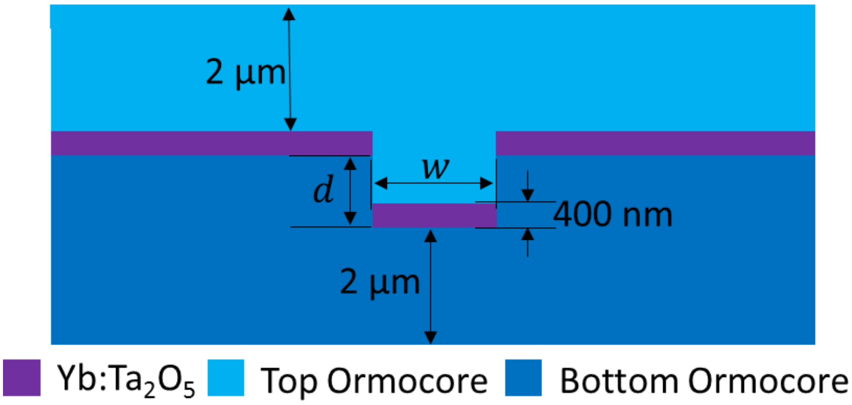

Figure 3.10 Cross section view of polymer based buried channel waveguide

3.4 Simulations

This section presents the simulation configurations and results of the fundamental mode propagating within the strip loaded and buried channel waveguide structures as well as the $Yb:Ta_2O_5$ gain simulation based on the parameters that taken from literatures.

3.4.1 Mode Profile Simulation

The mode profile simulation was carried out using Finite Difference Eigenmode (FDE) solver from Lumerical Mode solutions. The solver calculates the spatial profile and frequency dependence of the mode by solving Maxwell’s equations on a cross-sectional mesh of the waveguide.

3.4.1.1 Simulation Configuration

Figure 3.11 shows the geometry of the simulation model of the nanowire part of the strip loaded waveguide. In the simulation, the thickness of each layer was kept constant but the width w varies from 400 nm to 2 µm.

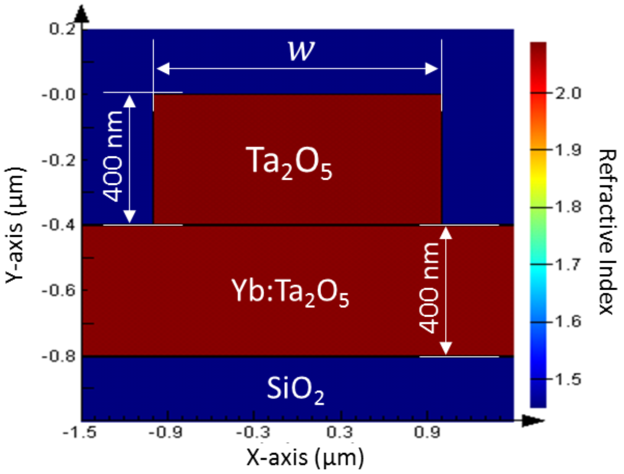

Figure 3.11 Geometric and material setup for strip loaded waveguide simulation

The wavelength of the laser source used in the simulation was set to 1100 nm. The mesh size of the simulation was set to 10 nm for the horizontal direction (x axis) and 5 nm for the vertical direction (y axis) to ensure that the simulation is accurate enough. The stability factor was set to 0.95 to make the simulation stable.

Figure 3.12 shows the geometry used for the simulation of the nanowire part of the buried channel waveguide. The width w of the channel waveguide was also set to vary from 400 nm to 2 µm.

Similarly as for the simulation set up of the strip loaded waveguide, the mesh size was set to 10 nm, and 5 nm for x and y direction, respectively. The stability factor was set to 0.95 to make the simulation stable.

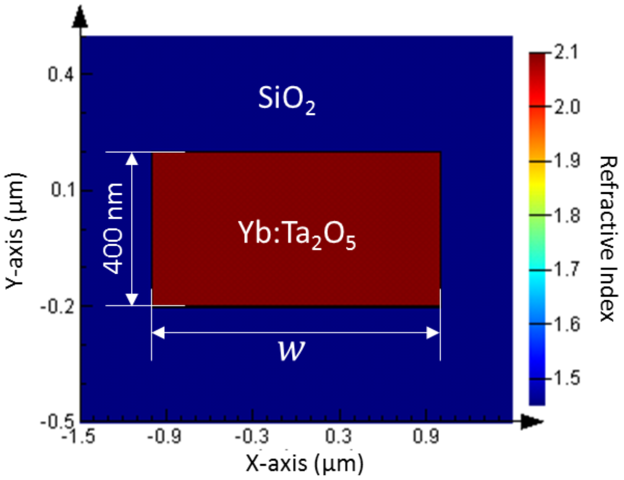

Figure 3.12 Geometric and material setup for buried channel waveguide

Since both the Si based and polymer based buried channel waveguide share the same waveguide core structure, the geometries that were used for both waveguide simulations are the same. The only difference in simulation configuration between these two types of buried channel waveguide is the cladding refractive index – Ormocore has higher (~1.54 at 1100 nm) refractive index than SiO_2 (~1.45 at 1100 nm). *Figure 3.13* displays the geometry and refractive index of the simulated waveguide.

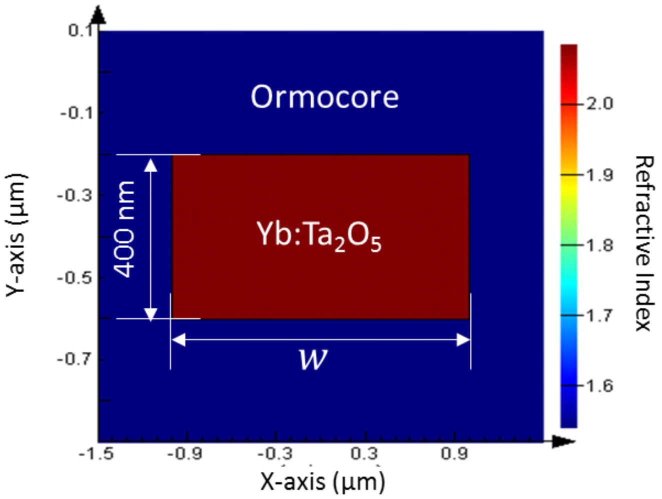

Figure 3.13 Geometric and material setup for polymer based buried channel waveguide

3.4.1.2 **Simulation Results**

In this section, simulation results of mode profile for different types of waveguide were presented together with mode spot size (in full width half maximum) and mode confinement.

3.4.1.2.1 **Strip Loaded Waveguide**

Figure 3.14 (a), (b) and (c) displays the mode profile of the light propagating in the strip loaded waveguide with nanowire width of 2 μm, 1 μm and 400 nm, respectively. For all three simulated waveguides, the modes have a good overlap with the waveguide. For 2 μm nanowire waveguide, the parts of the mode that travels in strip and planar layer are almost symmetric. However, with the narrowing of the nanowire, the mode is more likely to travel in the planar layer rather than the strip. At narrowest nanowire (400 nm), the mode propagates almost fully in the planar layer but its direction is still guided by the strip. In the simulated mode profile in the *Figure 3.14*, it is clear to see that with the narrowing of the nanowire, the modal overlap with the sidewall of the waveguide becomes larger. As a consequence of this, when the waveguide sidewall is not perfect smooth (which it will not be in practical case) the mode propagates inside the narrower waveguide will suffer higher propagating loss.

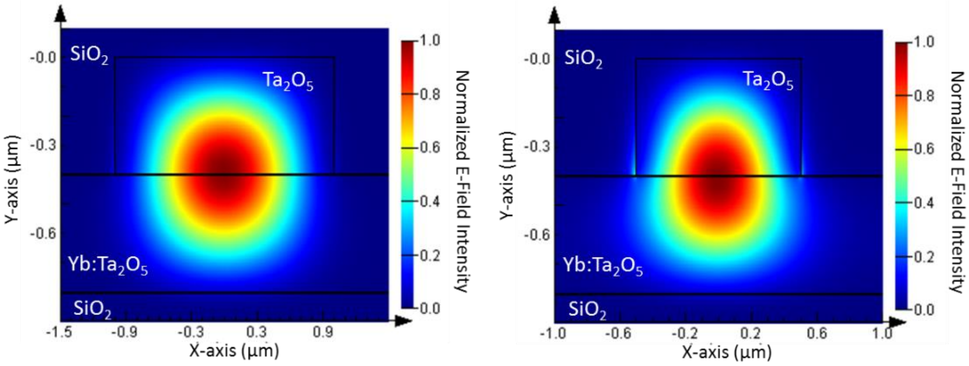

(a) 2 µm strip width (b) 1 µm strip width

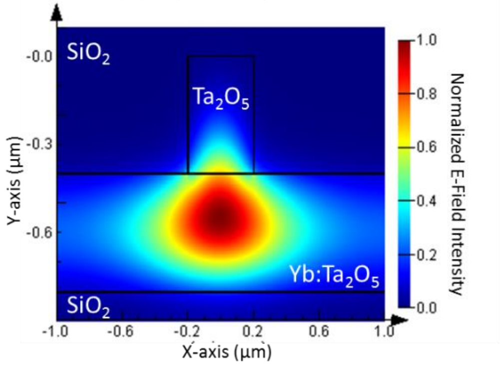

(c) 400 nm strip width

Figure 3.14 Simulated mode profile of strip loaded waveguide with (a) 2 µm nanowire ($n_{eff} = 2.012$), (b) 1 µm nanowire ($n_{eff} = 1.981$) and (c) 400 nm nanowire ($n_{eff} = 1.914$).

Figure 3.15 shows the effective refractive index of different propagation modes as a function of the nanowire width.

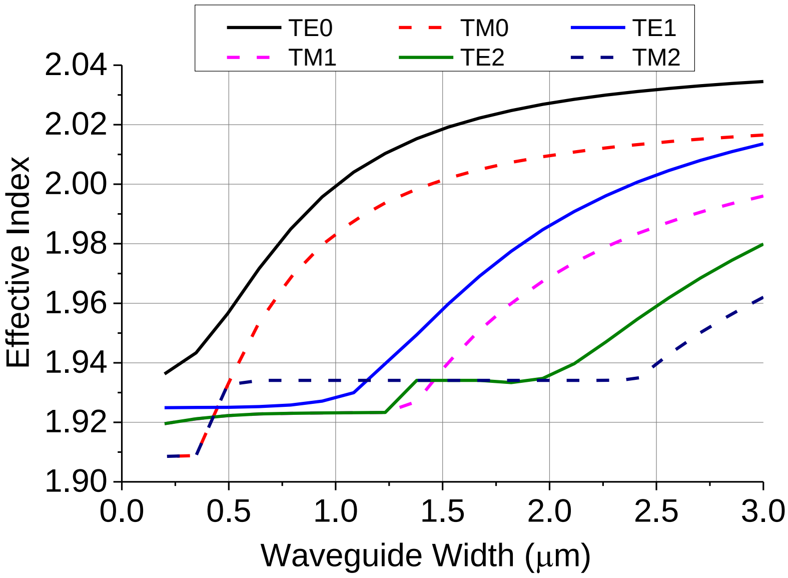

Figure 3.15 Effective index of different modes as a function of nanowire width for strip loaded waveguide

As expected, the effective index reduces as the nanowire width decreases. However, due to the limitation of the software, the simulation cannot be set to only pick up the modes under the strip.

Therefore, the cut-off nanowire width for higher modes (i.e. non-fundamental modes) can only be figured out by checking the simulated mode profiles, which is 500 nm.

Figure 3.16 shows the full width half maximum (FWHM) of the simulated waveguide fundamental mode in both horizontal and vertical directions. The minimum mode size occurs at 0.7 µm nanowire width. However, due to part of the mode overlapping with the un-doped strip, the fraction of mode that travels in doped area is lower than the waveguide which has narrower nanowire.

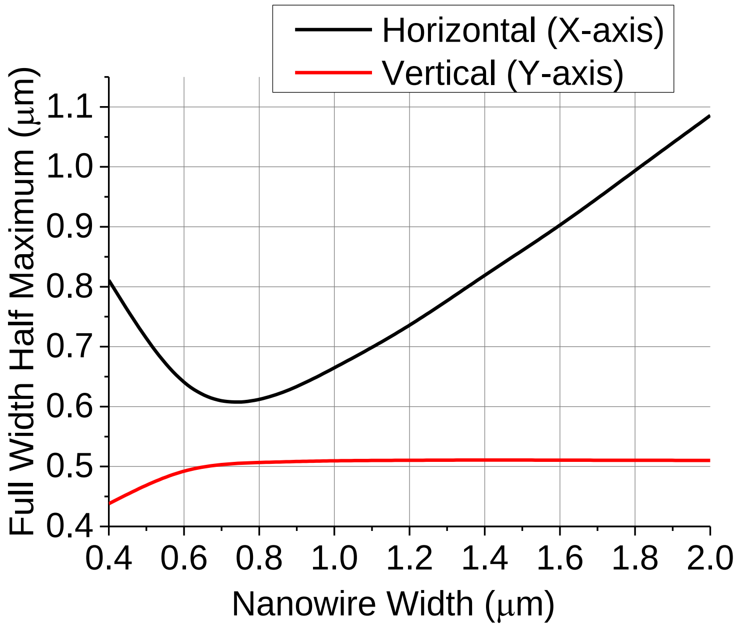

Figure 3.16 Full width half maximum of simulated fundamental mode in strip loaded waveguide as a function of nanowire width

Figure 3.17 illustrates the mode confinement the strip loaded waveguide as a function of nanowire width, which is calculated by integrating the amount of the mode that overlays with the waveguide. The fractions of power confined in the undoped strip (Ta_2O_5) and doped layer ($Yb:Ta_2O_5$) are plotted individually. It is clear to see that with the decreasing of nanowire width, the amount of power that travels in the doped layer increases. Hence, for the same amount of pump power, the waveguide with narrower nanowire will have more power contributes to the laser excitation.

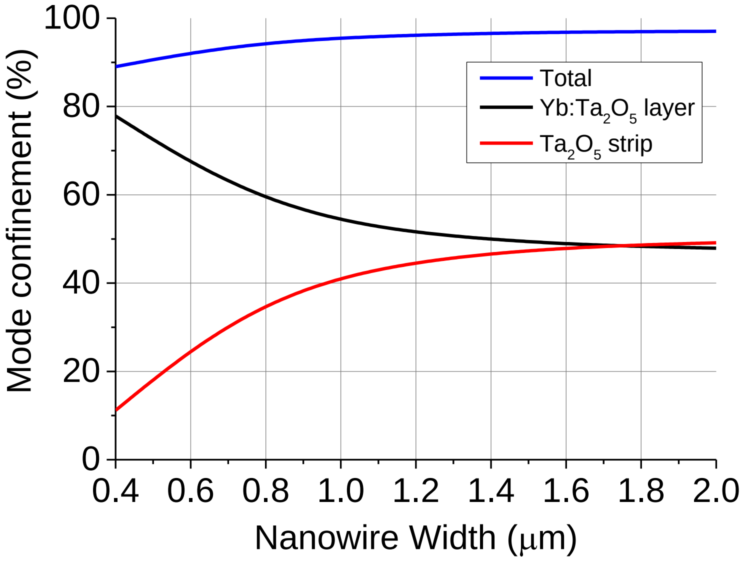

Figure 3.17 Confinement of the mode inside the strip loaded waveguide as the function of nanowire width

3.4.1.2.2 **SiO_2 Based Buried Channel Waveguide**

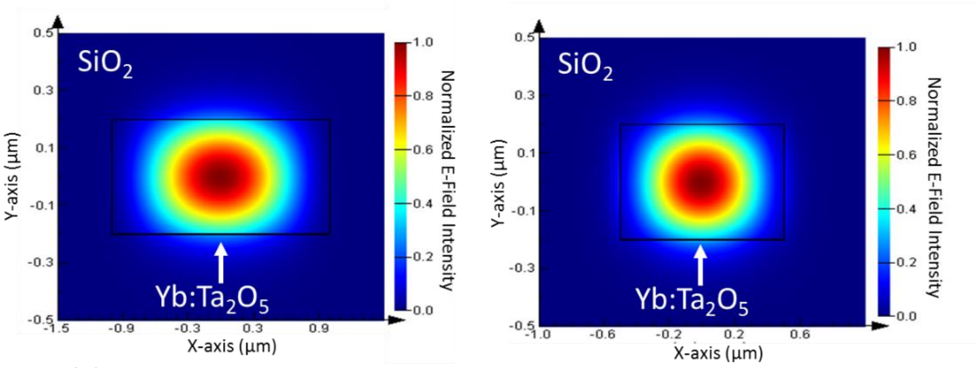

(a) 2 µm nanowire width (b) 1 µm nanowire width

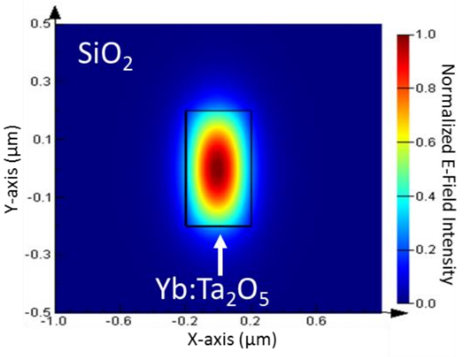

(c) 400 nm nanowire width

Figure 3.18 Simulated mode profile of SiO_2 buried channel waveguide with (a) 2 µm nanowire ($n_{eff} = 1.909$), (b) 1 µm nanowire ($n_{eff} = 1.866$) and (c) 400 nm nanowire ($n_{eff} = 1.668$).

Figure 3.18 (a), (b) and (c) shows the simulated mode profile of the channel waveguide buried in SiO_2 cladding with 2μm, 1 μm and 400 nm nanowire, respectively. The simulation results show that even with the narrowest nanowire (400 nm), the light at 1100 nm can still propagate inside the nanowire without spreading to the cladding layer. The modal overlap with the sidewall in this waveguide shows the same performance as it of the strip loaded waveguide – the narrower the waveguide is, the more the mode overlaps with the waveguide sidewall. Therefore, propagation loss of narrow waveguide is expected to be higher than the wide waveguide.

Figure 3.19 illustrates the effective index curves for different modes propagating inside the nanowire at different nanowire width. The curves show the same tendency as them of the strip loaded waveguide. Different from the strip loaded waveguide, the buried channel waveguide does not have a slab section that any mode that propagates outside the core range is a leaky mode. Thus, the cut-off nanowire width can be concluded from *Figure 3.19* by checking at what width the effective index drops to the refractive index of the cladding. In this simulation, the cut-off width is found to be 600 nm.

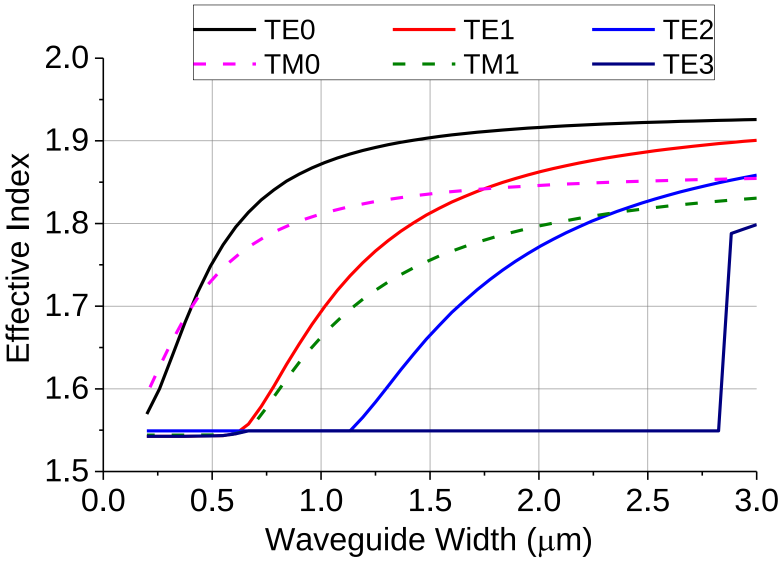

Figure 3.19 Effective index of different modes as a function of nanowire width for SiO_2 based buried channel waveguide

The FWHM of the mode spot of SiO_2 based buried channel waveguide is displayed in *Figure 3.20*. The mode spot size in horizontal direction increases with the increase of the nanowire width while the spot size in vertical direction decreases from 400 nm to 700 nm and keeps constant after that.

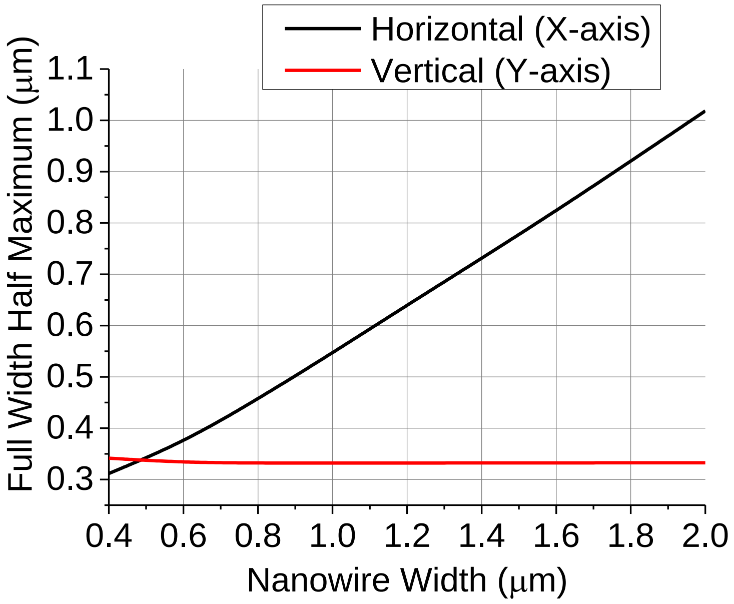

Figure 3.20 Full width half maximum of simulated fundamental mode in SiO_2 based buried channel waveguide as a function of nanowire width

Figure 3.21 illustrates the mode confinement of channel waveguide buried in SiO_2 as a function of nanowire width. As expected, the confinement reduces with the decrease of nanowire width.

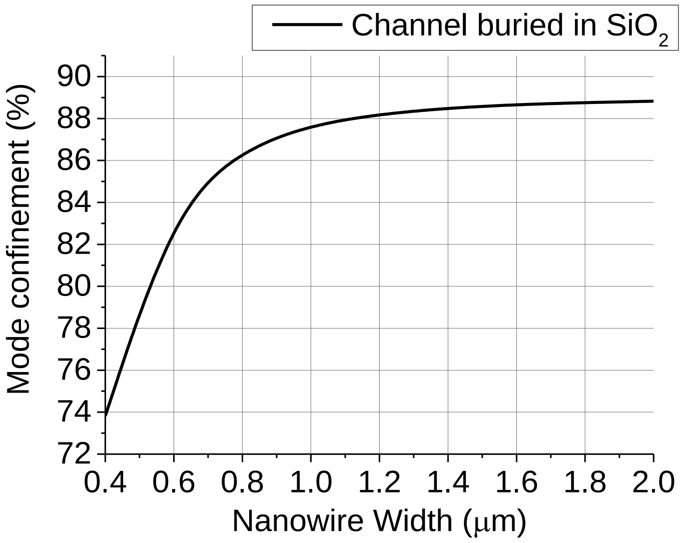

Figure 3.21 Confinement of the mode inside the SiO_2 based buried channel waveguide as the function of nanowire width

3.4.1.2.3 **Polymer Based Buried Channel Waveguide**

Figure 3.22 displays the simulation results for the polymer based buried channel waveguide with different width. Similar to the SiO_2 based buried channel waveguide, the mode is well confined inside the waveguide with nearly the same effective refractive index (difference <0.3%). The simulation also confirms the same expectation as the previous two waveguides – the mode propagates in narrow waveguide will overlap with the sidewall more than it propagates in wide waveguide, thus causing a higher propagation loss in the narrow waveguide.

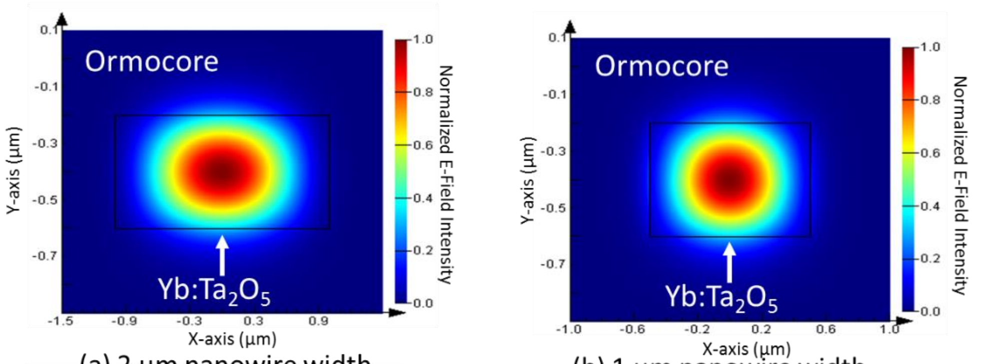

(a) 2 µm nanowire width

(b) 1 µm nanowire width

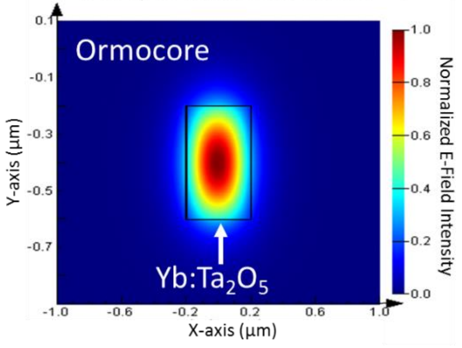

(c) 400 nm nanowire width

Figure 3.22 Simulated mode profile of polymer buried channel waveguide with (a) 2 µm nanowire ($n_{eff} = 1.902$), (b) 1 µm nanowire ($n_{eff} = 1.863$) and (c) 400 nm nanowire ($n_{eff} = 1.596$)

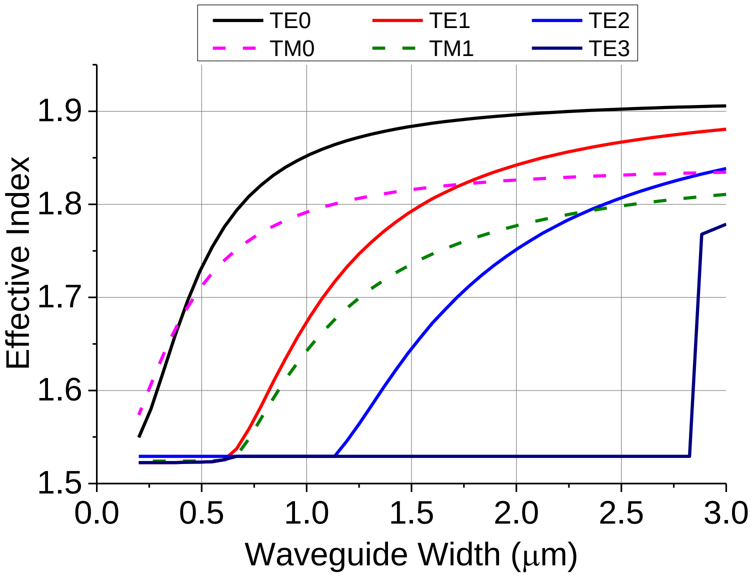

Figure 3.23 Effective index of different modes as a function of nanowire width for polymer based buried channel waveguide

The effective index curves of different modes at different nanowire width for polymer based buried channel waveguide is shown in *Figure 3.23*. The trend of the curves is identical to it of the SiO_2 based buried channel waveguide as shown in *Figure 3.19*. This is expected because of the refractive index of the polymer is very close to the SiO_2. The cut-off width extracted from the figure is 600 nm.

The mode spot size of polymer based buried channel as a function of nanowire width is shown in *Figure 3.24*. The trends of the FWHM in both directions are exactly the same as them of the SiO_2 based buried channel waveguide.

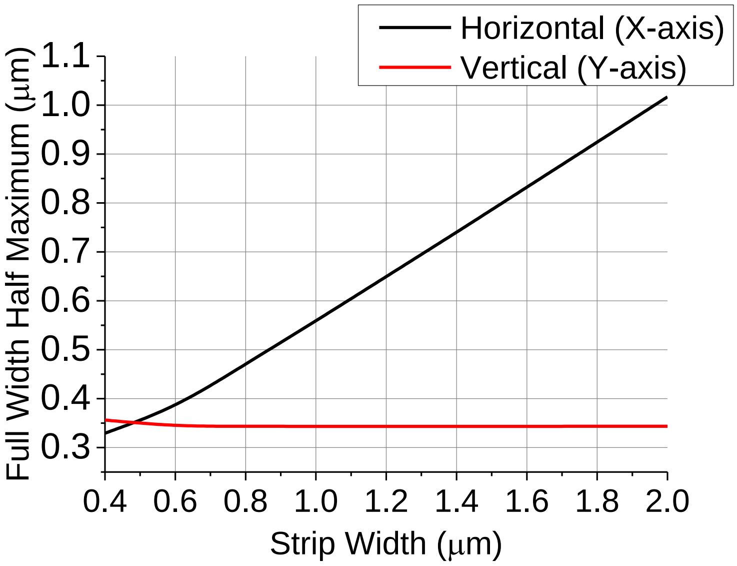

Figure 3.24 Full width half maximum of simulated fundamental mode in polymer based buried channel waveguide

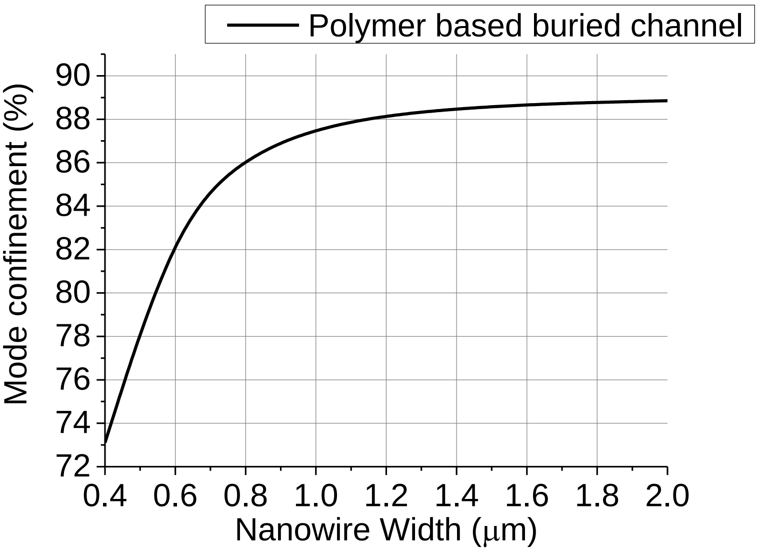

Figure 3.25 Confinement of the mode inside the polymer based buried channel waveguide as the function of nanowire width

Figure 3.25 shows the mode confinement of the polymer based buried channel waveguide. The confinement of polymer based waveguide is nearly identical compared to it of the SiO_2 based waveguide, which corresponds to the negligible difference in effective refractive index.

3.4.1.2.4 **Comparison**

Figure 3.26 illustrates the mode profiles of three different types of waveguide proposed in Section 3.3.2. Compared to the buried channel waveguides, the strip loaded waveguide has a larger mode size. This results in a lower power density compared to that for the same width buried channel waveguide and consequently increases the pumping power needed for reaching threshold. However, on the other hand, the distance between the mode surface and waveguide in strip loaded waveguide is larger than in the buried channel waveguides, which leads to lower surface scattering loss. Both buried channel waveguides provide good confinement. Compared to the SiO_2 based buried channel waveguide, the fraction of power confined in polymer based waveguide is slightly lower due to the relatively lower refractive index contrast (~0.56) between the core and the polymer.

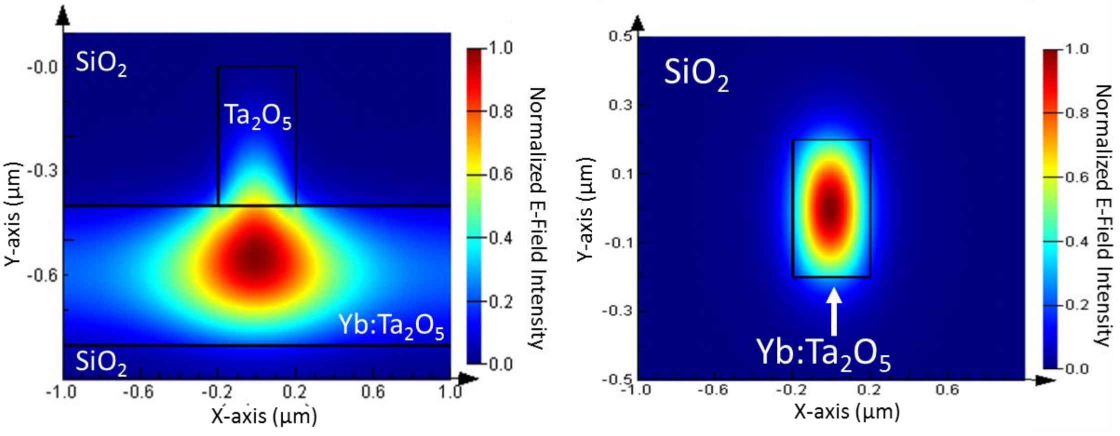

(a) Strip loaded

(b) Channel buried in SiO_2

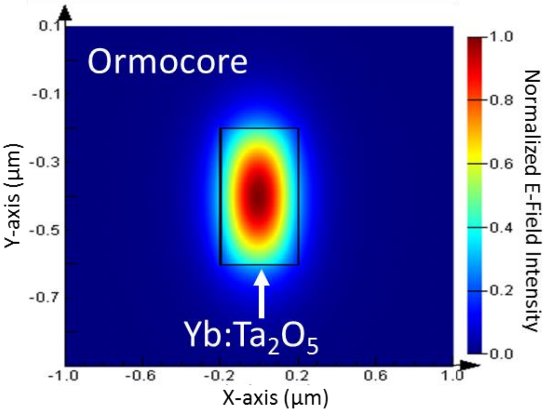

(c) Channel buried in polymer

Figure 3.26 Simulated mode profile for (a) strip loaded waveguide, (b) buried channel waveguide in SiO_2 and (c) buried channel waveguide in polymer with same nanowire width of 400 nm

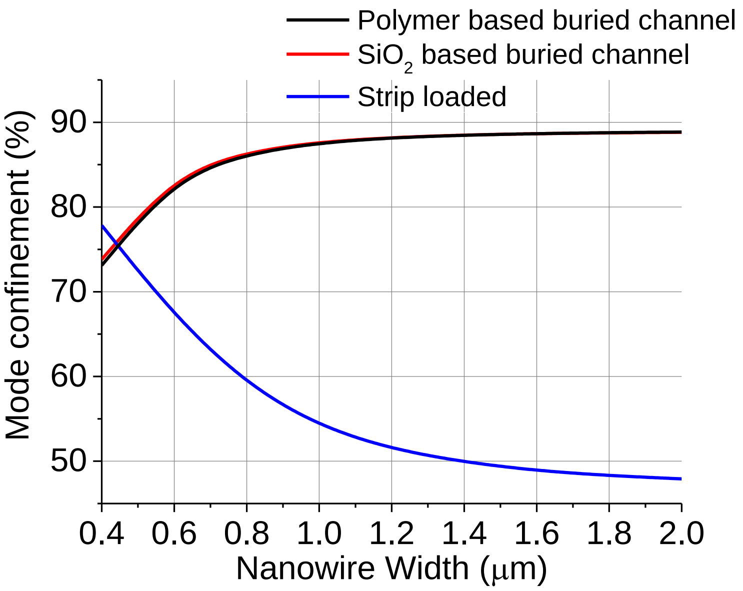

Figure 3.27 Confinement of the mode inside of the doped area of different types of waveguide as a function of nanowire width.

The mode confinement of the doped area of different types of waveguides with respect to the nanowire width are shown in *Figure 3.27*. The curve of both the polymer based and SiO_2 based buried channel waveguide show the same trend that confinement drops with the decreasing of nanowire width. However, the strip loaded waveguide shows the opposite behaviour and has a higher confinement at 400 nm nanowire width. However, as shown in *Figure 3.26*, the strip loaded waveguide clearly has a larger mode spot compared to the other two buried channel waveguide, results in lower power density.

3.4.2 Gain Simulation

Simphosoft is a simulation software that can accurately model light propagation and non-linear effects within photo-activated materials [6]. The software allows full-scale micro-level simulation of photo-active materials by considering a full set of energy levels and transitions of the material. The modelling part of this software is based on the Finite-Difference Time-Domain (FDTD) method. For wave propagation, Simphosoft implements a nonlinear Schrodinger equation derived from a nonlinear Helmholtz equation with a paraxial approximation. For the full simulation with photo-active materials, this software couples rate equations of given material parameter with propagation equations.

3.4.2.1 Energy Diagram and Transitions Building

To simplify the simulation, rather than a full model with all the transitions in it, a model only containing the most important transitions was built.

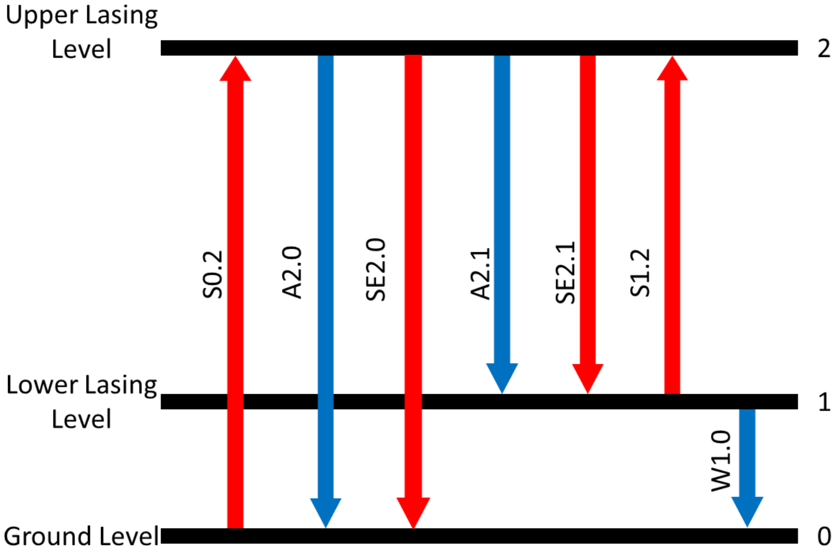

Figure 3.28 Yb^{3+} energy diagram and transitions

Figure 3.28 shows the simplified model that was built. In this model, most of the non-dominant transitions have been removed. The neglected transition are: the absorption from ground level 0 to upper laser level 2 (S0.2); the spontaneous emissions from upper laser level 2 to ground level 0 (A2.1); the stimulated emission from upper laser level 2 to ground level 0 (SE2.0); the spontaneous emissions from upper laser level 2 to lower laser level 1 (A2.1); the stimulated emission from upper laser level 2 to lower laser level 1 (SE2.1); the absorption from lower laser level 1 to upper laser level 2 (S1.2); the non-radiatively decay from lower laser level 1 to ground level 0 (W1.0).

Table 3.1 Parameters used for setting up the transitions in the simulation

Transition	***Parameter***	***Parameter Origin***
S0.2	Absorption cross section = $2.80 \times 10^{-20} cm^2$	[4]
SE2.0	Emission cross section = $2.9\times 10^{-20} cm^2$	[4]
A2.1	Relaxation Time = $260 \mu s$	[4]
A2.0	Relaxation Time = $260 \mu s$	[4]
W1.0	Relaxation Time = $600 ns$	Assumed
SE2.1	Emission cross section = $0.5 \times 10^{-20} cm^2$	[4]
S1.2	Absorption cross section = $0.027 \times 10^{-20} cm^2$	[5]

Table 3.1 gives the parameters that have been used to set up the simulation. The values of absorption and emission cross section for pump wavelength are taken from the measurement and estimation in Section 3.1.2. The radiative relaxation time is set to 260 µs as reported by A. Aghajani in his paper[4]. The phonon induced non-radiative relaxation time has been assumed to be 600 ns as this type of transition is usually very fast [5]. The absorption and emission cross section at lasing wavelength are set to the value that A. Aghajani reported [4] and J. Kong reported [7].

In the transitions building, the thermal induced populates and depopulates of the lower laser level (Level 1) and any intraband transitions were considered due to the limitation of the Simphosoft software.

3.4.2.2 **Laser Source and Sample Set-up**

After configuring the energy diagram and the transitions, the experiment set-up including laser source and sample parameter settings needs to be done. *Figure 3.29* shows the simulation set-up for a pump-probe experiment.

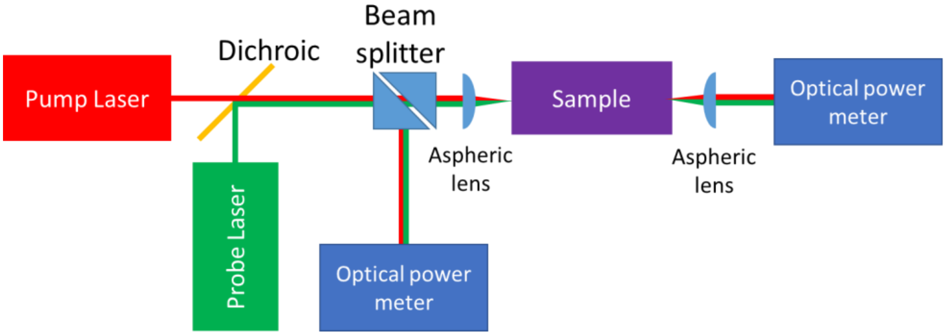

Figure 3.29 Schematic of pump-probe experiment simulation

In this simulation, two laser sources have been defined: a 975 nm wavelength pump laser and a probe laser at 1030 nm wavelength. Due to the limitation of the software, the only available pump source is the pulsed laser source (there is no option for the CW source). Therefore, in order to simulate the pump-probe experiment under continuous wave (CW) pumping, both the pump and probe source were been set to emit a “top hat” shape pulse with a width of 100 µs to mimic the CW pumping for 100 µs (as shown in *Figure 3.30*). A dichroic has been placed in the light path to combine two laser beams into one. The sample has been set to be 1 mm long to speed up the simulation. Due to the simulation software only permits rod-like sample, the waveguide has been set to have a radius of 0.5 µm so that the waveguide has the same area compared to the rectangular waveguide with the dimension of 0.4 x 2 µm.

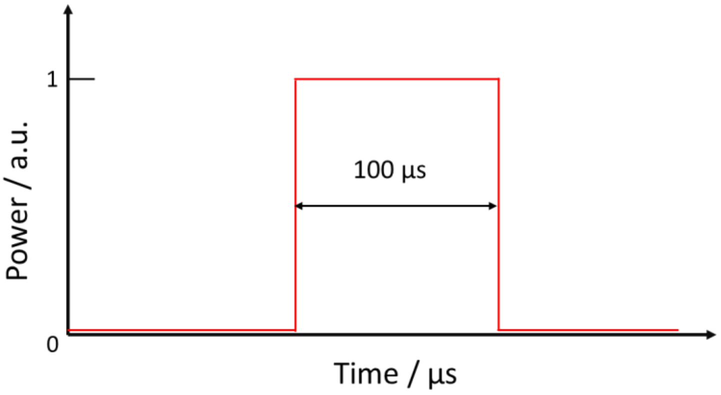

Figure 3.30 Temporal pulse shape and time scale of both pump and probe source

Table 3.2 gives the parameters of the pump and probe sources and the dimension and doping concentration of the sample.

Table 3.2 Parameters of components in the pump-probe experiment simulation

Component Name	***Parameters***
Pump Source	$\lambda = 975nm, E = 0.5\mu J(P = 50\ mW), t = 100\mu s, R = 0.5\mu m$
Probe Source	$\lambda = 1030nm, E = 0.1\mu J(P = 1\ mW), t = 100\mu s, R = 0.5\mu m$
Sample	$L = 1mm, R = 0.5\mu m, \rho = 6.2 \times 10^{20} cm^{-3} (equivlent\ to\ 1.5\ at.\%)$

E: energy of pulse; P: average power of pulse; t: time of the pulse; R: radius; L: length; ρ: doping concentration.

Due to the limitation of the software, the sidewall roughness cannot be implemented. Therefore, there is no sidewall scattering loss has been taken into consideration. The Fresnel reflection at the sample interface was also not included as the pump and signal source power that have been set are the power at the beginning of the sample.

3.4.2.3 **Simulation Results**

As mentioned in previous sections, the simulation software has some limitations. Therefore, this modelling approach is a preliminary simulation which is not taken any sample sidewall roughness and thermal dynamics into consideration (i.e. perfect condition).

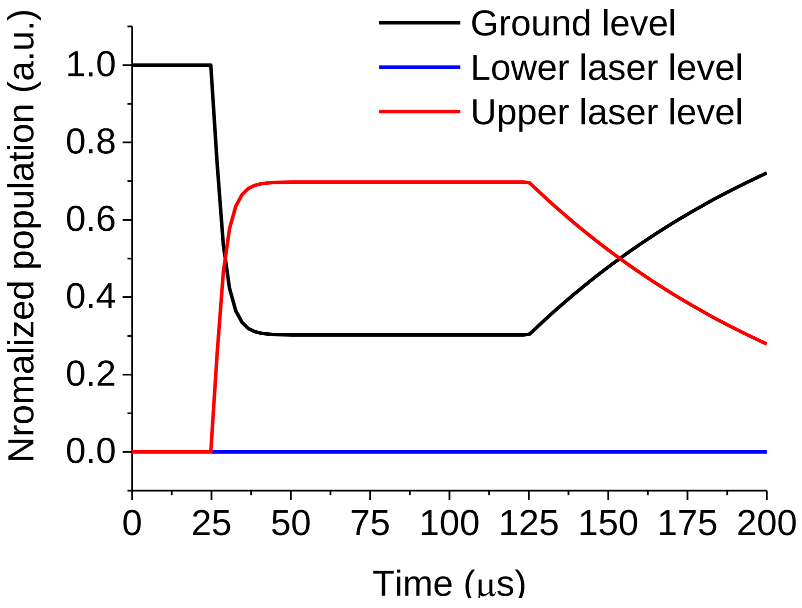

Figure 3.31 Changes of population for different energy levels over time

Figure 3.31 gives the change of population density of different energy levels over time. The sample started to be pumped by both the pump laser and probe laser at the time of 25 μs in the simulation (as shown in *Figure 3.31*). The ions in the ground level started being excited to the upper laser level

2. Population inversion was achieved after 5 µs of pumping. The population densities of each level reached a state of equilibrium in 5 µs after population inversion and kept steady until pumping finished at 125 µs.

Figure 3.32 shows the intensity of the probe light measured in different positions of the 1 cm long, 2000 nm wide nanowire (400 nm thick). The intensity of the probe was measured every 1 mm from the beginning of the sample. It is clear that there is increasingly higher intensity over the length of the sample, which means there is an amplification of the probe light when it passes through.

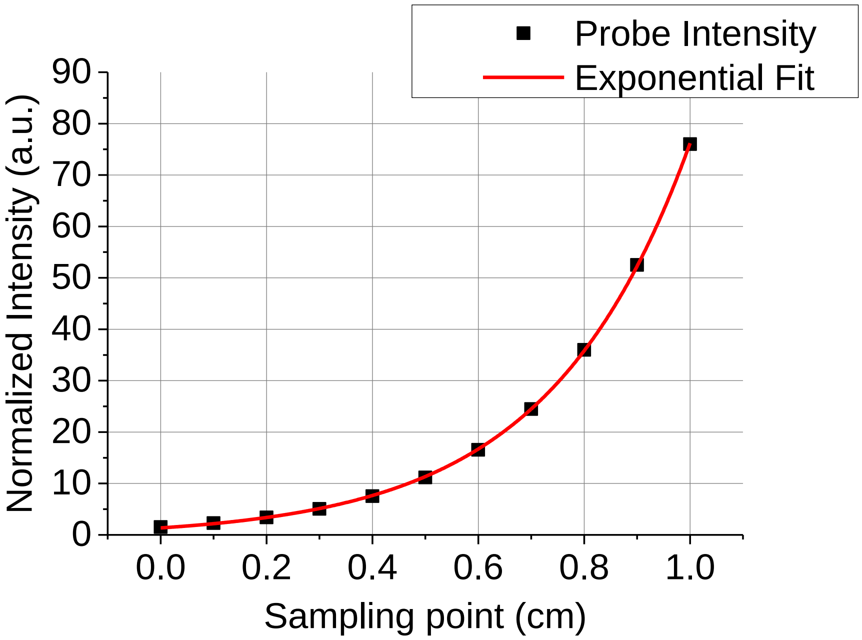

Figure 3.32 Intensity measured at different positions of the sample under 100 mW pumping

The gain for a single trip within the gain medium of length l is given by:

$$G_{single} = \exp(gl)\exp(-\alpha l) \qquad Eq.2-16$$

where g is the gain coefficient of the material taking all absorption and emission caused by optical transitions into consideration and α is the loss coefficient inside the cavity related to internal cavity loss, and l is the length of the medium. Thus, the intensity of the light measured at the end and inside of the medium can be written as:

$$I = I_0 \times G_{single} = I_0 \times \exp(gl - \alpha l) = I_0 \times \exp(g_{net} l) \qquad Eq.3-9$$

where I_0 is the input light intensity at the beginning of the laser medium and g_{net} is the net gain coefficienct which equals to the sum of g and $-\alpha$.

Figure 3.9 displays the intensity of probe light measured from different positions of the sample. All the points are perfectly fitted with the curve:

$$y = 1.561 \times \exp(3.9125x) \qquad Eq.3-10$$

where y is the probe intensity and x is the length. By matching the Eq.3-9 and Eq.3-10, we could know that the incident beam intensity is $I_0 = 1.561$ and the gain coefficient $g_{net} = 3.9125$ in the unit of cm^{-1}. This justifies the probe intensity increasing exponentially with increasing distance.

The amplification coefficient can be defined as the ratio of the input optical intensity to output optical intensity:

$$C_{amp} = \frac{I(Output)}{I(Input)} \qquad Eq.3-11$$

where $I(Input)$ and $I(Output)$ is the intensity of the signal beam measured at the beginning and the end of the sample, respectively.

Hence the total gain in dB of the sample can be expressed as:

$$G(total) = 10 \times \log(C_{amp}) = 1.5579\ dB \qquad Eq.3-12$$

Because of the sample length of 1 mm, the gain in dB per unit length under 10 mW pump is:

$$G(dB) = \frac{G(total)}{L} = 1.5579\ dB/mm \qquad Eq.3-13$$

3.4.2.4 Gain – Power Scanning

After finishing the initial simulation, more simulations with different pump power were done to produce a gain – power curve.

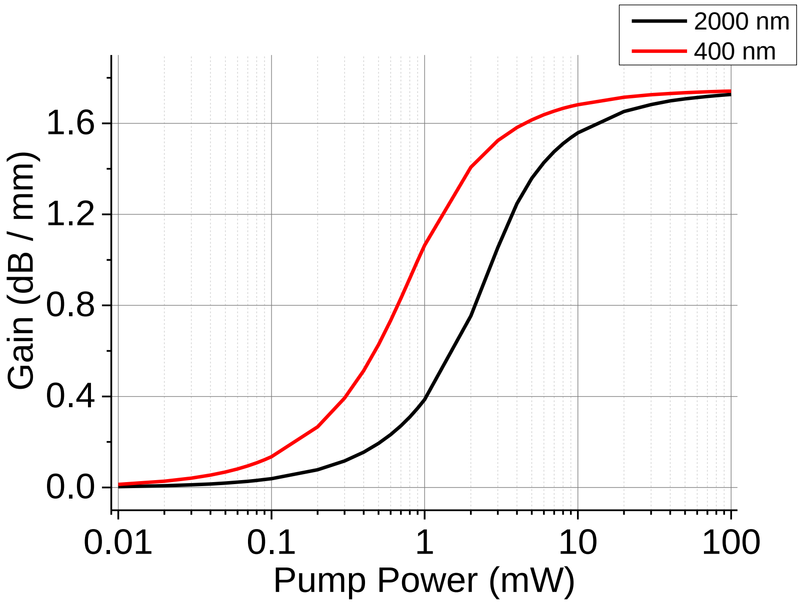

Figure 3.33 Waveguide gain versus Pump power for 2 µm and 400 nm wide nanowires

Figure 3.33 shows the gain versus pump power curve for the widest (2 µm) and narrowest (400 nm) nanowires in the design. Both two curves show that the gain of the nanowire increases with the increasing pump power and saturates when the pump power reaches a certain value. With the same pump level, the narrower nanowire provides higher gain due to the higher pump power density inside the waveguide.

The saturation of the gain is due to there being no more states that can be promoted to the upper laser level. Any further increase of the pump power will not provide any increasing in amplification of the probe light. The saturated gain extracted from the simulation is 17.2 dB/cm.

3.5 Summary

In this chapter, the loss mechanisms of the waveguide, including coupling loss and waveguide loss, are discussed. The only loss mechanisms that is mainly affected by the waveguide geometry is the mode mismatching. Therefore, a low loss waveguide design, containing nanowire, taper and coupler section, is developed to minimize the mode mismatching. By introducing the wide coupler section, the mode mismatch at air-waveguide interface can be reduced. The mode mismatch between the nanowire and coupler is also minimized by the taper.

Three different types of waveguide with different characteristics are proposed. Strip loaded waveguide provides ease of fabrication and low surface scattering loss due to it has less contact surface with the propagating mode when strip is very narrow, at the cost of having lower power density inside it. SiO_2 buried channel waveguide possesses high power density but suffers from higher surface scattering loss when the nanowire width decreases. Polymer buried channel waveguide has the same structure as SiO_2 buried channel waveguide and similar performance. The main advantage of it over the SiO_2 buried channel waveguide and strip loaded waveguide is its simpler fabrication process that has the capability of low-cost mass production.

Mode simulations were sequentially performed according to the geometries of the three different types of waveguide using Lumerical MODE solutions. All three types of waveguide present good confinement of the propagating mode even at the narrowest nanowire width. The spot size of strip loaded waveguide decreases with the decrease of the nanowire width down to 0.7 µm and starts to increase again. This is due to the mode being more likely to propagate in the planar layer where there is lack of horizontal confinement. Different from the strip loaded waveguide, the mode spot size of the two buried channel waveguide decreases with the narrowing of nanowire. The power confined in the doped area for all three waveguides was calculated. The mode confinement of both the polymer based and SiO_2 based buried channel waveguide drops with the decreasing of nanowire width and at 400 nm width was at 73% and 74%, respectively. The strip loaded waveguide, however, shows the opposite behaviour and has its peak confinement of 77% at 0.4 µm nanowire width.

Gain simulation of an Yb doped nanowire under ideal scenario (i.e. no surface scattering loss or other ion-ion interactions) was carried out by Simphosoft which has both rate equation modelling and FDTD modelling embedded in. The simulation results show that the maximum gain of the Yb:Ta_2O_5 nanowire at Yb concentration of 1.5 at.% is 17.41 dB/cm under 100 mW pumping.

Bibliography

[1] R. G. Hunsperger, Integrated Optics: Theory and Technology, Springer (2009)

[2] H. Kogelnik *et al.*, "*Laser beams and resonators*", Appl. Opt. **5** (10), 1550 (1966)

[3] M. F. A. Muttalib *et al.*, "*Tapered nanowire waveguide layout for rapid optical loss measurement by 'cut-back' technique*", Proc. SPIE **8604**, Nonlinear Frequency Generation and Conversion: Materials, Devices, and Applications XII, 86040Z (2013)

[4] A. Aghajani *et al.*, "*Waveguide lasers in ytterbium-doped tantalum pentoxide on silicon*", Opt. Lett. **40**, 2549-2552 (2015)

[5] C. B. Layne *et al.*, "*Multiyhonon relaxation of rare-earth ions in oxide glasses*", Physical Review B, **16**, 1, 10-21 (1976)

[6] Simphosoft Official Website http://www.simphotek.net/simphosoft.html

[7] J. Kong *et al.*, "*9.2-W diode–end–pumped Yb:Y_2O_3 ceramic laser*", Applied Physics Letters **86**, 161116 (2005)

[8] W. K. Burns *et al.*, "*Optical waveguide parabolic coupling horns*", Appl. Phys. Lett. **30**, 28 (1977)

[9] A. F. Milton *et al.*, "*Mode Coupling in Optical Waveguide Horns*", IEEE Journal Of Quantum Electronics, Vol. **QE-13**, NO. 10, (1977)

Chapter 4: Device Fabrication

4.1 Introduction

Waveguides made by amorphous materials that are compatible with CMOS processes are strongly favoured for mass production of integrated optical circuit.

In this chapter the fabrication processes for different types of Yb:Ta_2O_5 nanowire waveguide are presented. The strip loaded and buried channel waveguide on silicon are fabricated utilizing CMOS fabrication technologies such as e-beam lithography, sputtering and dry etching. The fabrication process of polymer based buried channel waveguide using nano-imprint is also presented. The first ever anisotropic reactive ion etching process of Yb:Ta_2O_5 has been achieved, resulting in high profile nanowire channel waveguides.

4.2 Fabrication Procedures

4.2.1 **Fabrication of Strip Loaded Nanowire Yb:Ta_2O_5 waveguide on Silicon**

Figure 4.1 shows the flow chart of the fabrication process of the strip loaded waveguide device.

4.2.1.1 **Bottom SiO_2 layer growth (Step A)**

The fabrication starts with the growth of the bottom SiO_2 cladding layer. According to the design, a 2 µm thick SiO_2 layer is fabricated by a wet oxidation method on a standard 100-oritated N-doped (Phosphorus doped) 6-inch wafer.

The oxidation process was carried out using wet oxidation in a furnace (TS6304, Tempress). Due to the maximum temperature limitation of the machine, the oxidation temperature was set to 1000℃. The process time was set to 23 hours to achieve the nominated thickness.

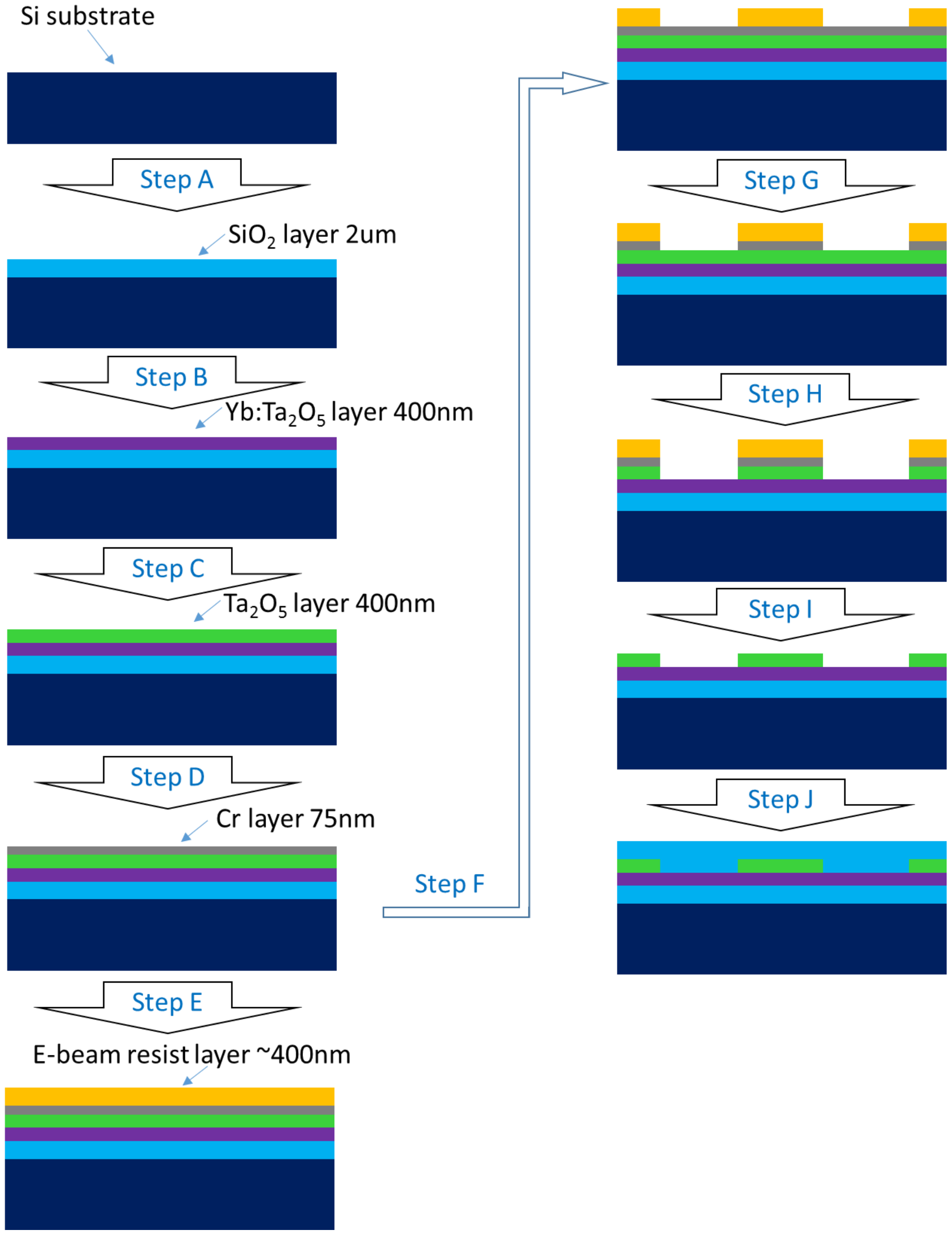

Figure 4.1 Fabrication processes of strip loaded waveguide device

4.2.1.2 **Thin film Deposition (Step B and Step C)**

The next fabrication step is to deposit two thin film layers on the SiO_2 layer - the planar layer ($Yb:Ta_2O_5$) and the strip layer (Ta_2O_5). Prior to the deposition, the sputterer machine was cleaned and conditioned to reduce any possible contamination (for details check Appendix B).

The 400 nm $Yb:Ta_2O_5$ thin film were deposited by plasma assisted reactive magnetron sputtering (PARMS) from a high purity tantalum metal target (99.999%) and a high purity ytterbium metal target (99.999%). This technique offers an improved metal oxide thin films by using dual magnetron sputtering and an additional RF plasma source to create a near-stoichiometric film at low temperature (< 70 °C).

The deposition was performed at a base pressure of 6 × 10^{-7} mbar. The deposition system (Helios ProXL, Leybold Optics) has dual-targets allowing-co-sputtering. Each target is environmentally isolated from the other. Substrates pass each target sequentially allowing different reactive processes to run for each of the two targets simultaneously. Therefore, Yb concentration can be controlled on-site.

Table 4.1 shows the parameter of the Yb:Ta_2O_5. Since the best Yb concentration is unknown, 11 samples with different Yb concentration were produced. As the sputterer is not able to measure the Yb concentration, all the samples were numbered by their Yb deposition powers, which were: 75, 100, 125, 150, 200, 350, 500, 450, 500 and 750W.

Table 4.1 Deposition parameters for Ta, Yb and PBS chamber when depositing Yb:Ta_2O_5 and pure Ta_2O_5

	Ta Chamber	***Yb Chamber***	***PBS Chamber***
RF Power(W)	*8700*	*75 – 750*	*2000*
Gases Flow(sccm)	*Ar / O_2 = 15 / 72.5*	*Ar = 15*	*O_2 = 5*

A 400 nm thick layer of pure Ta_2O_5 was deposited directly on top of the doped Yb:Ta_2O_5 layer using identical process conditions of the Ta chamber. These two layers were deposited sequentially without breaking vacuum, greatly reducing the number of embedded particulates at the interface which would otherwise cause significant scattering loss. The deposition thickness of both films were controlled by optical monitoring system (OMS) that is based on thin film interferences (for details check Appendix C).

4.2.1.3 Mask Deposition and Patterning (Step D - G)

In order to shape the Ta_2O_5 layer into the desired structure, a patterned process needs to be applied. Since Ta_2O_5 is a hard material, the durability of the mask has to be very good. Thus, instead of using normal photoresist, a 75nm Chrome (Cr) layer was used as a hard mask. The deposition was done by evaporation (LAB700, Leybold Optics) under high vacuum (1.5 × 10^7 mbar) with slow deposition rate (0.05nm/s). The layer was chosen to be 75nm thick in order to be able to protect the waveguide during etching the etching process (*Figure 4.1* Step D).

As conventional photolithography is not capable of producing features smaller than 1 µm, E-beam lithography was used to get the best quality pattern and produce 400nm wide features. E-beam lithography is a process that uses a focused electron beam to draw a pattern on a surface covered with an electron sensitive resist. The E-beam machine that was used is called JEOL JBX-9300FS and can provide a maximum resolution of 4nm. A layer of ZEP-520 positive E-beam resist was spun on top of the wafer with 3370 RPM for 90 seconds and was baked for 180 seconds at 180°C (*Figure 4.1* Step E). After being exposed with the electron beam, the sample was then put in a ZED-N50 solution for 90 seconds to remove the unwanted parts. An IPA rinse was subsequently used to clean up the leftover ZED-N50 and any contamination on the wafer (*Figure 4.1* Step F).

To transfer the pattern from the ZEP-520 resist to the Cr hard mask and further to the Ta_2O_5 strip layer, Inductively Coupled Plasma Reactive Ion Etching (RIE-ICP, Plasma Lab System 100 – ICP380, Oxford Instrument) was used. RIE-ICP is a dry etch technique that removes the material deposited on the wafers by using a chemically reactive plasma beam to hit the wafer surface. This type of etching allows for high aspect ratio features since it is highly directional with the etching rate being significantly higher in parallel to the beam direction. The etching recipe for the Cr hard mask is listed in *Table 4.2*.

Table 4.2 RIE-ICP parameters for Cr etching

RF Power (W)	***ICP Power (W)***	***Cl_2 / O_2 (sccm)***	***Chamber Pressure (mT)***	***Temperature (°C)***
10	*750*	*50 / 12.5*	*10*	*20*

4.2.1.4 **Dry Etching of Strip (Step H)**

The pattern of the Cr hard-mask can then be transferred to the Ta_2O_5 layer by once again using the same RIE-ICP tool. The recipe used for etching can be seen in *Table 4.3* which gives the details of the RIE-ICP etching condition for the dry etching step. The etching time was set slightly longer than the calculated time to ensure the Ta_2O_5 is completely etched. Since Yb:Ta_2O_5 is very hard to etch, the over etch of the Yb:Ta_2O_5 layer was avoid.

Table 4.3 RIE-ICP parameters for pure Ta_2O_5 etching

RF Power (W)	***ICP Power (W)***	***C_4F_8 / O_2 (sccm)***	***Chamber Pressure (mT)***	***Temperature (°C)***
200	*750*	*38 / 2*	*10*	*20*

4.2.1.5 **Mask removal and Roughness Smoothening (Step I)**

There were further fabrication steps to be taken before the deposition of the top SiO_2 cladding layer. First of all, the ZEP-520 resist and the Cr hard mask have to be removed. The ZEP-520 resist was stripped by dipping the sample into fuming nitride acid (FNA) for 5 minutes and the Cr hard mask was removed by dipping the sample into a Cr etchant solution for 10 minutes. A quick DI water dump was used after each dipping process to rinse the remaining chemicals.

After the removal of the hard mask and the resist, a 10 minutes KOH dip was applied. The purpose of this process is to remove any possible particles on the wafer surface and to smoothen the roughness of the etched waveguide side walls. The concentration of the KOH solution was 40% (60% water and 40% KOH) and the reaction temperature was 70℃.

4.2.1.6 **Top SiO_2 Layer Deposition (Step J)**

After removing remaining mask and smoothening the waveguide roughness, a 2 µm SiO_2 top cladding was deposited on top of the patterned strip loaded waveguide to provide better optical confinement and to protect the waveguide structure from environmental damage. The SiO_2 top cladding layer deposition was sputtered by the same PARMS system (Helios Pro XL). The deposition was performed under the same base pressure of 6×10^{-7} mbar. *Table 4.4* shows the deposition parameters that used for this deposition.

Table 4.4 Deposition parameters for Si and PBS chamber when depositing top SiO_2 layer

	Si Chamber	*PBS Chamber*
RF Power(W)	*6700*	*2000*
Gases Flow(sccm)	*Ar / O2 = 15 / 40*	*O2 = 25*

4.2.1.7 **Oxygen annealing**

Oxygen annealing can further oxidise the deposited SiO_2 top cladding, Ta_2O_5 waveguides and Yb:Ta_2O_5 layers and improve their performance by activating the Yb dopants and reducing the stress in the thin film. The process was done by heating the sample under an oxygen environment using a contaminate-free tube in the furnace (TS6304, Tempress).

Prior to sample loading, the furnace was pre-heated to 100℃. The loading process takes 1 hour to reduce thermal shock and fracture. Once the sample was loaded, a 4-hour 450℃ annealing in 1:4 oxygen: nitrogen gas flow was applied. For the same reason, the temperature was ramped with a slow temperature gradient (1.95℃/min) for 3 hours. After the annealing stage, the furnace was cooled down to the 100℃ loading temperature over the course of 3 hours with the same temperature step size. The wafer was then unloaded using the same slow process as the load.

The annealing temperature was chosen at 450℃ which is below the Ta_2O_5 crystallization temperature 700℃. This temperature is good for oxidation, but is not able to cause the crystallization of the sample[1]. If the annealing temperature exceeds the crystallization temperature, the Yb:Ta_2O_5 film will start to crystalize.

4.2.1.8 Dicing

After fabrication, the wafer needs to be diced into separate chips for proceeding waveguide experiments. The dicer used is called Loadpoint Microace 3 dicing saw equipped with a hubbed blade that offers a fine cut line of ~50 µm (for details please check Appendix D).

To protect the sample surface, a 50 µm S1813 photoresist layer was spun on top of the wafer and baked at 120°C for 1 minute. The total wafer thickness was estimated to be 755 µm (675 ± 25 µm Si substrate, 5 µm waveguide device including claddings, and 50 µm photoresist) thus to make sure the sample is completely cut, an extra 30µm was added to the cutting depth (i.e. 785µm in total).

4.2.1.9 Polishing

Although the damage of the chip facet was minimized by utilizing the hubbed blade, the end facet of the waveguide was still quite rough and not suitable for any optical pumping and measurement. To smooth the end facets, polishing process was carried out using LP50 Precision Lapping and Polishing System (Logitech).

Polishing process has two steps: physical lapping and chemical polishing. The lapping process is used to flatten the end facet of the waveguide chip. The machine used for lapping is a Logitech LP50. The working principle of this machine is using a flat metal plate together with suspensions containing Al_2O_3 particles of different diameters (i.e. 9 µm, 3 µm and 1 µm) to mill the chip end facet. Usually, the 9 µm Al_2O_3 suspension is applied for rough lapping and the 3µm Al_2O_3 to end the lapping process with a fine finish. As the end facet damage of the waveguide sample was found to be minimal after fine dicing, no rough lapping was taken. Only 1µm Al_2O_3 suspension was used during the whole lapping process to obtain the best quality. The lapping depth was monitored by a micrometer that attached on the sample holder. For both two end facets of the waveguide sample, 200 µm was milled to ensure the remaining sample surface and end facets were scratch and dent free.

Different from physical lapping, chemical polishing uses chemical fluid to smooth the end facet. The machine used for chemical polishing is as the same as used in lapping. However, the plate used in this step was different. In this case a special coated metal plate was used. To chemically polish the sample, a fluid containing alkaline colloidal silica was added during the process. The process time can be neither too short (as the effect of polishing will not be good) nor too long (since it can result in over-milling of the end facet). For the waveguide sample, the optimum polishing time was found to be 15 minutes. The consuming rate of the sample for the chemical polishing process was measured to be 1 µm/min.

4.2.2 Fabrication of Buried Channel Nanowire $Yb:Ta_2O_5$ Waveguide on Silicon

The fabrication process of buried channel nanowire $Yb:Ta_2O_5$ waveguide is as the same as it of the strip loaded nanowire waveguide except for the absence of Ta_2O_5 film deposition and core material etching. The flow chart of the fabrication process of the device is given in *Figure 4.2*.

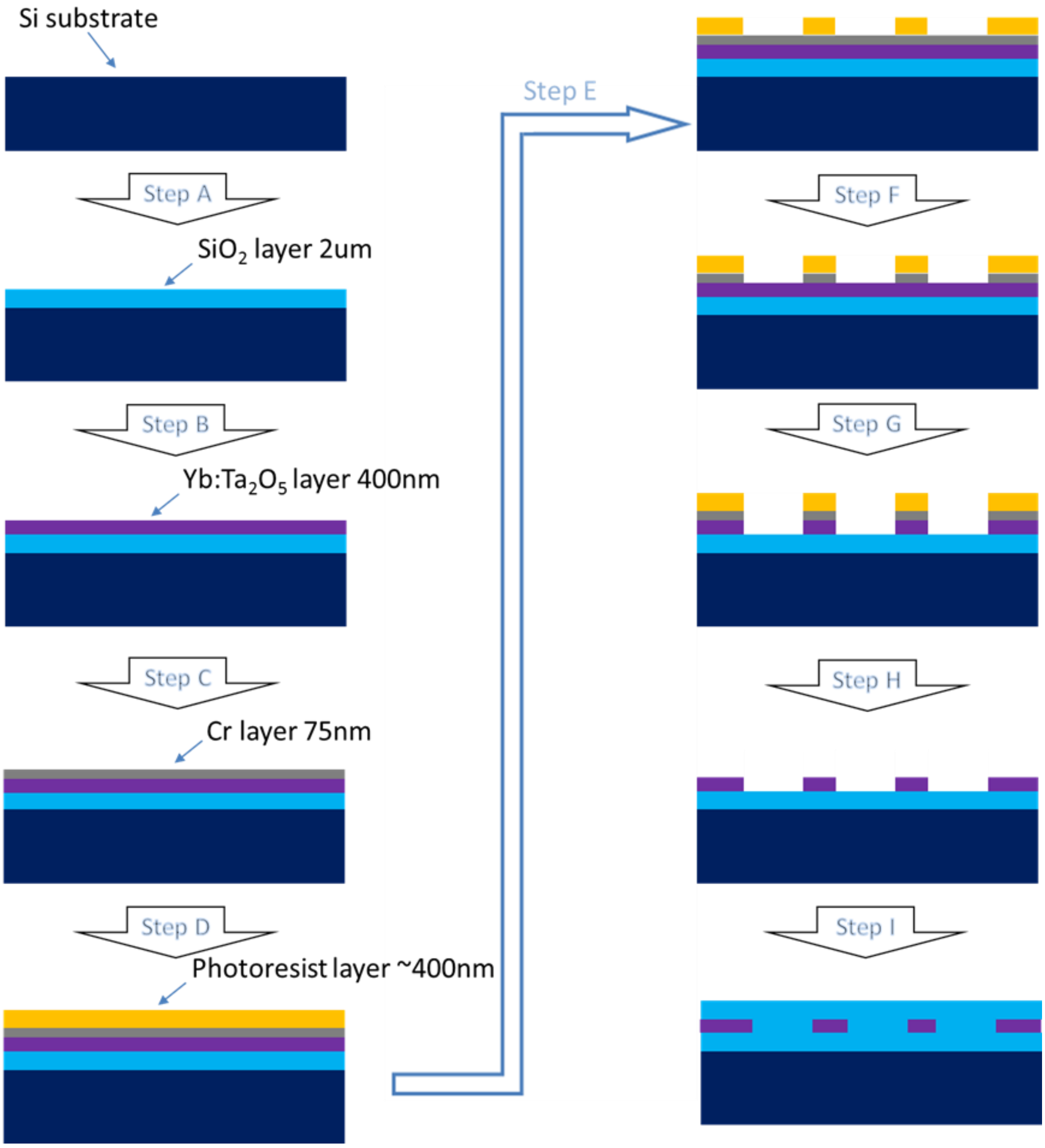

Figure 4.2 Fabrication processes of buried channel waveguide device

The 400 nm $Yb:Ta_2O_5$ core layer was deposited again by PARMS on top of a 2 µm thermally grown SiO_2 on Si. The deposition parameters used was identical to those presented in Section 4.2.1. Following the core layer deposition, Cr hard mask and e-beam resist were sequentially deposited and patterned. Etching of $Yb:Ta_2O_5$ was carried out using RIE-ICP tool with optimized process (parameters are shown in *Table 4.5*) as the original Ta_2O_5 etching process is inefficient in the case of etching Yb:Ta_2O_5.

Table 4.5 RIE-ICP parameters for Yb:Ta_2O_5 etching

RF Power (W)	ICP Power (W)	C_4F_8 / O_2 (sccm)	Chamber Pressure (mT)	Temperature (°C)
200	1250	45 / 5	10	20

The wafer was dipped firstly in 7:1 FNA and Cr etchant to remove the remaining masks and then in 40% KOH to smoothen the etching roughness. After depositing 2 µm SiO_2 top cladding, the wafer was put into the furnace for oxygen annealing. Lastly, dicing and polishing processes were performed to turn the wafer into chips that can be optically measured.

4.2.3 **Fabrication of Polymer Based Buried Channel Nanowire Yb:Ta_2O_5 Waveguide**

The fabrication of polymer based buried channel nanowire waveguide was done in collaboration with VTT Technical Research Centre of Finland as the local imprinting system in University of Southampton is only capable to process 400 nm thick imprinting films. VTT was responsible for creating the polymer bottom cladding and applying polymer top cladding and the rest fabrication process were done locally.

Since Ormocore and Ormoclad are UV cured polymers, either the stamp or the substrate needs to be transparent at UV wavelength range in order to allow solidification of the polymer structure. *Figure 4.3* shows the flow chart of making an imprinting stamp. The Si stamp fabrication (Step A to Step D) was performed locally using standard Si fabrication processes: hard mask deposition, resist spinning, e-beam lithography and dry etching. The etched Si stamp was then sent to VTT for transparent stamp making. There the polymer was applied to the Si stamp (Step E), the transparent substrate was attached and UV cured (Step F) and finally the dismounting of the fabricated transparent stamp from the Si stamp was performed (Step G).

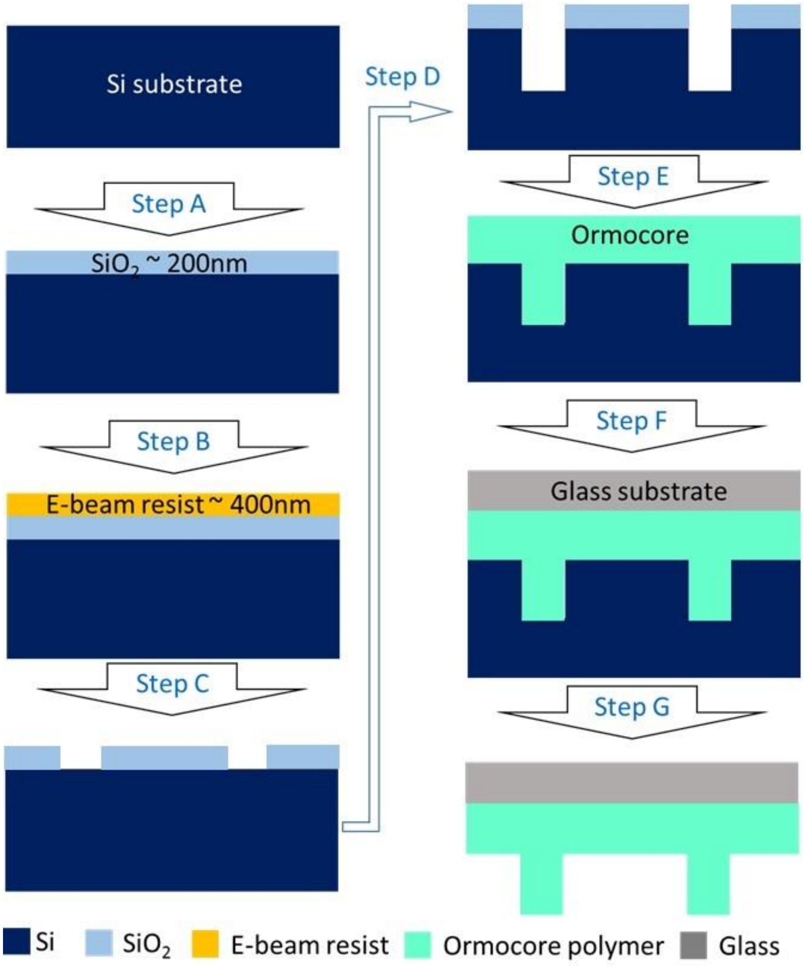

Figure 4.3 Fabrication processes of imprinting stamp

The next step of the fabrication process was to make the actual device as shown in *Figure 4.4*. After Ormocore polymer was spun onto a Si substrate (Step H), the trench was formed by pressing the transparent stamp that was made in previous steps firmly onto the polymer (Step I) followed by UV curing from top surface (Step J). After dismount the stamp, an Yb:Ta_2O_5 thin film was deposited onto the wafer (Step L). Since the deposition is a low temperature process (maximum substrate temperature has been measured to be 75°C), the polymer can maintain its original shape without melting. Ormocore was spun on top of the wafer, working as the top cladding for protection, and forming a symmetric waveguide structure. The wafer was cut into small chips by manual cleaving using diamond scriber. This is because the polymer may peel off from the substrate during polishing, damaging the chip. Consequently, any cutting method (i.e. dicing) which leads to a rough end facet cannot be used.

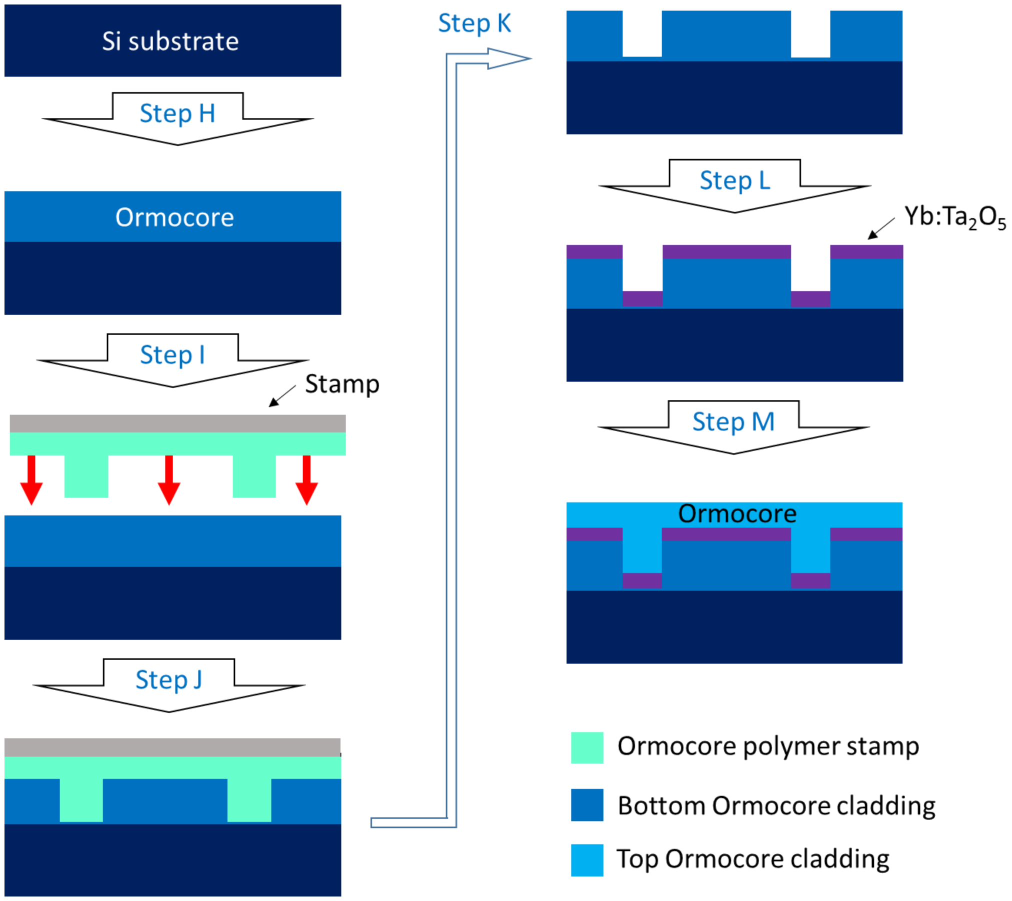

Figure 4.4 Fabrication processes of channel waveguide device on polymer

4.3 Results and Discussion

4.3.1 Strip Loaded Nanowire Waveguide

4.3.1.1 SEM Imaging

The etched waveguide of the strip loaded device was imaged using a scanning electron microscope (SEM) to examine the fabrication outcome. The cross section was prepared by diamond pen cleaving. Since the waveguide was formed by non-conductive materials (except from the Cr hard mask, which is not a part of the designed waveguide), the cross section was coated with a 5nm layer of gold to avoid image distortion that caused by electrostatic charging.

Figure 4.5 provides a cross sectional micrograph of the edge of the strip loaded device after etching. From top to bottom, the layers are the ZEP520 resist, Cr hard mask, Ta_2O_5 strip, Yb:Ta_2O_5 layer and SiO_2 layer. From the picture it is clear that the Ta_2O_5 strip has been successfully patterned. The thickness of Ta_2O_5 and Yb:Ta_2O_5 layer are measured to be 385 ± 10 nm and 386 ± 10 nm, respectively.

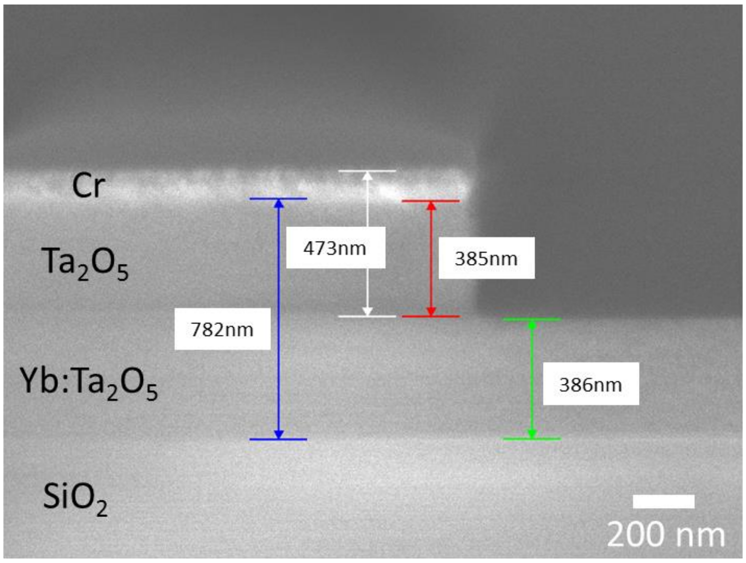

Figure 4.5 SEM micrograph of cleaved cross section of the etched strip loaded device

In *Figure 4.6* , a side wall angle of 87 ± 1° was measured.

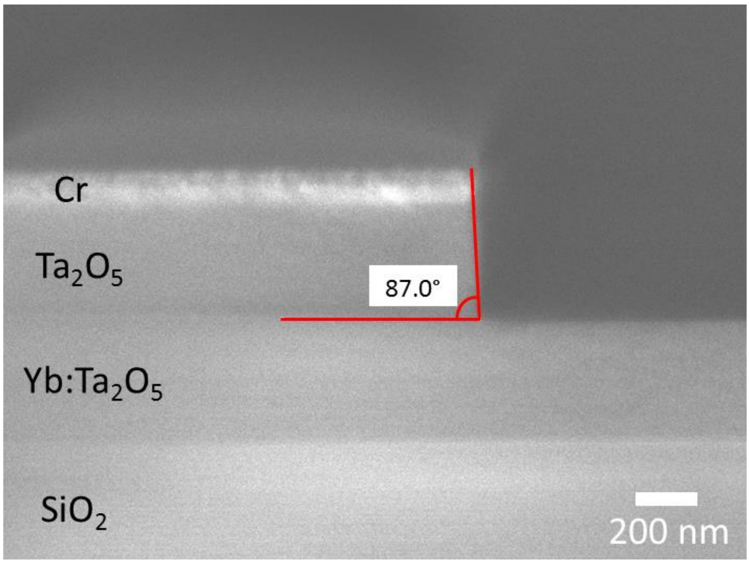

Figure 4.6 SEM micrograph of cleaved cross section of etched Ta_2O_5 strip with measured side wall angle

4.3.2 Buried Channel Nanowire Waveguide

4.3.2.1 $Yb:Ta_2O_5$ Etching Process Optimization

The $Yb:Ta_2O_5$ layer was firstly etched using Ta_2O_5 etching process that stated in Section 4.2.1.4. However, comparing the result with that of the etching result of the pure Ta_2O_5 sample the etching rate was found to be significantly slower. *Table 4.6* shows the comparison of the etching results for both the pure Ta_2O_5 and $Yb:Ta_2O_5$. The etching rate of pure Ta_2O_5 waveguide was 44 nm/min while that of the Yb:Ta_2O_5 was 6 nm/min. As the etching rate of the Cr hard mask is 5.5 nm/min, only 81 nm Yb:Ta_2O_5 can be etched with a 75 nm thick Cr mask.

Table 4.6 Etching results for Ta_2O_5 and Yb:Ta_2O_5 sample using Ta_2O_5 recipe

	Pure Ta2O5	*Yb:Ta2O5*	*Difference compare with pure Ta2O5*
Etch rate of material (nm/min)	*44*	*6*	*~6.3 times lower*
Selectivity (to Cr mask)	*8*	*1.2*	*~6.6 times lower*
Side wall angle	*~90 °*	*Hard to measure*	*N/A*

Figure 4.7 displays the cross section SEM micrograph of the Yb:Ta_2O_5 waveguide after etching using the pure Ta_2O_5 recipe. From the figure, a total etching depth of 16 nm of the Yb:Ta_2O_5 layer has been measured, showing that there the recipe was highly inefficient in the case of the Yb:Ta_2O_5 layer.

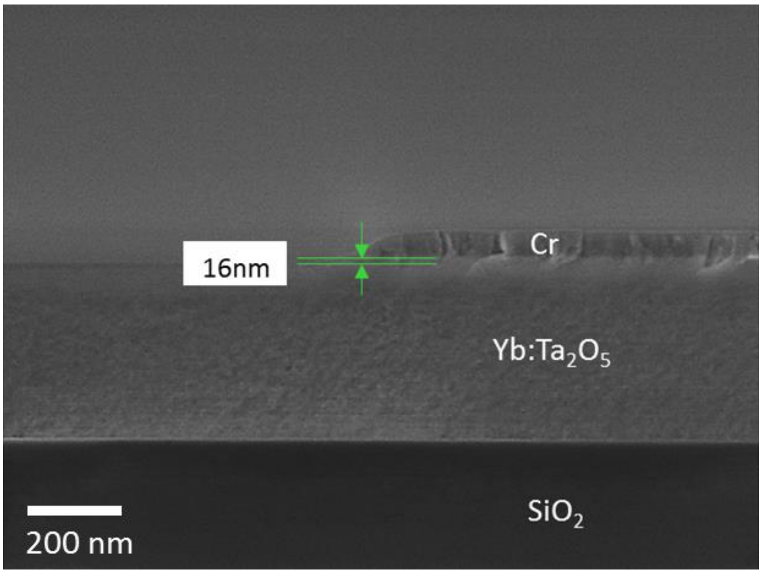

Figure 4.7 SEM micrograph of cleaved cross section of first etching attempt of Yb:Ta_2O_5 after 2.5 minute etching

The possible reason for the failure of the original Ta_2O_5 process is that the Yb dopants in the Ta_2O_5 cannot react with the gases in the conditions set by the recipe. The chemical reaction of the etching process can be written as follows[2]:

$$Ta_2O_5 + C_4F_8 + O_2 \rightarrow TaF_x + COF_x + CO_x \qquad Eq. 4-1$$

In the etching tests, four factors were selected to improve the etching performance: RF power; ICP power; chamber pressure and gas ratio. RF power and chamber pressure are crucial parameters for controlling ion bombardment during the etching process, thus controlling the physical etching of the layer. The ICP power and gas ratio mainly affect the chemical reaction with the target material, thus controlling the chemical etching of the layer [3,4]. Due to the limited number of sample wafers, the etching test was performed using single waveguide chip on a Cr coated carrier wafer to mimic the environment of etching of a whole wafer.

The Yb:Ta_2O_5 etch rate extracted from the first attempt was very slow, implying the chemical etching was not sufficient. Therefore, the first step of recipe development was to improve the effect of chemical etching.

The first step in order to achieve this was to tune the gas ratio between C_4F_8 and O_2. As described in Eq. 4-1, the main etchant for etching Ta_2O_5 is fluorine ions. Hence, increasing the density of the C_4F_8 gas should speed up the etching process. However, with increasing the amount of C_4F_8, the polymer side product that forms also increases and can in turn block the etchant from reacting with the target material. Due to this, O_2 gas was introduced in the etch recipe in order to remove the polymer. Hence, the gas ratio is a critical factor that needs to be considered – too much C_4F_8 will slow down the Yb:Ta_2O_5 etch; too much O_2 will destroy the passivation polymer that is attached on the sidewall and hence reduce anisotropy.

Figure 4.8 shows the results of etching with C_4F_8: O_2 gas ratio of 0.5, 0.7 and 0.9. As expected, with the increase of the fraction of the C_4F_8 gas, the etch rate of Yb:Ta_2O_5 increases. The sidewall angle decreases from 106 degrees to 93 degrees indicating the improvement of sidewall passivation caused by the polymer that is formed. Since the goal of this etching is to achieve a waveguide with a 90 degrees sidewall, the gas ratio of 0.9 was picked for the formal etching recipe.

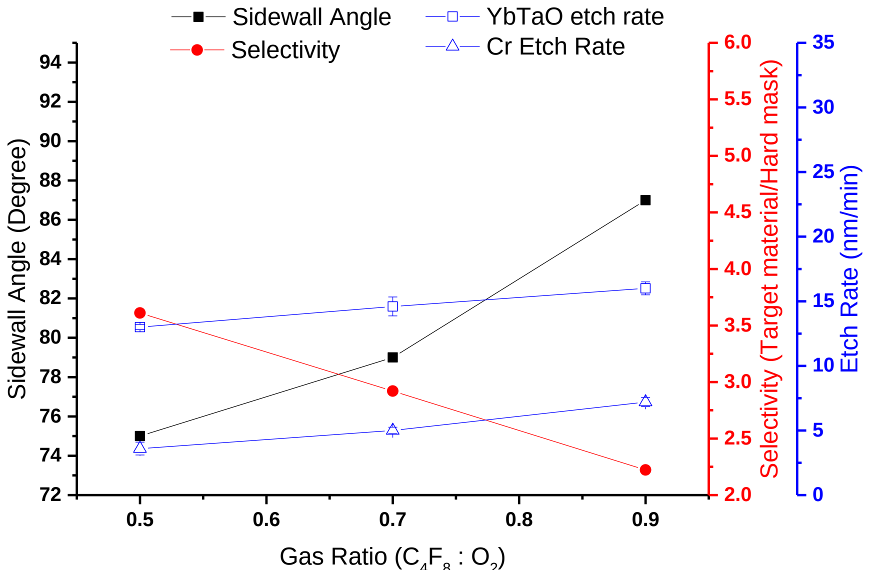

Figure 4.8 Etch rate for Yb:Ta_2O_5 and Cr; sidewall angle and calculated selectivity under different C_4F_8: O_2 gas ratio

The next factor that needed to be modified was ICP power, which affects the ion energy of the plasma. The higher the ion energy is, the higher the etch rate can be. During the test, all factor were kept constant while the ICP power was varied from 750 W to 1500 W with a step of 250 W. The results of the etching test is shown in *Figure 4.9*. Both the Yb:Ta_2O_5 and Cr etch rate increased with increasing ICP power as expected. However, the increase of the etching rates between different materials were not proportional, resulting a peak selectivity of 5.28 occurring when 1250 W ICP power is applied.

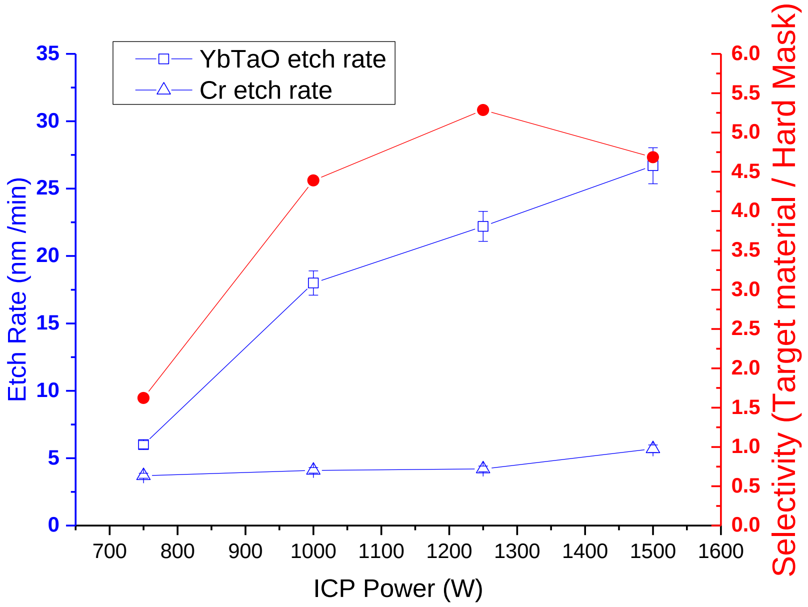

Figure 4.9 Etch rate for Yb:Ta_2O_5 and Cr under different ICP power with calculated selectivity

As mentioned in the previous text, the RF power determines the strength of ion bombardment during the process, which affects the anisotropy of the etching. The stronger the RF power is, the harder the etchant ions will bombard and react with the etch target surface that is perpendicular to the applied bias field, creating an anisotropic etching profile. As for other etching parameters, a suitable RF power has to be chosen. If the RF power is too high, the physical etching process will dominate the etching, resulting in high consumption of the hard mask and eventually lowering the selectivity. The selectivity of the etching process will also be very low if the RF power is too low because of part the etchant will attack the sidewall as well as the bottom surface of the etch target material. *Figure 4.10* illustrates the results of the measured etching rates, sidewall angle and calculated selectivity with 100 W, 200 W and 300 W RF power etching, respectively. The etch rates for both the Yb:Ta_2O_5 target material and the Cr hard mask increases while the RF power is growing. Because the increasing fraction of the etch rates for both materials are not the same, the selectivity that was calculated at different RF powers was different. *Figure 4.10* shows that the selectivity reaches its peak at 200 W RF power, which is 5.3.

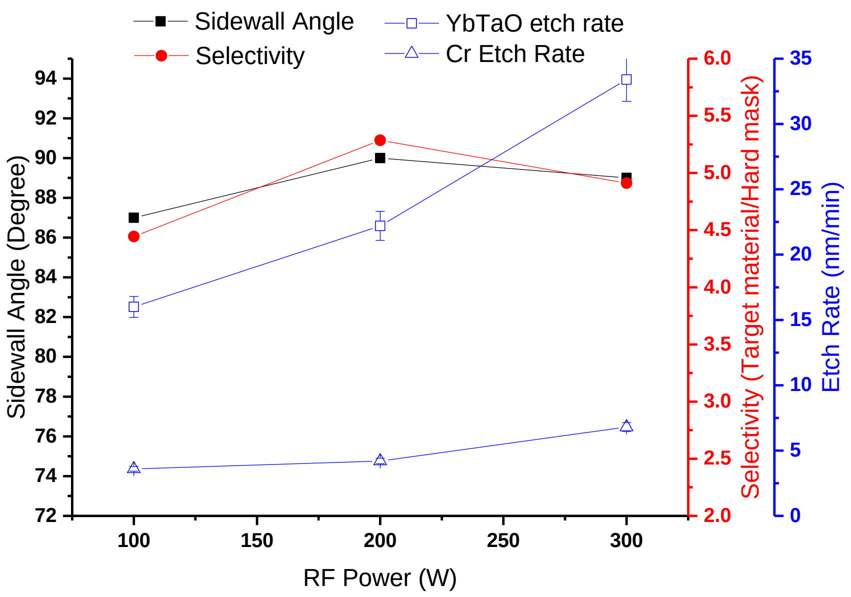

Figure 4.10 Etch rate for Yb:Ta_2O_5 and Cr; calculated selectivity and measured sidewall angle at different RF power

Figure 4.11 provides the etching results of the sample at different chamber pressures. As the pressure increases, the number of gas ions increases simultaneously, creating a denser plasma with lower ion energy. Consequently, the physical etching process (or so-called bombardment-induced physical damage) is reduced, resulting in improved selectivity. Lower ion energy, however, also reduces the efficiency of the chemical etching process, resulting in a lower etch rate. In addition, the increasing number of ions also leads to a higher chance of ions colliding with each other thus changing their kinetic energy and direction before they reach the sample surface. This has the effect of lowering the anisotropy of the etching.

The lowest pressure that a steady plasma can be maintained in the RIE-ICP machine is 5 mT. In this case, the etch rates for both Yb:Ta_2O_5 and Cr reach their maximum value of 27.5 nm/min and 7.2 nm/min, yielding a selectivity of 3.76. The etch rates then drop with the increase of chamber pressure. At 10 mT, the selectivity peaks at 5.3 with the side wall angle of 90°. Both the side wall angle and selectivity decrease with further increase of the pressure. Therefore, the chamber pressure has been set to 10 mT in order to achieve optimum results.

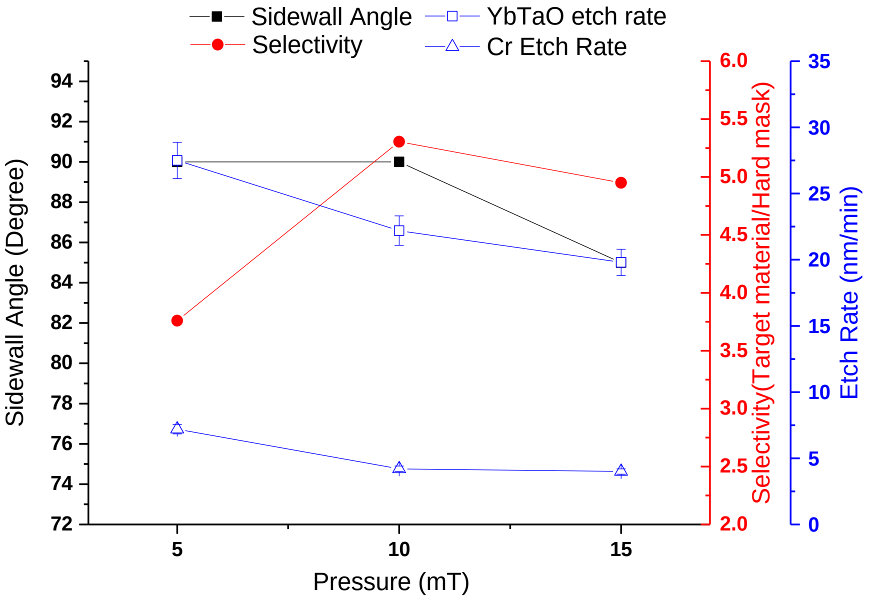

Figure 4.11 Etch rate for Yb:Ta_2O_5 and Cr; calculated selectivity and measured sidewall angle at different chamber pressure

In summary, the optimised etching recipe uses the parameters seen in *Table 4.7*.

Table 4.7 Developed etching recipe for Yb:Ta_2O_5

RF Power (W)	***ICP Power (W)***	***C_4F_8 / O_2 (sccm)***	***Chamber Pressure (mT)***	***Temperature (°C)***	***Yb:Ta_2O_5 etch rate (nm/min)***	***Selectivity (nm/min)***
200	*1250*	*45 / 5*	*10*	*20*	*22.2*	*5.3*

4.3.2.2 **SEM Imaging**

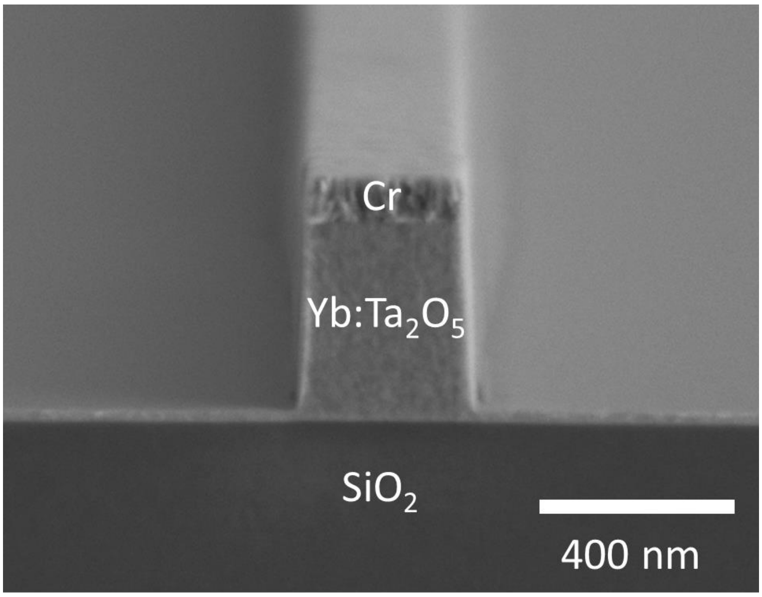

Figure 4.12 SEM micrograph of cleaved cross section of etched Yb:Ta_2O_5 channel waveguide device

Figure 4.12 displays the cross section SEM micrograph of the etched buried channel waveguide device. It shows that an anisotropic etching was achieved. The unwanted Yb:Ta_2O_5 slab was removed completely, leaving a clean channel waveguide structure on the SiO_2 bottom cladding.

Figure 4.13 shows the SEM micrograph of the the etched channel waveguide. A side wall angle of $88 \pm 1°$ is measured from the figure.

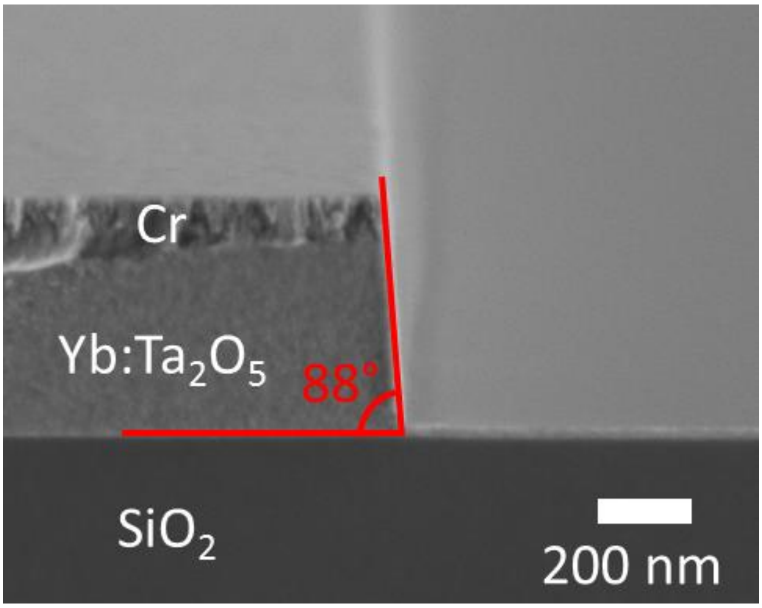

Figure 4.13 SEM micrograph showing side wall angle of etched Yb:Ta_2O_5 channel waveguide device

4.3.3 **Plastic Based Buried Channel Waveguide**

4.3.3.1 **SEM Imaging**

Figure 4.14 shows the SEM micrograph of the fabricated 2.5 µm wide polymer based channel waveguide. It is clear to see that apart from the horizontal surface of the sample, the side wall of the trench is also coated with Yb:Ta_2O_5. The thicknesses of the Yb:Ta_2O_5 waveguide deposited at the bottom of the trench and Yb:Ta_2O_5 layer that deposited on the side wall was measured to be 397 and 238 nm, respectively. This can be minimized by improving the fabrication quality when transferring the stamp pattern so that 90° side wall can be achieved or by changing the stamp design to have undercut side wall structures where the stamp can be released due to the polymer is flexible.

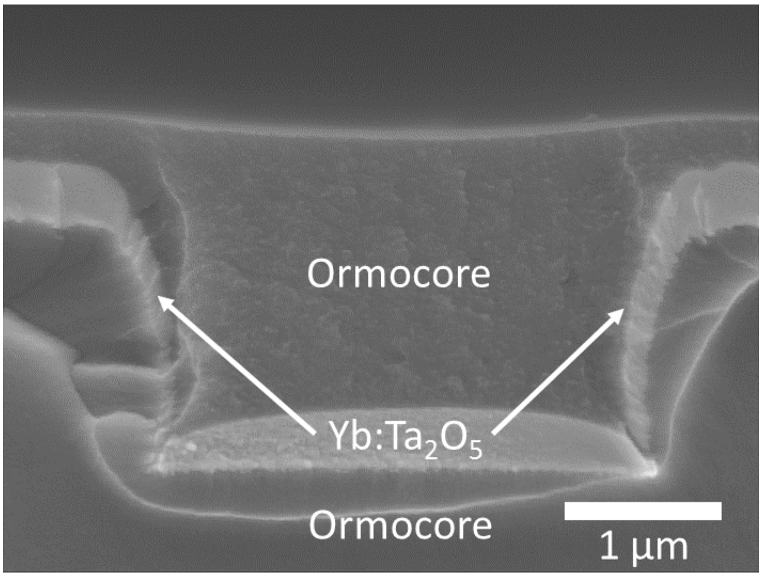

Figure 4.14 SEM micrograph of cleaved cross section of 2.5 µm wide polymer based buried channel waveguide

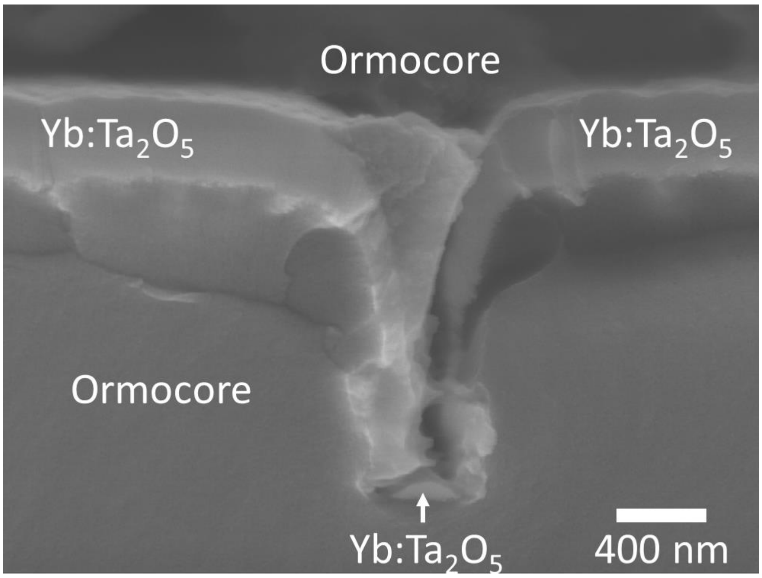

Figure 4.15 SEM micrograph of cleaved cross section of polymer based buried channel waveguide with 400 nm trench

Figure 4.15 displays the SEM micrograph of 400 nm wide polymer based buried channel waveguide. With narrower trench, the curvature of the waveguide top surface increases. The thickness and width of the waveguide were measured to be 108 and 357 nm, respectively. This waveguide is not able to guide light at 1100 nm thus cannot be used for Yb:Ta$_2$O$_5$ laser. The next available waveguide that is capable for guiding light at 1100 nm wavelength is the waveguide made with 600 nm trench, which is shown in *Figure 4.16*. The thickness and width of the waveguide were measured to be 202 and 585 nm.

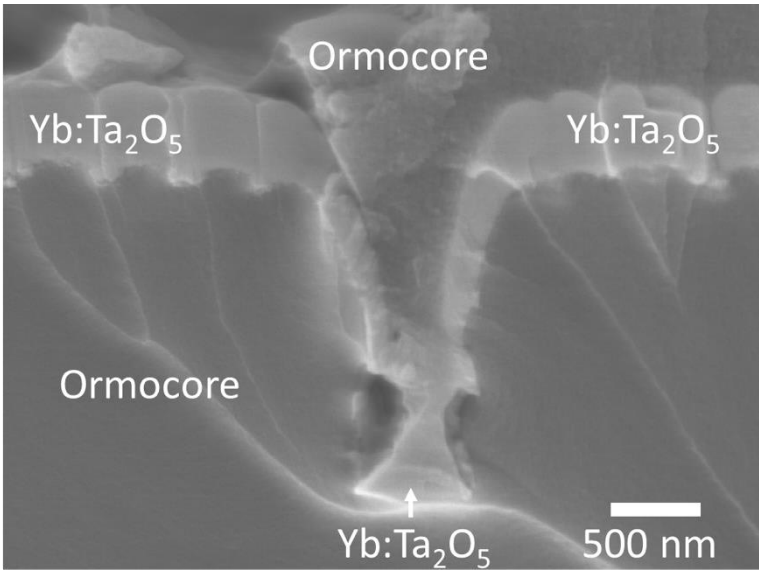

Figure 4.16 SEM micrograph of cleaved cross section of polymer based buried channel waveguide with 600 nm trench

4.4 Summary

The fabrication procedures and the fabricated devices of strip loaded waveguide, SiO_2 based buried channel waveguide and polymer based buried channel waveguide are presented in this chapter.

The strip loaded waveguide was fabricated successfully with CMOS compatible process. The Ta_2O_5 strip and Yb:Ta_2O_5 core layer was measured to be 385 ± 10 nm and 386 ± 10 nm, respectively. The thickness of deposited film is ~3.75% less compared to the designed 400 nm. The side wall angle of the Ta_2O_5 strip was 87 ± 1°.

The buried channel waveguide shares the same fabrication process with the strip loaded waveguide except the material needs to be etched changed to Yb:Ta_2O_5 and no strip is needed. The first anisotropic RIE-ICP etching recipe was developed based on the pure Ta_2O_5 etching process, providing an Yb:Ta_2O_5 etch rate of 22.2 nm/min with ~90° side wall angle. Since the Yb:Ta_2O_5 film was deposited in the same batch, the thickness of Yb:Ta_2O_5 in buried channel waveguide is as the same as the strip loaded waveguide, which is 386 ± 10 nm. The side wall angle was measured to be ~88°.

The polymer based buried channel waveguide was successfully made in collaboration with VTT Finland. However, due to the natural limitation of the sputtering process, the waveguide ended up with a curved top surface and side wall deposition. Besides, the thickness of deposited waveguide decreases with the decreasing of trench opening, limiting the minimum size of the waveguide that can be made. This issue may be addressed by replacing the overcut trench structure with undercut trench structure.

Bibliography

[1] Hari Singh Nalwa, Handbook of Surfaces and Interfaces of Materials, Elsevier Press (2001)

[2] M. F. A. Muttalib *et al.*, "*Anisotropic Ta_2O_5 waveguide etching using inductively coupled plasma etching*", Journal of Vacuum Science & Technology A, **32**, 041304 (2014)

[3] H. Deutsch *et al.*, "*Basic Mechanisms in Plasma Etching*", Contributions to Plasma Physics, Vol. 29, Issue 3 (1989)

[4] M. Sugawara, Plasma Etching: Fundamentals and Applications, Oxford Science Publications (1998)

Chapter 5: Yb:Ta_2O_5 Thin Film Properties

5.1 Introduction

This chapter presents the experimental procedures used to characterize the properties of Yb:Ta_2O_5 thin film. Characterization results of refractive index, Yb concentration, photoluminescence strength and propagation loss of planar Ta_2O_5 and Yb:Ta_2O_5 layer are shown.

5.2 Experimental Procedures

5.2.1 **Refractive indices**

The refractive index n (known as the real part of the complex index of refraction) and the extinction coefficient k (known as the imaginary part of the complex index of refraction) are two of the most fundamental components of an optical material. Together they describe how light propagates through the medium. The refractive indices were measured using Ellipsometry which uses a linearly polarized beam to illuminate the sample and analyses the change in the circularly or elliptically reflected beam. The measurement process is shown in the *Figure 5.1*.

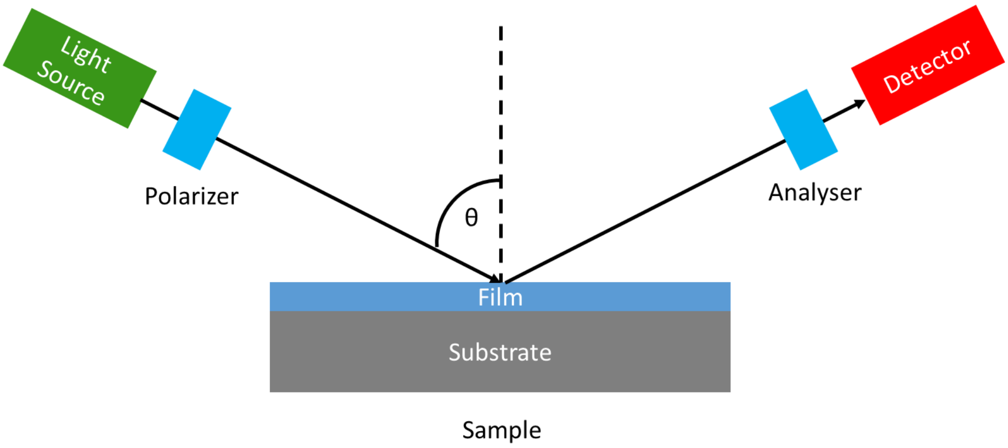

Figure 5.1 Work schematic of Ellipsometry

Together the light source and the polarizer generates an incident light with known polarization. After being reflected of the sample, the polarization of the light will change. The polarization of reflected light will be measured by the analyser and detector. After measuring the film, the data will be analysed. The processes are: a model with some estimated parameters is built to get a preliminary calculation of the predicted result. The calculated values will then be compared to the measured data to determine if the prediction is accurate. If they are not matching very well, one can vary the estimated parameters and repeat calculation and comparison processes until the prediction is well matched with the measured data. *Figure 5.2* shows the flowchart of analysis processes.

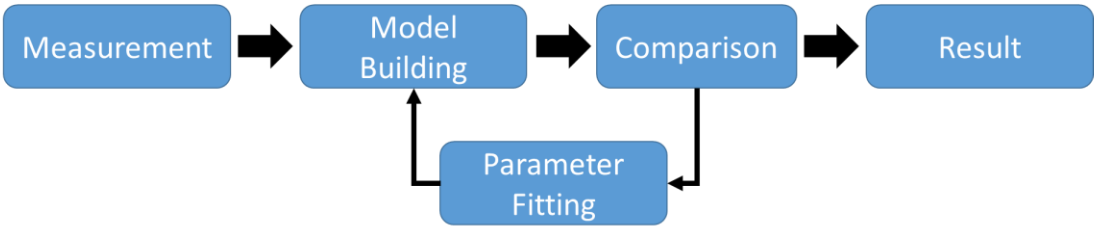

Figure 5.2 Flow chart of data analysis of Ellipsometry

In this measurement, a Cauchy model was chosen to predict the performance of the thin film as the Yb:Ta_2O_5 film is a transparent material. The Cauchy model is based on the Cauchy's equation which was defined by Augustin-Louis Cauchy[1]. It gives the relationship between the refractive index and the wavelength of light of a fully transparent material (i.e. assume $k = 0$).

$$n(\lambda) = A + \frac{B}{\lambda^2} + \frac{C}{\lambda^4} + \cdots \qquad Eq.5-1$$

where $n(\lambda)$ is the refractive index of the material at wavelength λ, coefficient A sets the range of the index and coefficients B, C, etc. describe the shape of dispersion.

The deposited thin film can be regarded as the mixture of two alloys – Yb_2O_3 and Ta_2O_5. Pure Yb_2O_3 and Ta_2O_5 have refractive indices of 1.951 and 2.146 at wavelength of 633 nm, respectively. According to the mixing rules: the refractive index of the film at 633 nm can vary from 1.951 (for the case of no Ta_2O_5 existed in the film) to 2.146 (for the case of no Yb_2O_3 existed in the film). Thus, the more Yb dopants in the sample, the lower the refractive index of the sample will be.

By assuming a mixing factor γ_{mx}, the refractive index of the Yb:Ta_2O_5 can be expressed as:

$$n_{Yb:Ta_2O_5} = \gamma_{mx} n_{Yb_2O_3} + (1 - \gamma_{mx}) n_{Ta_2O_5} \qquad Eq.5-2$$

where $n_{Yb_2O_3}$ is the refractive index of pure Yb_2O_3 and $n_{Ta_2O_5}$ is the refractive index of pure Ta_2O_5.

Therefore the mixing factor γ_{mx} can be calculated by rearranging the Eq. 5-2 and fitting the refractive index of the film, core material and cladding material in.

$$\gamma_{mx} = \frac{n_{Ta_2O_5} - n_{Yb:Ta_2O_5}}{n_{Ta_2O_5} - n_{Yb_2O_3}} \qquad Eq.5-3$$

However, the calculated mixing factor is a relative concentration that can only indicate the concentration relationship between each of the different samples. On the other hand, if the absolute value of the composition for one of those samples is known, the rest of them can be calculated without a complicated compositional analysis.

5.2.2 **X-ray Photoelectron Spectroscopy (XPS)**

Since the mixing factor only provides relative concentration, an XPS measurement was applied to obtain the absolute concentration of Yb element inside the Ta$_2$O$_5$ film.

The XPS is an analytical technique used for elemental analysis of a sample. The working principle of XPS is to irradiate the sample surface with a focused beam of X-ray and measure the kinetic energy and number of electrons that escape from the top of the material. *Figure 5.3* shows the operation of the XPS measurement and the spot size of the focused X-ray that used in the measurement. The measurement analyses the elemental composition of the top 10 nm of the sample surface. The measuring radius is 400 µm.

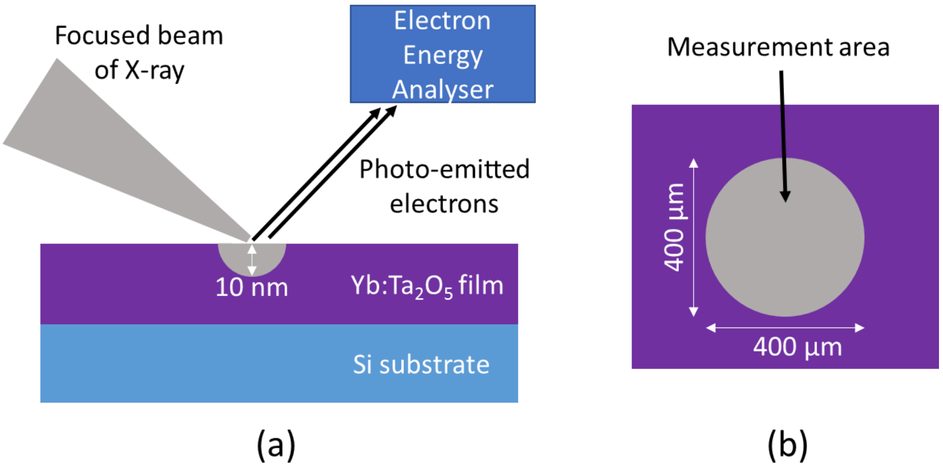

Figure 5.3 (a) Operation of XPS measurement and (b) Spot size of the focused X-ray

Since each element has its typical set of peaks at a characteristic binding energy, the elements that exist in or on the surface of the sample can be identified and quantified via plotting the electron spectrum (i.e. electron counts versus binding energy). *Figure 5.4* shows the basic physics of XPS. The electron of an ion absorbs the pumped X-ray photon and escapes from its orbit with certain amount of kinetic energy. The escaped electron will then be captured by the electron energy analyser and its kinetic energy can be measured. Because the photon energy of the X-ray and the kinetic energy of the electron are known, the binding energy can be calculated by subtracting the electron kinetic energy from the X-ray photon energy as shown in Eq. 5- 4:

$$Binding\ Energy = h\nu - Kinetic\ Energy \qquad Eq. 5-4$$

Therefore, the origin ion of this escaped electron can be distinguished via matching the characteristic binding energy of known materials. The number of escaped electrons with certain binding energy represent the number of this kind of ion in the measurement area.

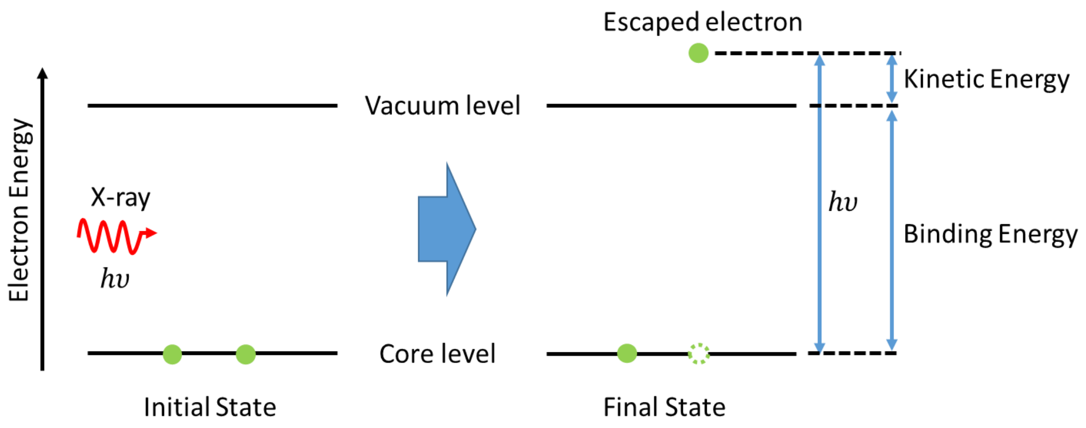

Figure 5.4 Schematic of basic physics used by XPS measurement

The system used for the measurement is the ThermoVG XPS Thetaprobe. In order to avoid measuring at an over-doped or under-doped position, the electron spectrum were measured at different points.

5.2.3 **Surface Photoluminescence (PL) Characterization**

The photoluminescence is light emission from any material due to the absorption of photons. For the sake of finding the right doping concentration of the material that can offer the maximum fluorescence, a photoluminescence measurement is needed.

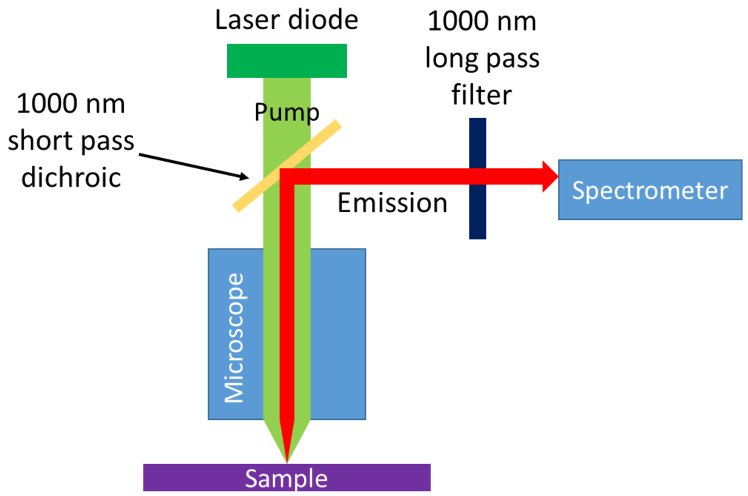

Figure 5.5 Schematic of surface PL measurement system

Figure 5.5 shows the configuration of the PL measurement system. The system consists of 5 main parts: a laser diode, a microscope, a spectrometer, a 1000 nm short pass dichroic filter and a 1000 nm long pass filter. The working principle of this measurement is quite straight forward. The laser diode works as a pump source, which generates a laser beam at 980 nm wavelength. As a 1000nm short pass dichroic filter was used, the pump beam from laser diode passes it and enters into the microscope without being reflected. The microscope focuses the pump beam onto the sample surface and collects the emission from the sample which was caused by the PL process. The emission is collimated into a beam and reflected by the dichroic as its wavelength is longer than 1000 nm (i.e. 1020 nm – 1100 nm). Before entering the spectrometer, there is 1000 nm long pass filter which blocks any possible reflected pump light. The spectrometer then measures the photo luminescence emitted from the sample.

5.2.4 **Planar Layer Propagation Loss**

The mode propagation loss of the Yb:Ta$_2$O$_5$ and Ta$_2$O$_5$ planar waveguides were measured to ensure the deposited film is of good quality. The loss can be determined by measuring the scattered light from the surface of the planar layer. By assuming the amount of light that scattered from the surface is proportional to the light that propagates inside the planar waveguide, the decaying rate of scattered light should mimic that of the propagating light inside the waveguide, thus the propagation loss can be calculated[2].

Therefore, the propagation loss of the film over unit distance can be expressed as:

$$Loss\ (dB)_{Propagation} = log_{10}\frac{I}{I(0)} = log_{10}\frac{I\ \times\ \alpha_{scattering}}{I(0)\ \times\ \alpha_{scattering}}$$

$$= log_{10}\frac{I_{scattered}}{I(0)_{scattered}} \qquad Eq.5-5$$

where the $I(0)_{scattered}$ and $I_{scattered}$ are the scattered intensity measured from the top of the layer at the start position and after an unit length, respectively, $\alpha_{scattering}$ is the scattering ratio of the waveguide.

Both Yb:Ta$_2$O$_5$ and Ta$_2$O$_5$ were deposited in the same batch of strip loaded samples to keep the consistence of the measurements. A 2 µm thick thermal silica substrate was used for each materials to form a planar waveguide.

Figure 5.6 illustrates the configuration of the planar layer propagation loss measurement. Prism coupler measurement (Metricon 2010/M) was used in this measurement. The 633 nm CW laser was coupled into the top layer through a prism. A fibre that can travel along the laser propagation trace was used to measure the decrease of light intensity with distance.

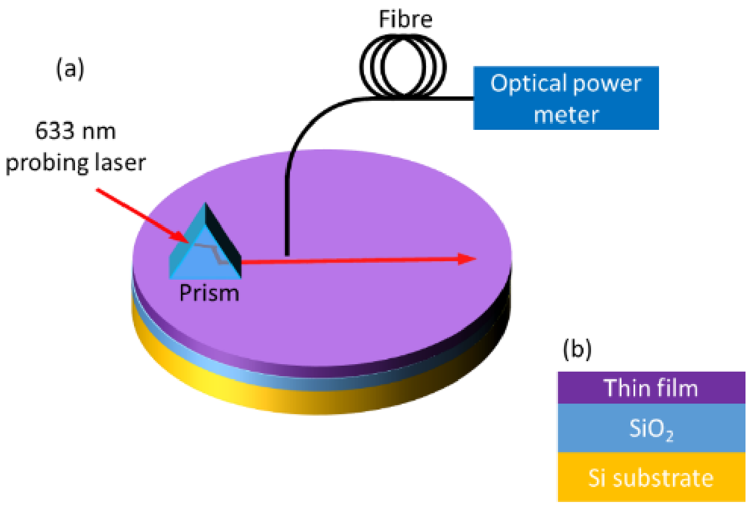

Figure 5.6 Schematics of (a) planar waveguide loss measurement and (b) layer stack of measured planar waveguide

5.3 Results and Discussions

5.3.1 Refractive Indices and Mixing Factor

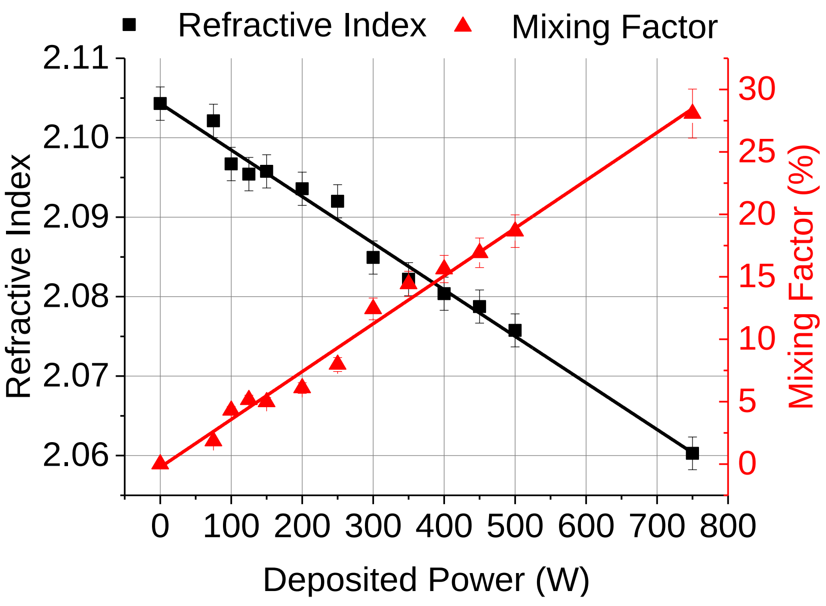

Figure 5.7 Refractive indices of Yb:Ta_2O_5 sample with different doping plasma powers at wavelength of 1100 nm and correspond mixing factor

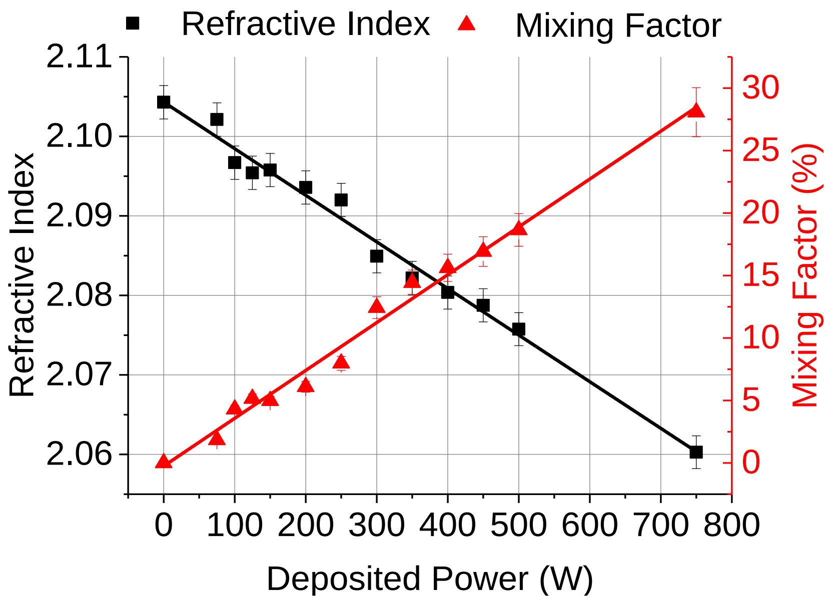

Figure 5.7 displays the curve of the measured refractive indices by Ellipsometry at wavelength of 1100 nm and the mixing factor of the Yb:Ta_2O_5 thin film with different deposition powers. As described in the Section 5.2.1, the measurement used Cauchy to fit the refractive indices of the film. The mean squared error (MSE) ranged 16 to 50 depending on the sample condition (i.e. doping concentration, cleanliness, uniformity, etc.). A fitting with less than 100 MSE is considered a reasonable fit, the smaller MSE the better. A well-designed model for a known material will have a MSE which is less than 10. In this measurement, multiple point measurement was taken and the smallest MSE results (i.e. best fits) are shown.

The measurement wavelength range was defined from 500 nm to 1200 nm but only 1100 nm data was shown as it is the longest emission wavelength for Yb dopants in common materials. It is easy to see that the real part of the refractive index decreases with increasing of deposition plasma power. The measured curve proves that the higher the deposition power is, the higher the Yb doping concentration is. It is also notable that for the highest deposition power 750W, the film still shows a relatively high refractive index of 2.06.

5.3.2 **Yb concentration measured by XPS**

Figure 5.8 shows the electron spectrum that was measured from an Yb:Ta_2O_5 sample with Yb deposition power of 250W, 500W and 750W, respectively. It is clear that with the increasing deposition power, the electron counts for both Yb 4p1 and Yb 4d5 increase, suggesting the increment of the Yb concentration.

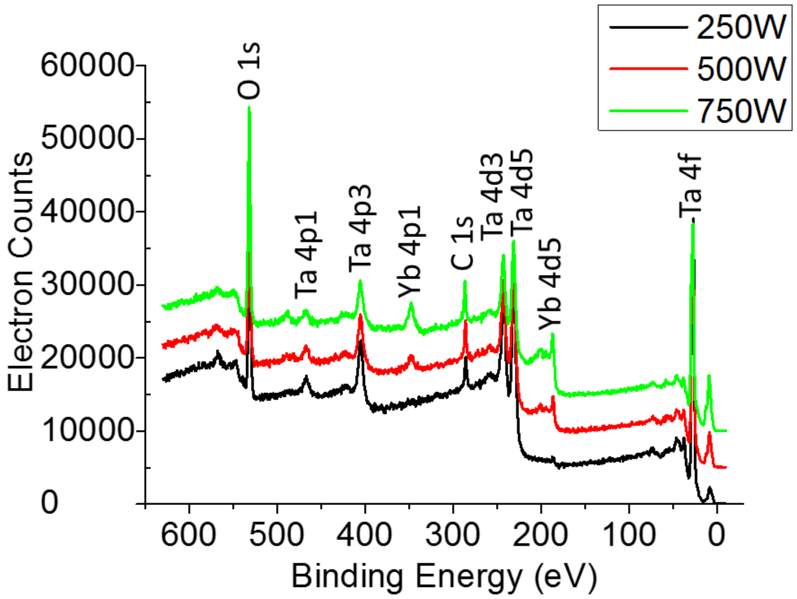

Figure 5.8 Electron spectrum of Yb:Ta_2O_5 sample with Yb deposition power of 250W, 500W and 750W

Figure 5.9 plots of the calculated Yb atomic percentage (at.%) of the thin film of different Yb deposition powers through the measured electron spectrum by Thetaprobe software together with the mixing factor that was obtained from the film refractive indices.

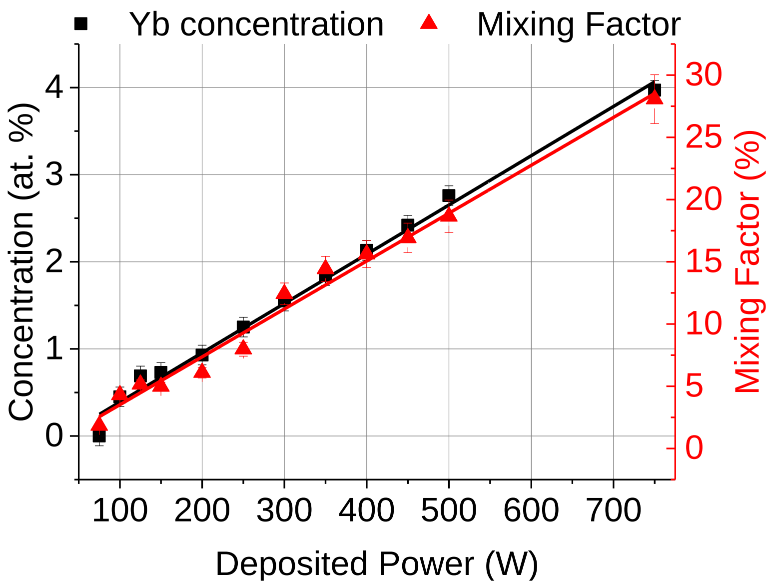

Figure 5.9 Mixing factor and measured Yb concentration with respect of Yb deposition power

In order to confirm the reliability of the mixing factor and to find out the relationship between the mixing factor and the actual Yb concentration (in at.%), both the mixing factor and the actual measured Yb concentration have been normalized and plotted in *Figure 5.10*. It is clear that the two trend lines have the same slope but slightly different offset, which means the mixing factor and actual concentration is linear related. Therefore, the relationship of them can be expressed by:

$$Yb(\%\,at.) = \delta\gamma_{mx} \qquad Eq.5-6$$

where δ is the converting factor for converting the mixing factor to the actual Yb atomic percentage in the Yb:Ta_2O_5 film.

Thus,

$$\delta = \langle\frac{Yb(\%\,at.)}{\gamma_{mx}}\rangle = 0.1414 \qquad Eq.5-7$$

Therefore, for a Yb:Ta_2O_5 thin film with known mixing factor, the concentration can be estimated using Eq. 5-6 with $\delta = 0.1414$.

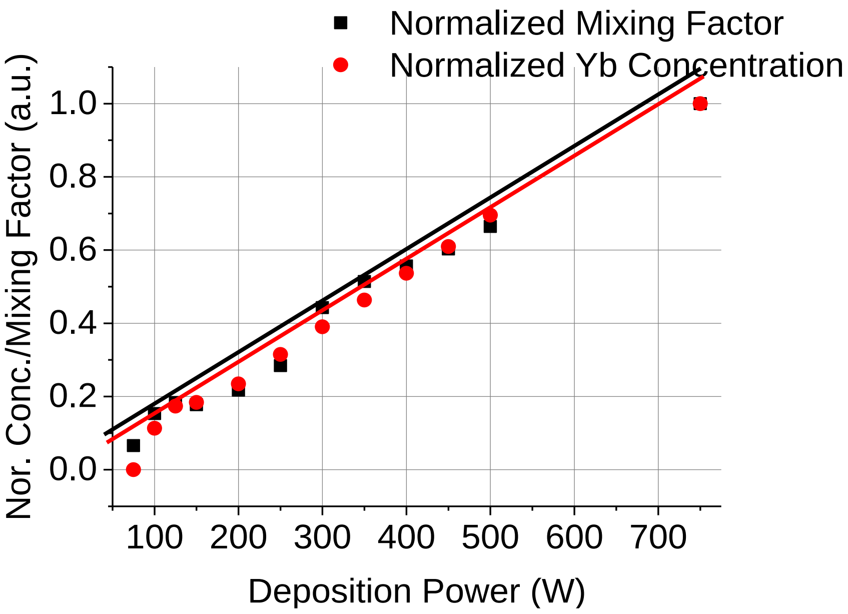

Figure 5.10 Normalized mixing factor and normalized Yb concentration with respect of Yb deposition power

5.3.3 Surface PL Measurement

The measured photoluminescence intensity is expected to grow with the increase of the Yb concentration and to reach its peak at certain concentration. Then it is expected to decrease with the increase of Yb concentration due to multi-ion interactions.

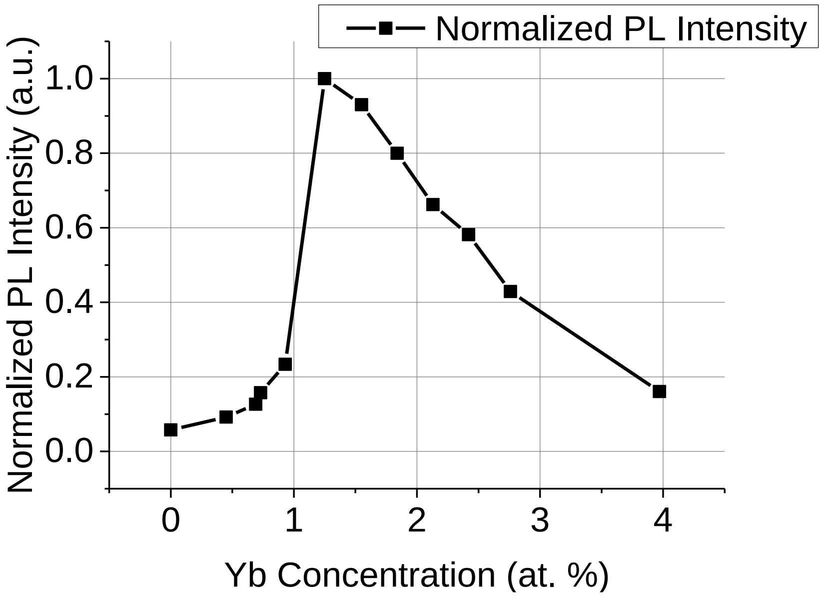

Figure 5.11 Normalized PL intensity collected from top of the thin film with respect of the sample Yb concentration

Figure 5.11 shows the results of the PL measurement for samples at different Yb concentrations. The sample that has 1.25 at.% Yb concentration, which corresponds to 250W in deposition power, has the highest photoluminescence. Hence, the Yb concentration of the laser gain material will be set to 1.25 at.% (250W in deposition power). By overwriting the Yb concentration in the gain simulation performed in Section 3.4.2 to 1.25 at.%, the saturated gain was simulated to be 1.46 dB /mm.

5.3.4 Planar Layer Propagation Loss

Since the Yb doping concentration of the laser gain material was chosen as 1.25 at.% (equivalent to 250 W Yb deposition power) according to the results shown in Section 5.3.3, the sample that being measured for its planar layer propagation loss was fabricated to have the same doping concentration.

The results of planar layer propagation loss measurement of 250W Yb:Ta_2O_5 film and pure Ta_2O_5 film are shown in *Table 5.1*. Both films show a low propagation loss before annealing, which indicates the deposited films are of high quality. The loss within the thin film was further reduced by the annealing process.

Table 5.1 Measured propagation loss for Yb:Ta_2O_5 and Ta_2O_5 planar waveguide before and after annealing

Thin film	***Loss before annealing***	***Loss after annealing***
Yb:Ta_2O_5	*0.96 dB/cm*	*0.20 dB/cm*
Pure Ta_2O_5	*0.54 dB/cm*	*0.10 dB/cm*

After annealing, the propagation loss of the 400 nm thick Yb:Ta_2O_5 planar waveguide drops to 0.20 dB/cm, which is nearly an order of magnitude lower than the Yb doped planar waveguide made of YAG (1 µm thick, 2 dB/cm), KGdW (20 µm thick, 2.1 dB/cm) and Y_2O_3 (6 µm thick, 1.4 dB/cm) [3-5]. There are also other Yb doped planar waveguides which have lower propagation loss but all of them are considerably thicker than the Yb:Ta_2O_5 planar waveguide presented in this work, for example, Yb:KYW planar waveguides reported by Y. E. Romanyuk *et al.* and F.M. Bain *et al.,* has achieved 0.08 dB/cm (17 µm thick) and 0.06 dB/cm (14 µm thick) propagation loss, respectively[6,7].

Same as the Yb:Ta_2O_5, the pure Ta_2O_5 film also benefits from annealing, resulting in a reduced propagation loss of 0.10 dB/cm. The other common waveguide materials such as Y_2O_3 (850 nm thick, 1.11 dB/cm), Al_2O_3 (740 nm thick, 0.12 dB/cm) and TiO_2 (358 nm thick, 0.5 dB/cm) are as well showing low propagation loss but still higher than pure Ta_2O_5 film made in this work, which proves the potential of the films that fabricated using the method mentioned in Chapter 4[8,9].

5.4 Summary

The optical properties and the stoichiometry of the Yb:Ta_2O_5 have been investigated in this chapter. The refractive indices for samples prepared with different deposition power were measured. The measurements show that the refractive index drops with increasing deposition power, indicating that the Yb concentration increases with the deposition power. An XPS characterization was futher applied in order to relate the mixing factor that was calculated by the film refractive index to the actual Yb concentration.

Furthermore, the photoluminescence (PL) of each sample prepared with different deposition power was measured using a surface PL measurement system. The results show the highest PL was obtained from the 250W sample (1.25 % at. Yb concentration) which suggests that the waveguide device should be made using this concentration. By updating the Yb concentration in the simulation in Section 3.4.2 to 1.25 at.%, the maximum gain of 1.46 dB/mm was obtained.

Finally, the propagation loss of both the pure Ta_2O_5 and 250W Yb:Ta_2O_5 thin film was measured. After annealing, the loss of Ta_2O_5 dropped from 0.54 dB/cm to 0.10 dB/cm and the loss of Yb:Ta_2O_5 decreased from 0.96 dB/cm to 0.20 dB/cm.

Biblography

[1] C. B. Layne *et al.*, "*Multiphonon relaxation of rare-earth ions in oxide glasses*", Physical Review B, **16**, 1, 10-21 (1976)

[2] R. G. Hunsperger, Integrated Optics: Theory and Technology, Springer (2009)

[3] D. C. Hanna *et al.*, "*Quasi-three level 1.03 μm laser operation of a planar ion-implanted Yb:YAG waveguide*", Optics Communication, **99**, 211-215 (1993)

[4] F.M. Bain *et al.*, "*Ultrafast laser inscribed Yb:KGd(WO_4)$_2$ and Yb:KY(WO_4)$_2$ channel waveguide lasers*", Optical Express, **17**, No. 25, 22417 (2009)

[5] S. J. Beecher *et al.*, "Diode-end-pumped 1.2 W Yb:Y_2O_3 planar waveguide laser", Optics Express, Vol. 22, **Issue 18**, pp. 22056-22061 (2014)

[6] Y. E. Romanyuk *et al.*, "*Yb-doped KY(WO_4)$_2$ planar waveguide laser*", Optical Letters, **31**, No. 1, 53 (2006)

[7] F.M. Bain *et al.*, "*Continuous-wave and Q-switched operation of a compact, diode-pumped Yb^{3+}:KY(WO_4)$_2$ planar waveguide laser*", Optical Express, **17**, No. 3, 1666 (2009)

[8] J. D. B. Bradley *et al.*, "Fabrication of low-loss channel waveguides in Al_2O_3 and Y_2O_3 layers by inductively coupled plasma reactive ion etching", Appl. Phys. B **89**, 311–318 (2007)

[9] T. Touam *et al.*, "*Low Loss Sol-Gel TiO_2 Thin Films for Waveguiding Applications*", Coatings 2013, **3**, 49-58

Chapter 6: $Yb:Ta_2O_5$ Strip Loaded Nanowire Waveguide Laser on Silicon

6.1 Introduction

Building upon the waveguide designs described in Chapter 3, the fabrication processes demonstrated in Chapter 4 and the $Yb:Ta_2O_5$ thin film characterization in Chapter 5, this chapter presents the work that carried out to characterize the waveguide properties and CW lasing behaviour of the $Yb:Ta_2O_5$ strip loaded nanowire waveguide. Due to time limitations, the other two kinds of devices (buried nanowire approach and polymer buried nanowire approach) could not be measured.

6.2 Experimental Procedures

6.2.1 Insertion loss Characterization

Insertion loss is the loss of signal power which results from the insertion of light to the device, which is a waveguide in this case. It represents the loss of the whole optical device, including the loss in the device and at the optical interface. Since any polishing defect or broken waveguide will lead to high insertion loss, the quality of the waveguide device can be determined by assessing its insertion loss. [1]

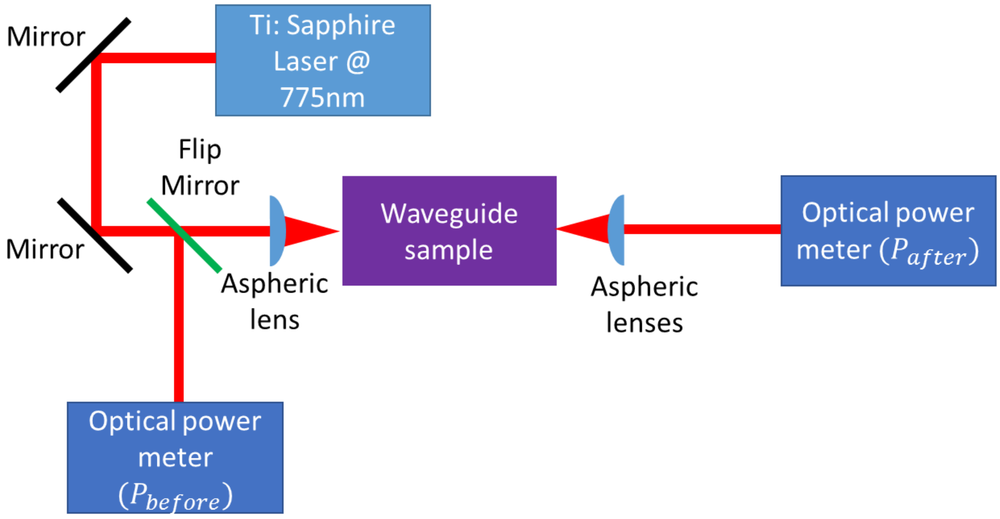

Figure 6.1 Schematic of insertion loss measurement

If the power transmitted to the waveguide before insertion is P_{in} and the power measured by the waveguide after the insertion is P_{out}, the insertion loss can be expressed as,

$$Loss\ (dB)_{Insertion} = 10 \times log_{10} \frac{P_{out}}{P_{in}} \qquad Eq. 6-1$$

Figure 6.1 illustrates the schematic of the loss measurement. A Ti: Sapphire laser that emits 775 nm wavelength light was used as pump source for the measurement since the absorption at this wavelength is very weak for Yb^{3+} ions. Due to the short focal length (3.1 mm) of the lenses, the power meter cannot be inserted between the lens and waveguide sample. Instead, the input power and output power was measured in front of the focusing lens ($P_{before\ focusing\ lens}$) and after the collecting lens $P_{after\ collecting\ lens}$, respectively. To calculate the accurate insertion loss of the waveguide, the power decay after each lens has to be taken into consideration. The power decay $\alpha_{\ lens}$ of the light that passes the focusing lens was measured to be 0.95. Hence Eq. 6-1 can be re-written as

$$Loss\ (dB)_{Insertion} = 10 \times log_{10} \frac{P_{out}}{P_{in}} = 10 \times log_{10} \frac{P_{after\ collecting\ lens} / \alpha_{lens}}{P_{before\ focusing\ lens} \times \alpha_{lens}} \qquad Eq. 6-2$$

6.2.2 Waveguide Propagation Loss Measurement

The propagation loss of the strip loaded waveguide sample was measured by using a Fabry-Perot (FP) loss measuring method. This method is based on the contrast of Fabry-Perot resonances measured from the polished and parallel end facets that are perpendicular to the waveguide at both ends of the waveguide [2].

Due to the setup was not being owned locally, only one lasing waveguide with total length of 6.7 mm containing 2.5 mm 400-nm-wide nanowire (i.e. Part A in *Figure 3.7 (a)* is 2.5 mm long, 400 nm wide) was tested. The measurement system used is called Agilent lightwave and has a tuneable DFB laser source and an optical power meter integrated in it. The schematic of the FP loss measurement is shown in *Figure 6.2* – the probe laser was butt-coupled into the waveguide by a fibre and the light output from the waveguide was collected by another fibre and was sent into an optical power meter. By changing the probe laser wavelength from 1445 nm to 1448 nm in steps of 10 pm, an output power spectrum was collected at the other end of the waveguide.

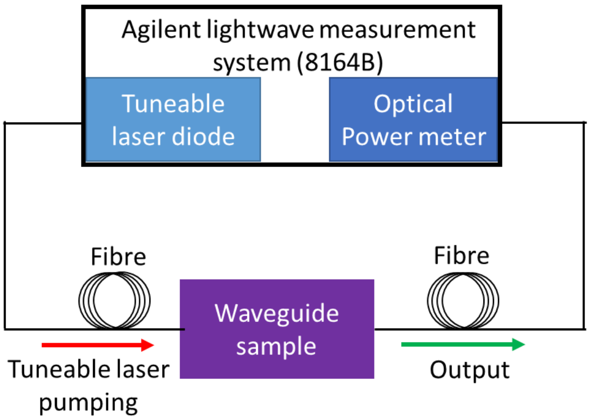

Figure 6.2 Setup for waveguide Fabry-Perot loss measurement

Assuming both end facets are perfectly polished and are perpendicular to the waveguide, the propagation loss of the waveguide can be expressed as [2]:

$$Loss(dB)_{Propagation} = 4.34 \times \left[ln(R) - ln\frac{1-\sqrt{1-\gamma^2}}{\gamma} \right] \qquad Eq.6-3$$

in which,

$$\gamma = \frac{I_{max} - I_{min}}{I_{max} + I_{min}} \qquad Eq.6-4$$

$$R = \frac{(n_{eff} - n_{air})^2}{(n_{eff} + n_{air})^2} \qquad Eq.6-5$$

where R is the reflection coefficient caused by Fresnel reflection between the waveguide end facet and air, n_{eff} and n_{air} is the refractive indices of the propagation mode inside the waveguide and the air, I_{max} is the maximum output intensity and I_{min} is the minimum output intensity.

6.2.3 Excited State Lifetime Characterization

Excited state lifetime is an important parameter for a laser device. The longer the lifetime is, the easier population inversion can be achieved. The lifetime measurement was performed on a Yb:Ta_2O_5 strip loaded waveguide sample with a total length of 6.7 mm. The experimental set up is shown in *Figure 6.3*. The pumping setup for this measurement was the same as for the fluorescence spectrum measurement, except the light from pump laser diode was chopped using a mechanical chopper. The chopping frequency was set to 240 Hz to avoid possible interference from the 50 Hz noise of the power line. The pump power was kept minimum so that amplified spontaneous emission (ASE) can be remain minimal. The waveguide output light was filtered with a long pass filter that has a cut-off wavelength of 1000 nm to eliminate interference from the pump. The filtered signal was sent into a fast-response silicon photo-detector which was directly connected to an oscilloscope.

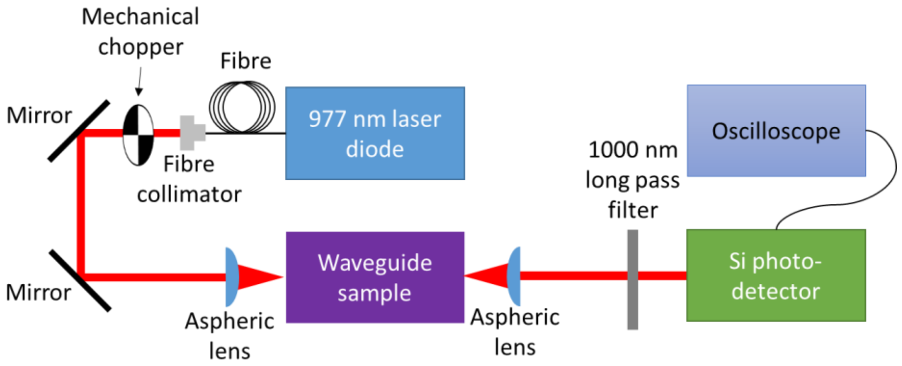

Figure 6.3 Setup of excited state lifetime measurement

6.2.4 Lasing Characterization

After characterizing the optical properties of the waveguide, the waveguide sample was tested for its lasing performance. Amongst all the waveguides, lasing was observed in two waveguides that have a 2.5 mm nanowire (i.e. Part A in *Figure 3.7 (a)*) length and nanowire widths of 400 nm and 600 nm (the total waveguide length is 6.7 mm). *Figure 6.4* shows the experimental setup for the lasing measurement. The waveguide was pumped at the end facet with a 977 nm laser diode, and the output of the waveguide was divided into two parts by a 50:50 beam splitter so that both the output power and the output spectrum can be observed simultaneously. There was no mirror attached at either end facets, hence the optical cavity was formed by Fresnel reflection only.

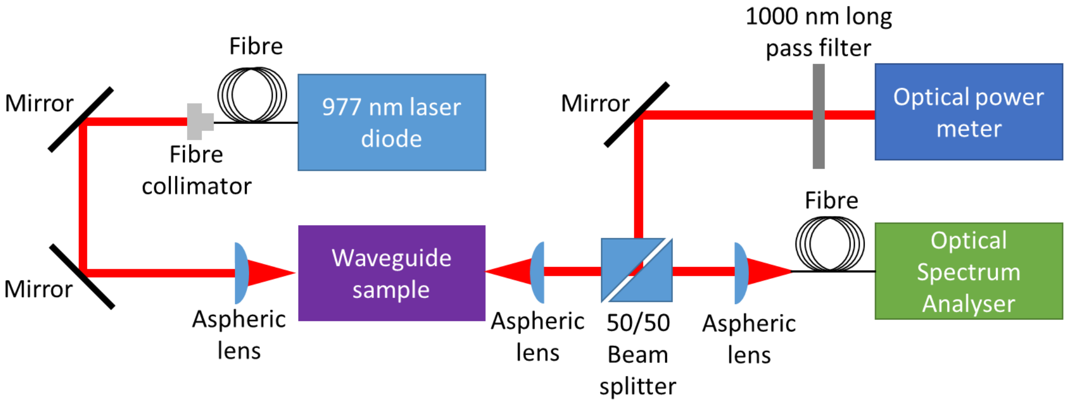

Figure 6.4 Schematic of lasing measurement

6.3 Results and Discussions

6.3.1 Waveguide Insertion Loss

Figure 6.5 shows the insertion losses measured from waveguides with different nanowire lengths and widths and the best linear fits for each nanowire width data sets. The slope of each linear fit curve represents the propagation loss for a unit length of the nanowire, the steeper the slope is, the higher the nanowire propagation loss is. The interception point with line X = 0 (Y-axis) indicates the loss including the coupling loss, coupler waveguide loss and taper waveguide loss.

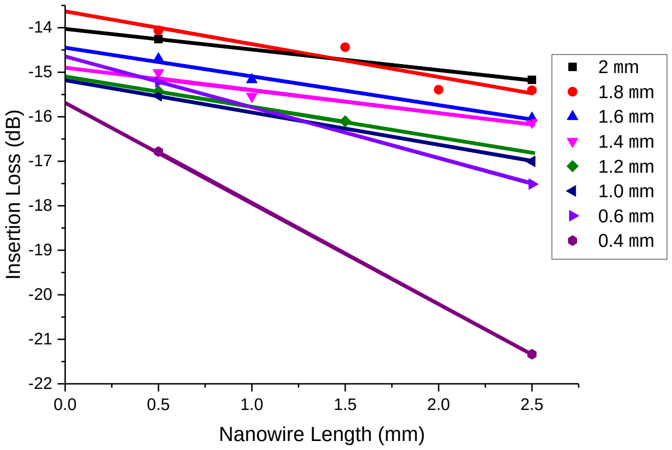

Figure 6.5 Insertion losses of waveguides with different nanowire length and width

Table 6.1 summarised the nanowire propagation loss and coupling loss of the nanowire that includes air-waveguide coupling loss, coupler propagation loss and taper propagation loss. As discussed in Chapter 2 and Chapter 3, the narrower the nanowire is, the more the propagation mode overlaps with the nanowire sidewall. As a consequence, the mode will suffer more from the loss cause by imperfection sidewalls, i.e. higher loss will occur. In *Table 6.1*, there are few data points which do not follow the expected trend from the theory and simulation in Chapter 2 and Chapter 3 but this is mainly due to fabrication errors. Apart from these points, both the nanowire propagation loss and the coupling loss of the nanowire show that the narrower nanowire the higher loss.

Table 6.1 Calculated nanowire propagation loss and coupling loss for waveguide with different nanowire widths

	2.0 µm	1.8 µm	1.6 µm	1.4 µm	1.2 µm	1.0 µm	0.8 µm	0.6 µm	0.4 µm
Nanowire Propagation Loss (dB/mm)	-0.46	-0.74	-0.64	-0.51	-0.67	-0.73	N/A	-1.14	-2.27
Coupling loss (dB)*	-14.02	-13.61	-14.43	-14.86	-15.09	-15.16	N/A	-14.64	-15.64

*‘Coupling loss’ here means the coupling loss of the nanowire, which includes the air-waveguide coupling loss, coupler loss and taper loss.

Figure 6.6 shows the insertion losses for waveguides that have a 2.5mm-long nanowire section with different nanowire widths. This set of waveguides is particularly interested because of it has the longest nanowire section among the other waveguide sets which has higher power density inside of it. As expected, the insertion loss increases with decreasing nanowire width. The insertion losses of waveguides with 800 nm and 1200 nm nanowire widths were not measurable since there are fabrication induced breakage existing in the middle of the waveguides.

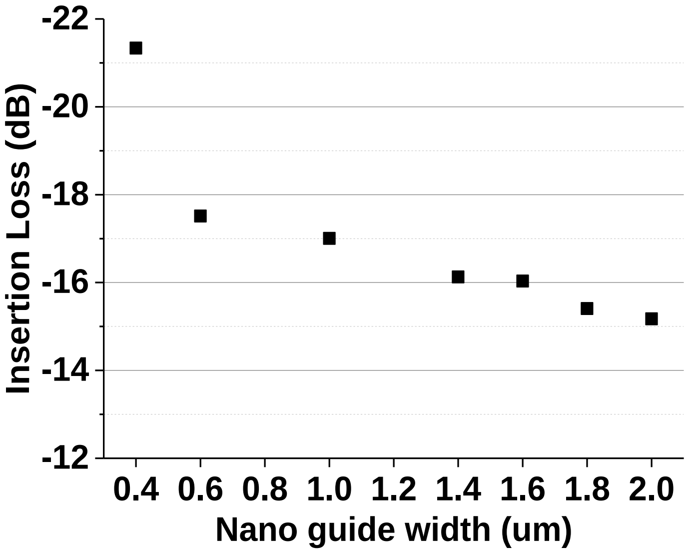

Figure 6.6 Insertion losses measured from waveguide contains 2.5-mm-long nanowire with different widths (0.8 µm and 1.2 µm data missing due to broken waveguide)

6.3.2 Waveguide Propagation Loss

The measured sample is the 6.7 mm long waveguide with 400 nm wide nanowire. The measured output intensity versus probe wavelength is plotted in *Figure 6.7*. The red line is a sine fit of measured intensity. The propagation loss of the waveguide is calculated by using the maximum and minimum intensity extracted from the figure and is found to be -7.772 dB.

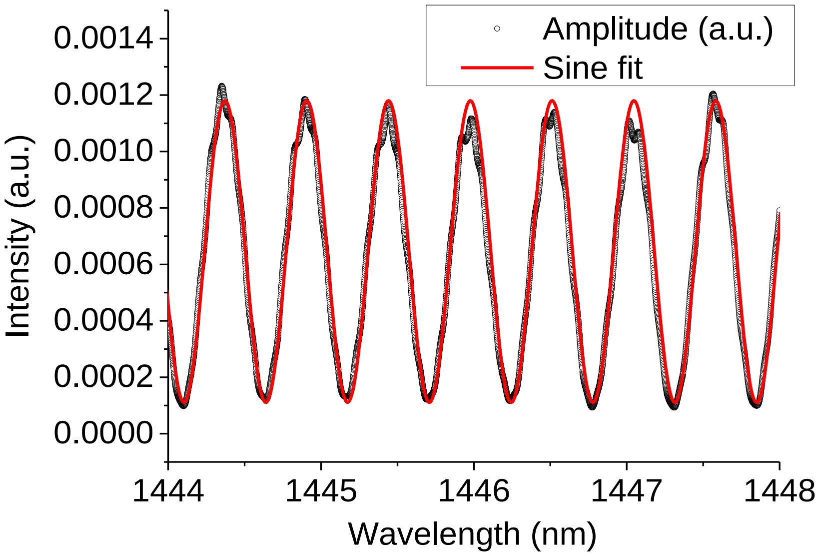

Figure 6.7 Normalized waveguide output intensity versus pump wavelength

6.3.3 Blue Luminescence

When end pumped by 977 nm laser diode, a visible blue luminescence was observed from the waveguide.

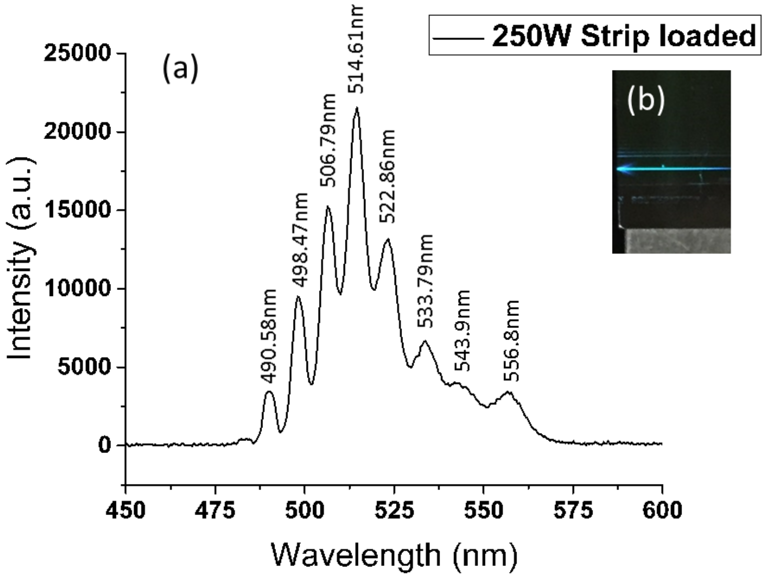

Figure 6.8 (a) Spectrum of blue luminescence and (b) Optical photo of the luminescence taken from the top of the waveguide.

Figure 6.8 (a) and (b) shows the spectrum of the blue luminescence and an optical picture of it, respectively.

There are three possible physical mechanisms responsible for the blue luminescence: emission from possible contamination ions (i.e. Er, Tm, Nd, etc.), the non-linear processes of the Ta_2O_5 host material, and the emission of Yb^{3+} ions. The XPS measurement of the sample suggests that there is no trace of contamination ions or that the concentration is too small (<0.1% at.) to be distinguished by XPS.

The non-linear processes that commonly exist in Ta_2O_5 are cross phase modulation (XPM)[3] and four wave mixing (FWM)[3, 4]. Both of these processes require high power pumping, ideally pulsed laser pump sources (as the peak power of pulsed laser is generally much higher than the power of CW laser), in order to be triggered. In this photoluminescence measurement, the pump source used was a CW laser maintained at a 50 mW output power, which is not likely to introduce non-linear effects. To confirm the blue luminescence is not originating from a non-linear process of Ta_2O_5, a measurement of luminescence power dependence was carried out. *Figure 6.9* plots the normalized intensity of the blue luminescence with respect to the launched pump power. It is clear that the intensity of the blue luminescence is linearly depending on the pump power, implying no non-linear process existing.

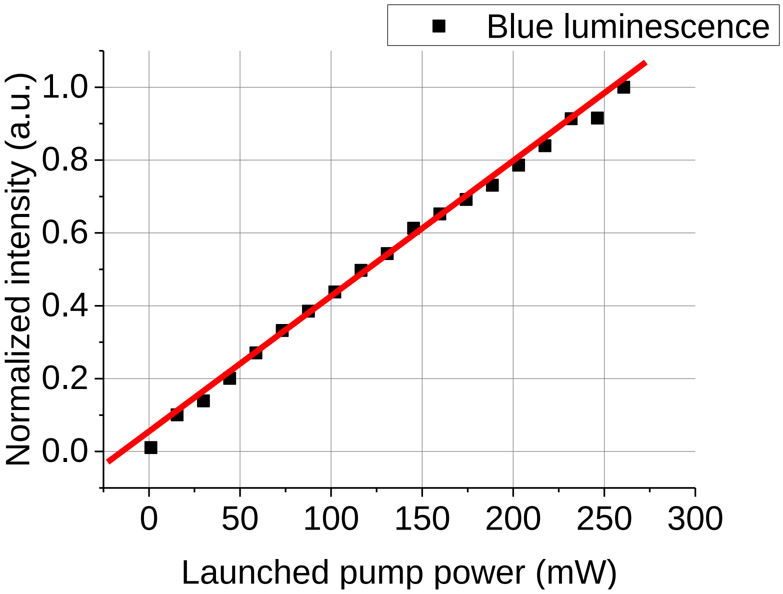

Figure 6.9 Normalized intensity of blue luminescence with respect of pumping power

Since Yb^{3+} ions only have two manifolds $^2F_{5/2}$ and $^2F_{7/2}$ (as shown in *Figure 6.10*), there cannot be any multi-photon absorption upconversion or co-operative upconversion. Therefore, the only possible process for Yb^{3+} ion that can produce blue-green light is the co-operative emission as mentioned in Section 2.3.2.4, which occurs when a pair of ions emit one photon due to simultaneous decay of electrons in from the excited states [5-9]. This luminescence is regarded as a loss mechanism because of it reduces the excited state population and thus shorten the excited state lifetime.

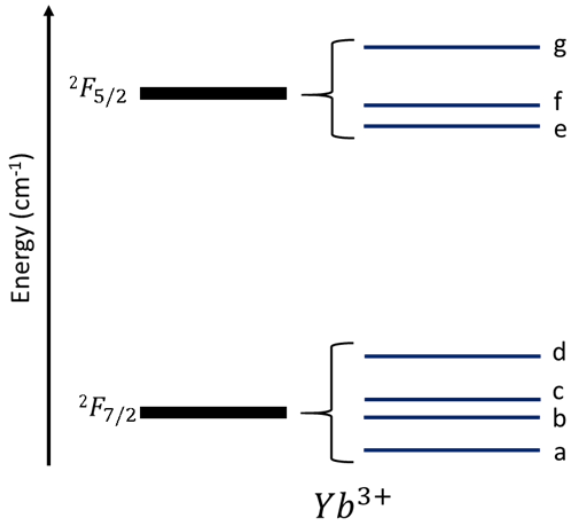

Figure 6.10 Energy diagram of Yb^{3+} ion

6.3.4 **Excited State Lifetime**

Figure 6.11 shows the normalized fluorescence power versus time. The excited state lifetime was calculated by applying an exponential decay fitting to the curve and was found to be 60 µs.

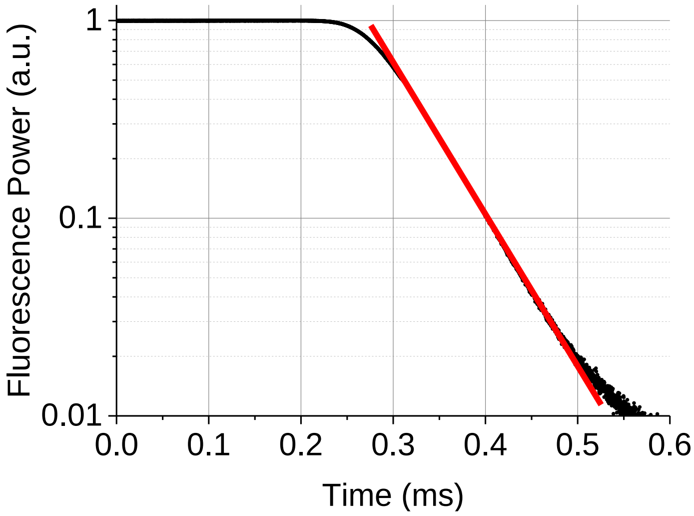

Figure 6.11 Normalized fluorescence intensity versus time

Table 6.2 lists the excited state lifetime of Yb ions in different kinds of host materials. The two Yb:Ta_2O_5 samples have the shorter lifetime when compared with all the other materials. The lifetime for Yb:Ta_2O_5 in this work was found to be 4.4 times shorter than A. Aghajani reported[10]. The reason for this is that the Yb concentration in our film is nearly one order of magnitude higher compared with A. Aghajani's. The excess amount of Yb ions will lead to an enhanced cooperative emission as mentioned in Section 6.3.3, which shortens the lifetime of the excited states.

*Table 6.2 Excited state lifetime of Yb in different hosts (*this work)*

Host material	***Ta_2O_5 ****	***Ta_2O_5 [10]***	***YAG [4]***	***YAB [4]***	***KGdW [4]***	***KYW [4]***
Concentration (10^{20})	*4.98*	*0.6*	*8.97*	*8.97*	*8.97*	*8.97*
Lifetime / μs	*60*	*260*	*951*	*680*	*600*	*600*

Figure 6.12 illustrates the simulated waveguide gain versus the pump power for excited state lifetime that taken from a reference [10] and measured excited state lifetime. The curves show that with shorter excited state lifetime, the waveguide needs higher pump to achieve the same gain when compared to the waveguide that has a longer lifetime. This is because the shorter the lifetime is, the higher the spontaneous emission rate will be.

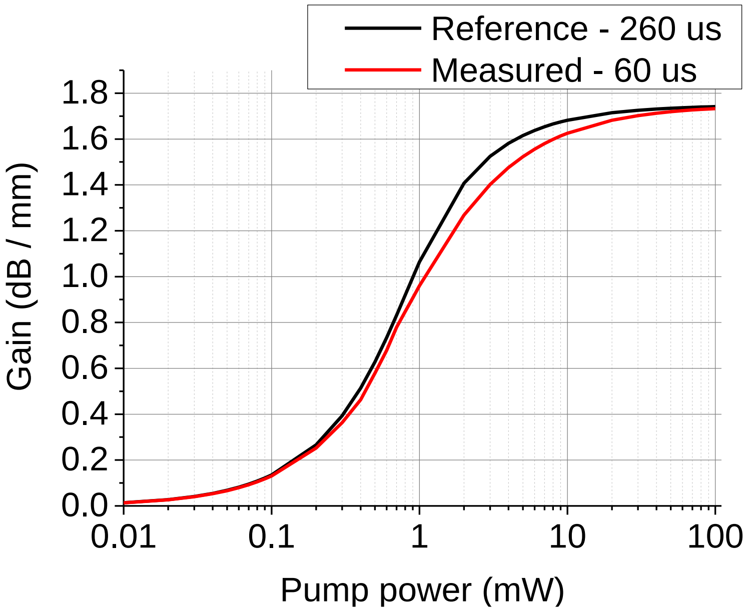

Figure 6.12 Simulated gain vs. pump power curve for 400 nm nanowire with reference and measured excited state lifetime

The ratio between the population of lasing level and ground level is given by [Appendix E]:

$$\frac{N_l}{N_g} = \frac{\sigma_{ap}\frac{I_p}{h\upsilon_p} + \sigma_{as}\frac{I_s}{h\upsilon_s}}{\sigma_{ep}\frac{I_p}{h\upsilon_p} + \sigma_{es}\frac{I_s}{h\upsilon_s} + R_{rad} + R_{nr}} \qquad Eq.E-26$$

where,

$$R_{rad} = \frac{1}{\tau_{rad}} \qquad Eq.6-6$$

$$R_{nr} = \frac{1}{\tau_{nr}} \qquad Eq.6-7$$

and τ_{rad} and τ_{nr} are the radiative (i.e. excited state lifetime) and non-radiative decay time, respectively. Since other factors other than R_{rad} and R_{nr} do not change under the same pump and signal level, Eq. E-26 can be rewritten as:

$$\frac{N_l}{N_g} = \frac{C_1}{C_2 + R_{rad} + R_{nr}} \qquad Eq.6-8$$

Because R_{nr} is very small between the lasing level and ground level (as the crystal structure cannot support large vibrations without breaking the bonds)[11], Eq. 5-19 can be further simplified as:

$$\frac{N_l}{N_g} = \frac{C_1}{C_2 + R_{rad}} \qquad Eq.6-9$$

The total population N of such a laser system equals the sum of the population of the lasing level and the ground level. Hence, the population of the lasing level is given by:

$$N_l = \frac{C_1}{C_1 + C_2 + R_{rad}} N \qquad Eq.6-10$$

Therefore, at a constant pump and signal level and for a shorter excited state lifetime, the population of the lasing level is lower compared to that of a sample with a longer excited state lifetime, leading to a lower number of stimulated emission and thus lower gain.

6.3.5 Laser Spectrum

The output spectrum of the waveguides with 400 nm and 600 nm nanowire width below and above the lasing threshold are shown in *Figure 6.13* (a) and (b). The lasing peak is located at 1026 nm and 1024 nm wavelengths, which are within the fluorescence bandwidth. Besides the lasing peak, there are some smaller peaks emerging that can be excited via tuning the excitation conditions. *Figure 6.14* shows the lasing spectrum for different coupling positions of the pump. By shifting the coupling position in horizontal direction, different lasing modes can be excited.

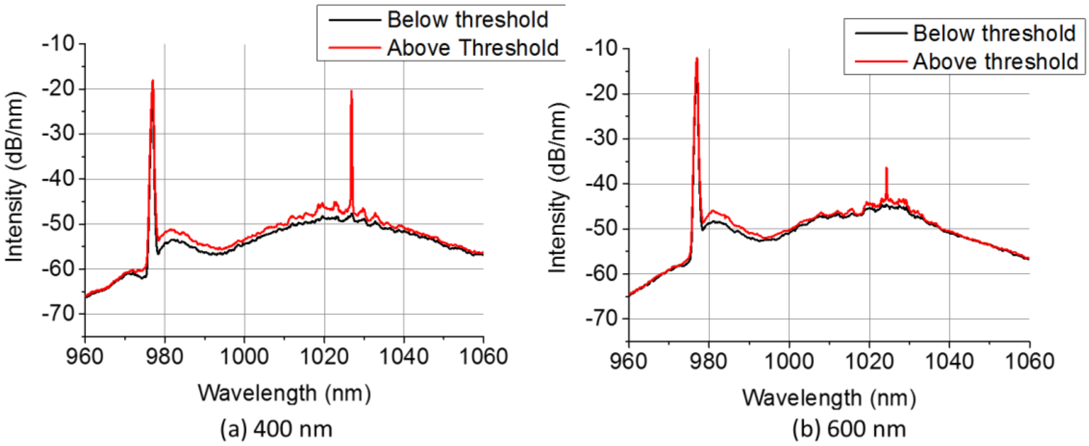

Figure 6.13 Output spectrum below and above laser threshold of waveguides containing: (a) a 400 nm wide nanowire and (b) a 600 nm wide nanowire

Since both 400 nm wide and 600 nm wide nanowires are single transverse mode waveguides, the peaks observed from output spectrum can only be different longitudinal modes but not different transverse modes. The wavelength spacing between two nearest modes, known as free spectral range (FSR), is related to the cavity length:

$$\Delta\lambda_{FSR} = \frac{\lambda^2}{2nL} \qquad Eq.6-11$$

where $\Delta\lambda_{FSR}$ is the wavelength spacing of two nearest excited modes, λ is the vacuum wavelength of light, n is the refractive index of the media within the cavity and L is the length of the cavity. The waveguide device used for this measurement has a physical length of 6.7 mm, thus the FSR related to this cavity is calculated to be 0.037 nm using Eq.6-11. This wavelength spacing, however, does not agree with the measured spacing of 4.2 nm from *Figure 6.14*. The cause of this phenomenon is unknown but there is a hypothesis for this. By adjusting the pump coupling position across the width of the 5 µm wide strip loaded input waveguide, the modes excited at the pump wavelength beating in the multimode input section, resulting in a spatial distribution of population inversion which changes as the pump mode excitation changes. Moving the pump coupling position alters the spatial overlap between the population inversion and the modes at the lasing wavelength resulting in different modes achieving threshold and a shift in wavelength. This hypothesis will be further investigated in the future.

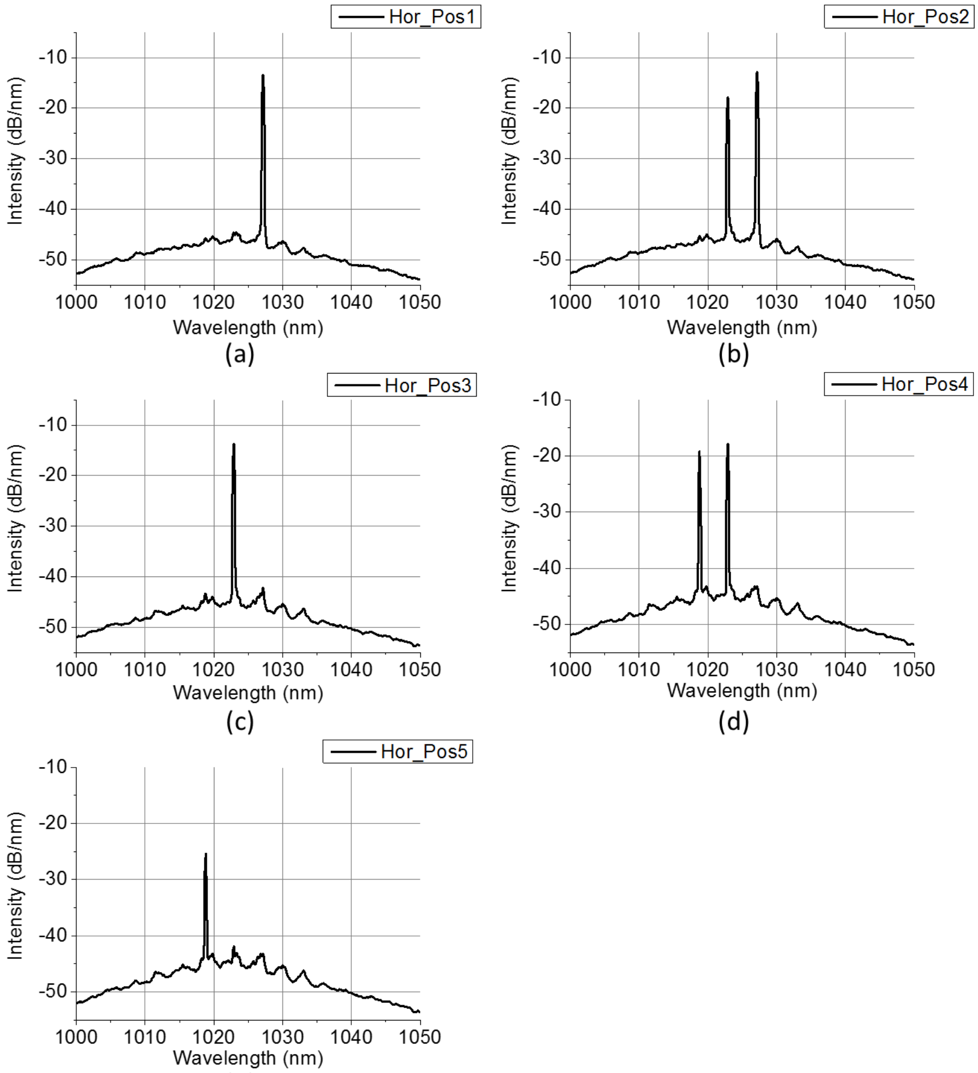

(a) (b) (c) (d) (e)

Figure 6.14 Output spectrum of the laser for different coupling position in horizontal direction (i.e. Hor_Pos1, Hor_Pos2, etc.)

6.3.6 Laser performance

The performance of a laser can be assessed by its slope efficiency and laser threshold. Because coupling loss varies for different devices and coupling methods, slope efficiency and threshold need to be calculated with respect of launched power rather than the incident pump power.

To calculate the launched power, the in-coupling loss needs to be known. The in-coupling loss and out-coupling loss are the two parts that forms the total coupling loss. The former is caused by the mode mismatch and Fresnel reflection and the latter is caused by Fresnel reflection only due to there not being a mode mismatch for a wave escaping from the waveguide into free space. Therefore, the in-coupling loss can be expressed as:

$$Loss(in-coupling) = Loss\ (coupling) - Loss(out-coupling) \qquad Eq. 6-12$$

Since the insertion loss consists of the coupling loss and propagation loss, knowing two of them can provide the third. Therefore, the total coupling loss is:

$$Loss(coupling) = Loss\ (insertion) - Loss(propagation) \qquad Eq.6-13$$

Recalling from Section 6.3.1, the insertion loss of the waveguide with a 2.5-mm-long, 400-nm-wide nanowire was found to be -21.33 dB and propagation loss of the same waveguide was -7.77 dB, yielding the total coupling loss of -13.56 dB.

As mentioned in Section 3.2.1, the Fresnel equations for reflection for s-polarization and p-polarization are:

$$R_s = \left|\frac{\mathrm{n}_1 \cos\theta_i - \mathrm{n}_2 \cos\theta_t}{\mathrm{n}_1 \cos\theta_i + \mathrm{n}_2 \cos\theta_t}\right|^2 \qquad Eq.3-2$$

$$R_p = \left|\frac{\mathrm{n}_1 \cos\theta_t - \mathrm{n}_2 \cos\theta_i}{\mathrm{n}_1 \cos\theta_t + \mathrm{n}_2 \cos\theta_i}\right|^2 \qquad Eq.3-3$$

For unpolarised, normal incident light, the Fresnel reflection is:

$$R = \left|\frac{\mathrm{n}_1 - \mathrm{n}_2}{\mathrm{n}_1 + \mathrm{n}_2}\right|^2 \qquad Eq.6-14$$

Hence, the out-coupling loss can be calculated using equation:

$$Loss(out - coupling) = 10\log_{10}(1 - R) = 10\log_{10}\left(1 - \left|\frac{\mathrm{n}_1 - \mathrm{n}_2}{\mathrm{n}_1 + \mathrm{n}_2}\right|^2\right) \qquad Eq.6-15$$

By applying the refractive index of 250W Yb:Ta$_2$O$_5$ and air to Eq.6-15, an out-coupling loss of -0.56 dB can be obtained. Therefore, the in-coupling loss of -13 dB is obtained, equalling to a coupling efficiency of 5.01%.

Figure 6.15 shows the laser output power versus incident power of the 400 nm and 600 nm strip loaded waveguides, respectively. The laser threshold and slope efficiency of the 400 nm wide strip loaded waveguide are calculated to be 10.2 mW and 43% respectively. Compared to the 400 nm strip loaded waveguide, the 600 nm wide strip loaded waveguide has a higher laser threshold of 12.3 mW, which is expected. Due to the maximum output power of the pump laser diode being 260 mW (i.e. equivalent incident power of 13.02 mW), only one data point beyond the laser threshold can be taken for the 600 nm wide strip loaded waveguide, thus the slope efficiency cannot be calculated.

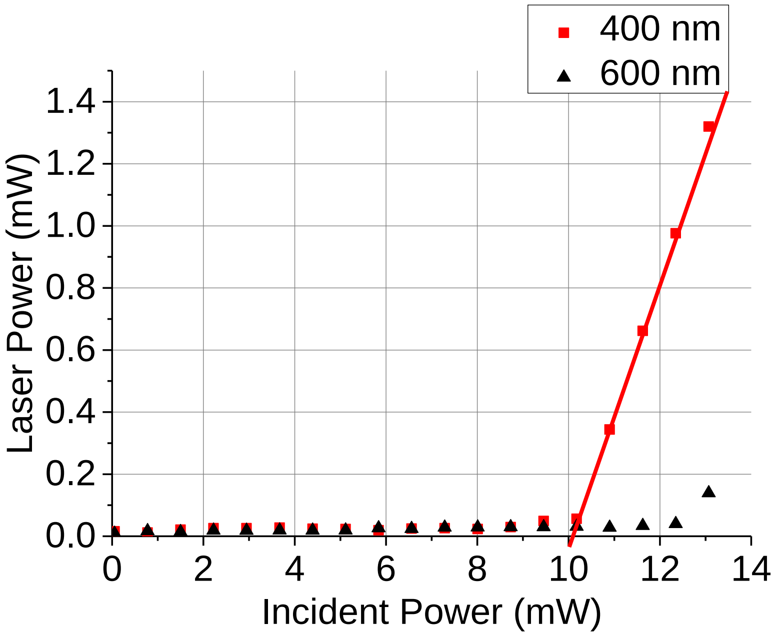

Figure 6.15 Laser output power of waveguides contain 400 nm and 600 nm nanowire with respect of incident pump power

Figure 6.16(a) and (b) plots the slope efficiency and laser threshold of the Yb doped waveguide lasers made by different materials from the literature and the work of this thesis, and their waveguide cross section area. As modifying reflectivity (i.e. attaching mirrors or using a DBR grating) can largely tune the slope efficiency as well as laser threshold, only the waveguides without any attached mirror or DBR grating will be parallel compared.

Among the listed devices with polished end facets, the Yb:YAG channel waveguide yields the highest slope efficiency of 56% yet possesses the second largest waveguide size of 530.66 μm^2[12]. Furthermore, this waveguide was fabricated by ultrafast laser inscription (ULI) which requires a sophisticated high power femtosecond laser system, resulting in high fabrication cost and limited throughput. In comparison, the Yb:Ta_2O_5 strip loaded waveguide (in this work) has a moderate slope efficiency of 38% but holds the smallest waveguide cross section area of 0.32 μm^2 at the output end among all existing Yb doped waveguide lasers.

Figure 6.16 (b) shows that the laser threshold increases with increase of the waveguide cross section area. Despite the differences in host material, doping concentration, and reflectivity of the cavity, larger cross section leads to a lower power density, hence more power is needed to achieve the population inversion.

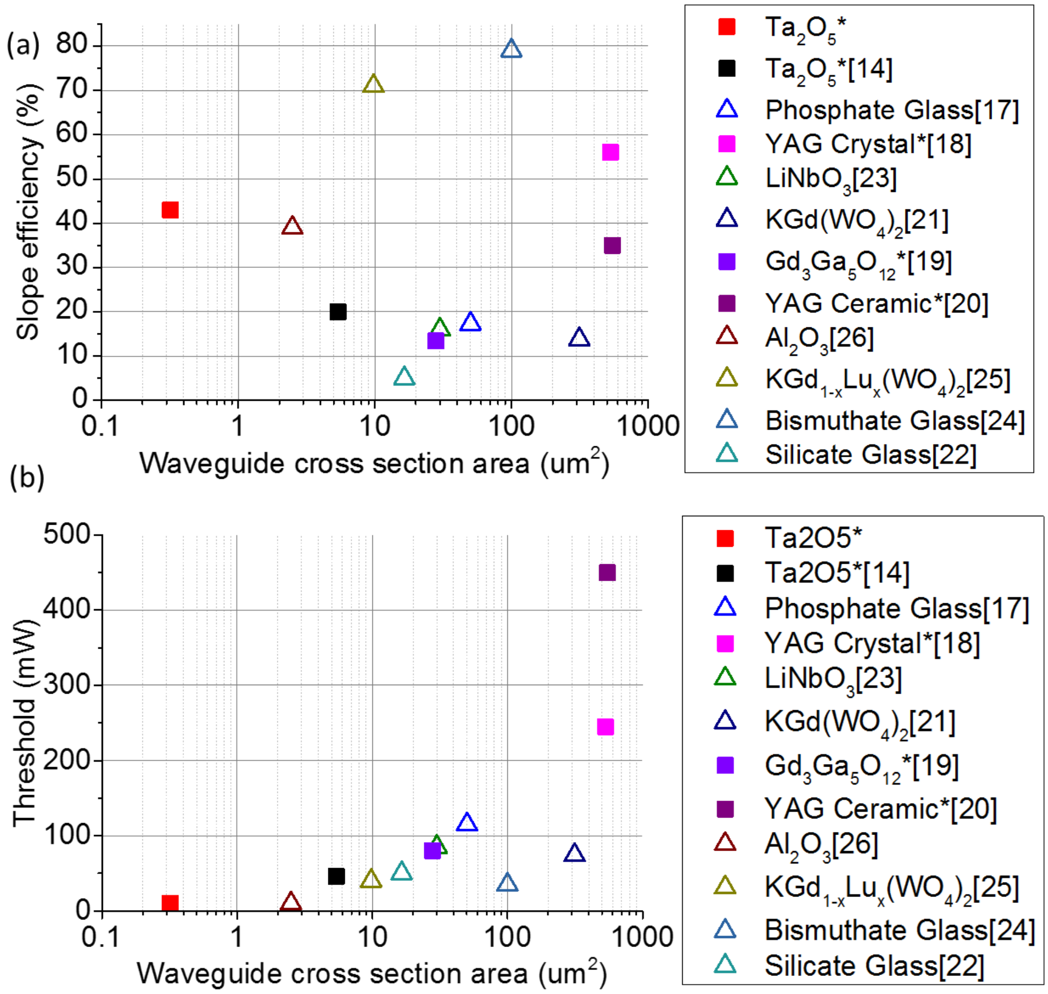

*Figure 6.16 (a) Slope efficiency versus waveguide cross section area and (b) Laser threshold versus waveguide cross section area (square in the figure and * superscript in legend represent waveguides device with polished end facet only; red square represents this work; detailed information is shown in Table 6.2)*

Table 6.3 provides the slope efficiency, threshold, mirror setting and waveguide size of different Yb doped waveguide lasers.

Table 6.3 Slope efficiency, laser threshold, waveguide (WG) forming method, reflectivity modification method and waveguide cross section size of different Yb doped waveguide lasers

Laser media	Type	Slope efficiency	Threshold (mW)	WG Forming Method	Reflectivity modification	Waveguide cross section size (μm^2)
Yb:Ta_2O_5	Strip loaded WG	38%	12	RIE-ICP	Polished end facet	0.32
Yb:Ta_2O_5 [10]	Rib WG	20%	46	IBE	Polished end facet	5.4
Yb:YAG crystal[12]	Channel WG	56%	245	ULI	Polished end facet	530.66
Yb:$Gd_3Ga_5O_{12}$[13]	Channel WG	13.4%	80	IBE	Polished end facet	28
Yb:YAG Ceramic[14]	Channel WG	35%	450	ULI	Polished end facet	550
Yb:$KGd(WO_4)_2$ [15]	Channel WG	13.8%	74	ULI	HR / 5% OC	314
Yb: silicate glass [16]	Channel WG	5%	50	Ion Exchange	HR / 5% OC	16.5
Yb:$LiNbO_3$ [17]	Channel WG	16%	85	N/A	HR / 8% OC	30
Yb: bismuthate glass [18]	Channel WG	79%	35	ULI	HR / 30% OC	100
Yb:$KGd_{1-x}Lu_x(WO_4)_2$ [19]	Channel WG	71%	40	IBE	HR / 70% OC	9.8
Yb: phosphate glass[20]	Channel WG	17.3%	115	ULI	Etched DBR	50.24
Yb:Al_2O_3[21]	Channel WG	39%	10	RIE	Etched DBR	2.5

6.4 Summary

In this chapter, the optical properties and the lasing performance of the 6.7 mm long Yb:Ta_2O_5 strip loaded nanowire waveguide were characterized.

The insertion loss of the waveguide with different nanowire widths was measured. As expected, the insertion loss increases with decrease of nanowire width. The propagation loss of the waveguide with 2.5 mm long, 400 nm wide nanowire was measured to be -7.77 dB by Fabry-Peort method.

The excited lifetime measured from the 250W Yb:Ta_2O_5 strip loaded waveguide was found to be 60 µs, which is shorter than published results from literature. This is due to the presence of strong blue cooperative emission that depopulates the excited states.

Laser action was observed from both the 400 nm wide and 600 nm wide strip loaded waveguide samples. They all have a nanowire length of 2.5 mm. The slope efficiency measured from the 400 nm wide strip loaded waveguide sample was found to be 38%, with respect to the launched power. The launched power threshold for this waveguide laser was found to be 12 mW. The laser threshold of the 600 nm strip loaded waveguide was found to be 14.5 mW, which is expected to be higher than it of the narrower waveguide since the power density inside the waveguide is lower compared to it inside of a smaller waveguide. The slope efficiency of the 600 nm wide strip loaded waveguide was not measurable due to the limitation of maximum output power of the pump diode which leading to insufficient data points beyond threshold. With higher pump level, waveguides with wider nanowires are expected to lase.

Apart from the main lasing peak of the 400 nm strip loaded waveguide, there are also other small peaks appearing around the lasing peaks. These peaks can be excited to lase under certain coupling conditions. However, the wavelength separation of those peaks is 4.2 nm, which is not correspond with the peak separation associated with the length of the waveguide (0.037 nm). The cause of this phenomenon will be investigate in the future.

Bibliography

[1] R. G. Hunsperger, Integrated Optics: Theory and Technology, Springer (2009)

[2] T. Feuchter *et al.*, "*High precision planar waveguide propagation loss measurement technique using a Fabry-Perot cavity*", IEEE Photonics Technology Letters, Vol. **6**, Issue 10 (1994)

[3] Y. Lin *et al.*, “*Self-phase modulation in highly confined submicron Ta_2O_5 channel waveguides*”, Optics Express, Vol. 24, No. 19 (2016)

[4] R. Y. Chen *et al.*, “*Broadband stimulated four-wave parametric conversion on a tantalum pentoxide photonic chip*”, Optics Express, Vol. 19, No. 27 (2011)

[5] A Brenier, “*A new evaluation of Yb^{3+}-doped crystals for laser applications*”, Journal of Luminescence, **92**, 3, 199-204(2001)

[6] J. Kong *et al., “9.2-W diode–end–pumped Yb:Y_2O_3 ceramic laser*”, Applied Physics Letters **86**, 161116 (2005)

[7] Y. Lin *et al.*, “*Self-phase modulation in highly confined submicron Ta_2O_5 channel waveguides*”, Optics Express, Vol. 24, No. 19 (2016)

[8] R. Y. Chen *et al.*, “*Broadband stimulated four-wave parametric conversion on a tantalum pentoxide photonic chip*”, Optics Express, Vol. 19, No. 27 (2011)

[9] C. Wu *et al.*,” *Four-wave-mixing in the loss low submicrometer Ta_2O_5 channel waveguide*”, Optics Letters, Vol. 40, No. 19 (2015)

[10] A. Aghajani *et al.* , "*Waveguide lasers in ytterbium-doped tantalum pentoxide on silicon*," Opt. Lett. **40**, 2549-2552 (2015)

[11] Z. Burshtein, “*Radiative, nonradiative, and mixed-decay transitions of rare-earth ions in dielectric media*”, Opt. Eng. **49**(9), 091005 (2010)

[12] J. Siebenmorgen *et al.,* "*Highly efficient Yb:YAG channel waveguide laser written with a femtosecond-laser*," Opt. Express **18**, 16035-16041 (2010)

[13] M. Shimokozono *et al., “Room-temperature operation of an Yb-doped $Gd_3Ga_5O_{12}$ buried channel waveguide laser at 1.025 µm wavelength*”, Appl. Phys. Lett. **68**, 2177 (1996)

[14] T. Calmano *et al., “Characterization of an Yb:YAG ceramic waveguide laser, fabricated by the direct femtosecond-laser writing technique*”, Appl Phys B **103**: 1–4 (2011)

[15] F.M. Bain *et al.*, "*Ultrafast laser inscribed Yb:KGd(WO_4)$_2$ and Yb:KY(WO_4)$_2$ channel waveguide lasers,*" Opt. Express **17**, 22417-22422 (2009)

[16] C. Florea *et al.*, “*Ytterbium-Doped Glass Waveguide Laser Fabricated by Ion Exchange*”, Journal of Lightwave Technology, Vol. 17, No. 9, 1593 (1999)

[17] J. K. Jones *et al.*, "*Channel waveguide laser at 1 µm in Yb-indiffused* $LiNbO_3$," Opt. Lett. **20**, 1477-1479 (1995)

[18] R. Mary *et al.*, "*Compact, highly efficient ytterbium doped bismuthate glass waveguide laser*," Opt. Lett. 37, 1691-1693 (2012)

[19] Dimitri Geskus *et al.*, "*High-power, broadly tunable, and low-quantum-defect* $KGd_{1-x}Lu_x(WO_4)_2$:Yb^{3+} *channel waveguide lasers*," Opt. Express 18, 26107-26112 (2010)

[20] M. Ams *et al.,"Monolithic 100 mW Yb waveguide laser fabricated using the femtosecond-laser direct-write technique*," Opt. Lett. 34, 247-249 (2009)

[21] E. H. Bernhardi *et al.*, "*Highly efficient, low-threshold monolithic distributed-Bragg-reflector channel waveguide laser in* Al_2O_3:Yb_{3+}", Opt. Lett. **36**, 603-605 (2011)

Chapter 7: Conclusion and Future Works

7.1 Conclusion

In this thesis, the working principle of lasers together with the theory of up/down-conversion of solid state lasers was introduced. Properties of different active ions and host materials were studied.

The loss mechanisms of the waveguide were discussed. Following the discussion, a low loss waveguide design, containing nanowire, taper and coupler section, was developed to minimize the mode mismatching. Strip loaded waveguide, SiO_2 based buried channel waveguide and polymer based waveguide were proposed. Mode simulations were performed according to the geometries of the three different types of waveguide using Lumerical FDTD. All three types of waveguide provide good confinement in doped area (> 70%) at narrowest nanowire width. The spot size of the strip loaded waveguide decreases with the decrease of the nanowire width down to 0.7 µm and starts to increase again. This is because the mode is more likely to propagate in the planar layer where there is lack of horizontal confinement. Different from the strip loaded waveguide, the mode spot size of both buried channel waveguides decrease with the narrowing of nanowire. The power confined in the doped area for all three waveguides was calculated. The mode confinement of both the polymer based and SiO_2 based buried channel waveguide drops with decreasing of nanowire width and bottomed at 73% and 74%, respectively. The strip loaded waveguide, however, shows the opposite behaviour and has its peak confinement of 77% at 0.4 µm nanowire width.

Gain simulation of Yb doped nanowire was carried out by Simphosoft which has both rate equation modelling and FDTD modelling embedded. The simulation results show that the maximum gain of the Yb:Ta_2O_5 nanowire at Yb concentration of 1.5 at.% is 17.41 dB/cm under 100 mW pumping.

The fabrication processes of Si based strip loaded, SiO_2 based buried channel and polymer based buried channel waveguides were presented. The strip loaded waveguide was finished as desired with a Ta_2O_5 layer etched through, forming strips with an 89° side wall angle. The film thickness was found to be slightly less than the designed value but does not cause any significant problems in terms of mode confinement. The SiO_2 based buried channel waveguide utilized a new ICP etching recipe which provides a 88° side wall angle and 5.3 selectivity as the existing etching recipe was extremely inefficient to etch the Yb:Ta_2O_5 layer. The recipe was developed by tuning the etching parameters (RF power, ICP power, process gas ratio and chamber pressure). The deposition and etching processes resulted in a 387 nm thick channel waveguide with 87° side wall angle. The polymer based buried channel waveguide was fabricated in collaboration with VTT Finland. Due to the natural defects of the sputtering process, the deposited channel waveguide has a reduced thickness and was not in rectangular shape. The narrowest nanowire that can guide Yb emission is 600 nm. This issue can be improved by improving the stamp quality or applying undercut structure.

The characterization of Yb:Ta_2O_5 thin film properties is demonstrated. The refractive index of the film decreases with the increase of the Yb deposition power. The Yb concentration measured by XPS shows that the Yb concentration is linear correlated to the Yb deposition power, proving the availability of precise control of doping concentration. The best concentration of Yb dopants is determined by measuring the photoluminescence of samples with different concentrations. Among all the samples, the 250W sample (equivalent to 1.25 at.%) showed the highest photoluminescence intensity and is therefore nominated to be used as the gain material of the waveguides. The planar waveguide loss of 250W Yb:Ta_2O_5 film is measured to be 0.96 dB/cm before annealing and 0.2 dB/cm after annealing.

After the characterization of Yb:Ta_2O_5 thin films, a series of 6.7 mm long Yb:Ta_2O_5 strip loaded nanowire waveguides are measured. During the measurement, a cooperative emission induced blue emission was observed, which resulted in the reduction of the excited state lifetime to 60 µs. Lasing was observed in waveguides that have a nanowire length of 2.5 mm and width of 400 nm and 600 nm with bare polished end facets. The waveguides have nanowires wider than 600 nm are also expected to lase with higher pumping levels. The slope efficiency and launched power threshold of the 400 nm wide waveguide are 38% and 12 mW, respectively. Due to the high coupling loss and short in pump power, there is not sufficient data obtained beyond the laser threshold (14.5 mW) for the waveguide with 600 nm wide nanowire. Therefore, the slope efficiency of this waveguide could not be calculated. Beside the main lasing peak, there are also other small peaks that can be excited to lase under certain coupling conditions. However, the wavelength separation is not corresponding to the length of the waveguide. The cause of this phenomenon is unknown at the moment and will be investigated in the future.

The work presented in this thesis focuses on the demonstration of a nanowire waveguide laser in Yb:Ta_2O_5, building a foundation for realizing complex optical devices for integrated optical circuits. This work also made an effort towards establishing new depositing technique for doped amorphous material with on-site doping control for both electrical and photonic applications and new waveguide fabrication processes for materials that are hard to pattern.

7.2 Future works

7.2.1 Strip loaded waveguide device

In Chapter 6, the laser action of an Yb:Ta_2O_5 strip loaded waveguide was demonstrated. The laser cavity was formed by the end facets of the waveguide, which means the reflection from both the pump and emission are caused by Fresnel reflection. Recalling the Fresnel reflection equation (Eq 4-4 and Eq 4-5), for normal incidence, the reflection can be given as:

$$R = \left|\frac{n_1 - n_2}{n_1 + n_2}\right|^2 \qquad Eq. 7-1$$

where n_1 and n_2 are the refractive indices of the two different mediums that the light passes through. By taking the refractive indices of air and the Yb:Ta_2O_5 into Eq. 7-1, the reflection of each end facet has been calculated as 12.6%, meaning 87.4% of the pump and emission is coupled out from the waveguide at the end facets. The reflectivity of the end facet of the waveguide can affect the threshold and the output of the laser. On one hand, the low reflectivity of the end facet helps the laser output escape from the device, lifting up the slope efficiency. On the other hand, it also raises the threshold of lasing since the pump is not utilized fully. Therefore, modifying the reflectivity of the end facet can effectively tune the laser threshold and slope efficiency.

7.2.1.1 External mirror attaching

The most common solution for modifying end facet reflectivity of a waveguide laser is to attach an external mirror with different reflective properties on each waveguide end facet (as shown in Figure 7.1). There are three proposed mirrors: high reflective (HR) mirror (reflectivity greater than 99%), 10% output coupler (OC) and 5% output coupler (OC). All the reflection mirrors are targeting the lasing wavelength of the Yb:Ta_2O_5 waveguide laser. Using these mirrors, three different mirror configurations can be made: HR and bare polished end facet; HR and 10% OC; and HR and 10% OC.

The mirrors will be attached to the end facets of the waveguide using an electronic liquid called Fluorinert FC-70. It is a clear and colourless liquid with thermal resistance up to 215°C, which can provide effective adhesion between the mirror and the waveguide. After mounting the mirror, the waveguide device will be tested for its lasing properties using the same method and setup as explained in Section 5.6.

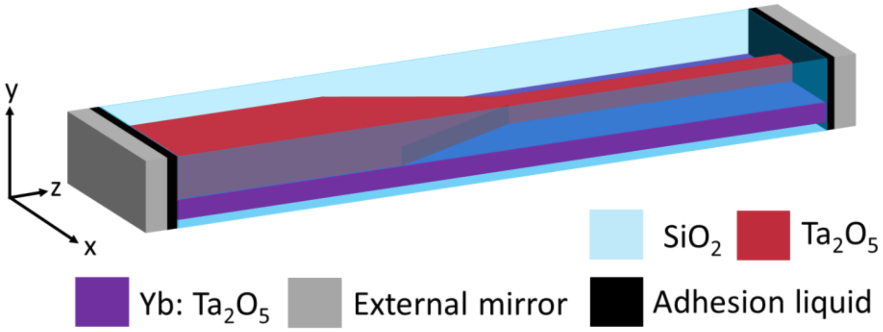

Figure 7.1 Schematic of waveguide with attached external end facet mirrors

7.2.1.2 Dielectric mirror deposition

Using a dielectric mirror is another solution for modifying the end facet reflectivity. Figure 7.2 (a) and (b) illustrate the schematic of the waveguide with a dielectric mirror deposited on end facet, and the structure of the dielectric mirror respectively. Unlike the commercial external mirror that normally modifies one wavelength range (unless you order a customized product like a single band filter), the in-house made dielectric mirror offers more flexibility. Instead of having 5% OC at lasing wavelength only, the mirror can be made to have 5% OC at the lasing wavelength and over 99% reflectivity at pumping the wavelength. However, the only drawback of the dielectric mirror is that once it is deposited on the end facet, it can no longer be removed. On the other hand, the deposited dielectric mirror has a much stronger adhesion than the attached external mirror and thus makes handling of the chip easier and extends the maximum value of pump power that the waveguide can take before the adhesive liquid that holds the external mirror attached is evaporated.

There are two types of dielectric mirrors proposed: an input mirror that reflects over 99% of the Yb emission wavelength (i.e. from 1000 nm to 1100 nm), and an output mirror that reflects over 99% at pumping wavelength (i.e. from 970 nm to 985 nm) and partially reflects (5% to 20% depending on the results of external mirror measurement) the Yb emission wavelength.

The mirror consists of two different kinds of materials, pure Ta_2O_5 and SiO_2. The deposition will take place in Leybold Helios using exactly the same process that was used for the waveguide demonstrated in Section 5.3.2 and 5.3.6.

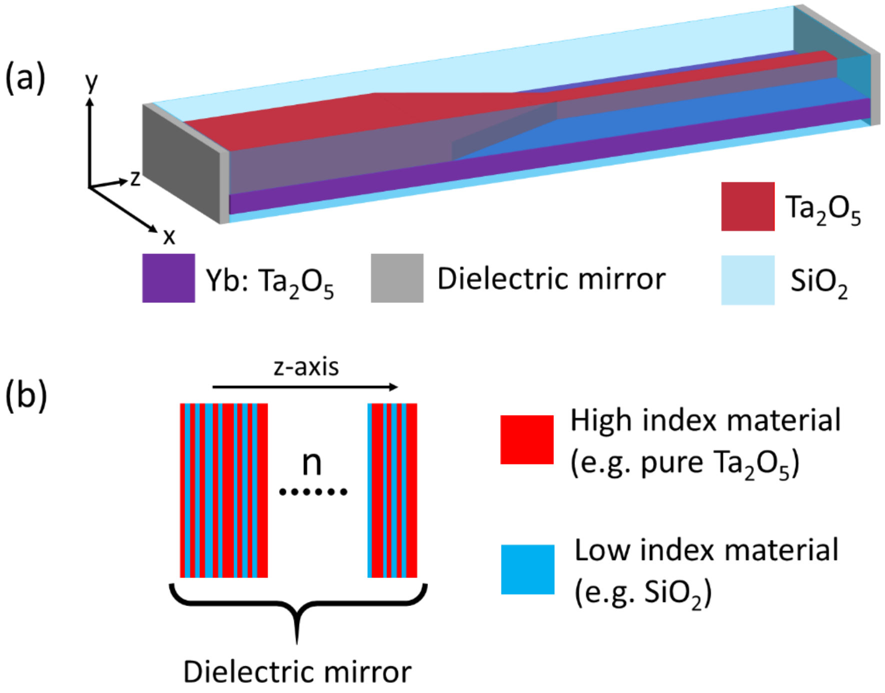

Figure 7.2 Schematic of (a) waveguide with deposited dielectric end facet mirror and (b) dielectric mirror structure

7.2.1.3 Distributed Bragg reflector (DBR)

Apart from attaching commercial mirrors or depositing dielectric mirrors at the end facets of the waveguide, distributed Bragg reflectors (DBR) that fabricated into the waveguide during the waveguide etching process can as well help with modifying the reflectivity. The advantage of the DBR is the possibility of mass production since the external mirror attachment can only be done on one chip at a time and the dielectric mirror deposition introduce an extra step to the fabrication process.

Figure 7.3 (a) and (b) shows the schematic of the waveguide device with DBR etched at both ends and the refractive index profile of the waveguide along the z direction, respectively.

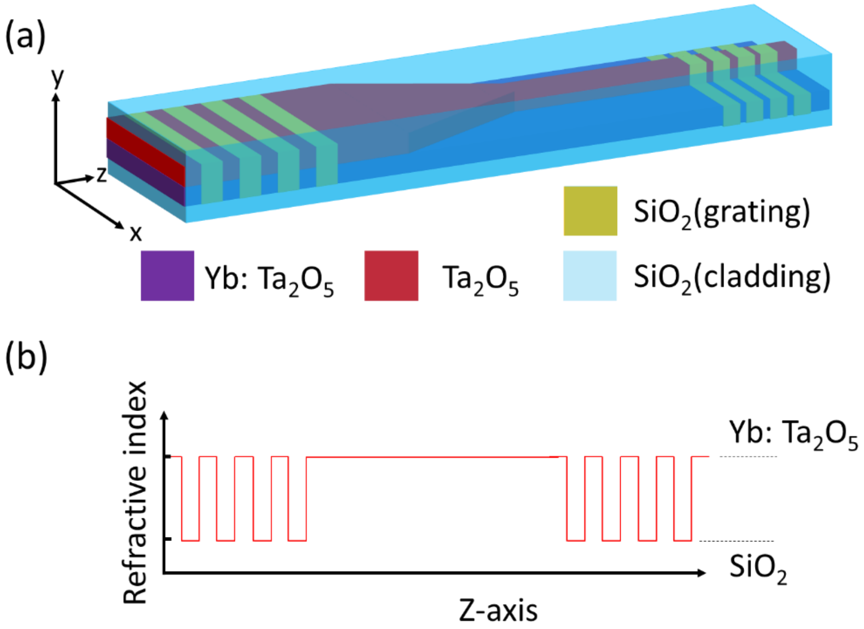

Figure 7.3 Schematic of (a) waveguide with DBR etched into it and (b) refractive index profile of the waveguide along the Z axis

7.2.2 **Buried channel waveguide device**

Due to the breakdown of the sputterer, the buried channel waveguide cannot be finished. Hence, the future work for this kind of waveguide device would be finishing the fabrication when the machine is back online, measuring the optical properties and comparing the results with the strip loaded waveguide device.

The laser performance after adding different kinds of mirrors (external mirror, dielectric mirror and DBR) also needs to be investigated.

7.2.3 **Polymer based buried channel waveguide device**

The polymer based buried waveguide device will be measured using the methods introduced in Chapter 6 for its loss and laser performance. Mirrors will be added after the monolithic waveguide has been tested and the performance will be assessed and be compared with the monolithic waveguide.

Appendix A Dieke Diagram for Rare Earth Ions

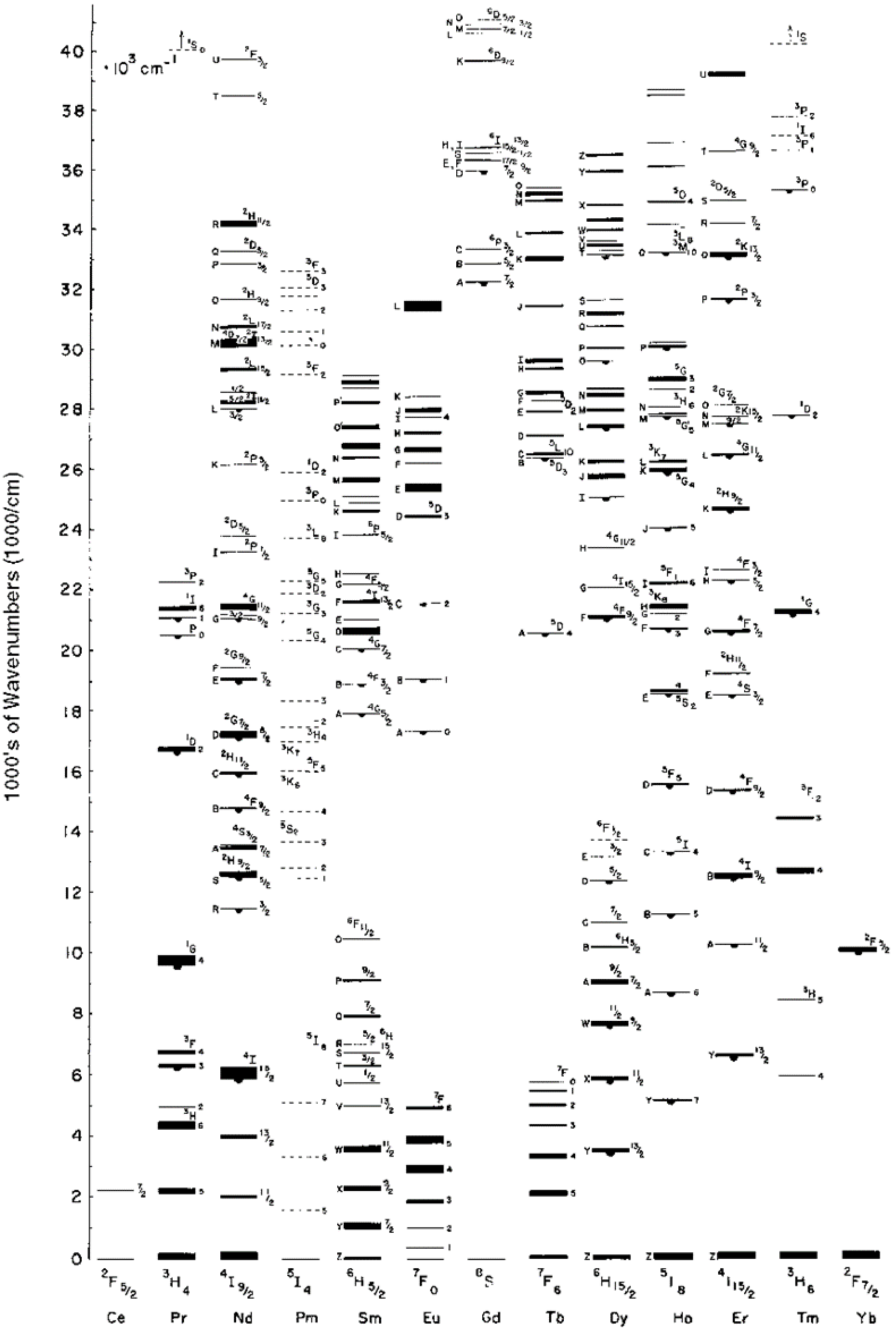

G. H. Dieke. Spectra and energy levels of rare earth ions in crystals
(Interscience Publishers. New York. 1968)

Figure A.1 Dieke Diagram for Rare Earth Ions

Appendix B Sputtering machine conditioning

Since the sputterer is shared with users who deposits thick metal films, there can be metal particle contamination during deposition that leads to degradation of the device performance. Therefore, deep clean and conditioning are extremely critical before depositing the functional layer of the laser device. The cleaning procedure includes several steps: firstly, detachable chamber shields and uniformity masks need to be blasted with fine virgin Al_2O_3 beads to remove all previous deposited residuals. Then the shield surface needs to be finished with coarse Al_2O_3 beads in order to enhance adhesion so that the excess sputtered material will stick on the shield rather than floating around in the chamber. After bead blasting, the shields and masks need to be dipped into an ultrasonic tank with de-ionized (DI) water in order to strip off the Al_2O_3 beads which are stuck on them. Before reinstalling the shields and masks into the machine, they need to be put in a dust free environment for drying up and then need to be washed with isopropanol alcohol (IPA). After the cleaning process is complete, the sputterer needs to be conditioned before performing deposition of the device. The conditioning loop consists of heating up the chamber and purging with Ar gas in order to get rid of water vapour trapped inside the shields. A thin film of Ta_2O_5 is then deposited to suppress any possible remaining Al_2O_3 beads.

The $Yb:Ta_2O_5$ thin film was checked by a Tencor surface scanner and Metricon (prism coupler) after each conditioning loop to determine the deposition quality. The Tencor surface scanner uses a laser to scan the surface of the wafer and counts the scattering that occurs from the top surface of the wafer. The scattering can originate from deposition defects and/or particle contamination. Metricon was used in order to visually check the defects.

Figure B.1 shows the results of the surface scanning and pictures of laser propagation trace in the films at different stages of the conditioning procedure. Figure B.1 (a) displays surface scanning data prior to the conditioning process. The scattering count exceeded the maximum number that can be stored in the system, thus only one-third of the wafer was scanned. The propagation trace in Figure B.1 (a) helps to visually confirm the massive amount of scattering that occurs in the film. Figure B.1 (b) and (c) illustrates the scanning results and propagation traces for the 14th conditioning loop and 29th conditioning loop, respectively. Both the surface results and the laser propagation traces show that with the progressing numbers of conditioning cycles, scattering was significantly reduced.

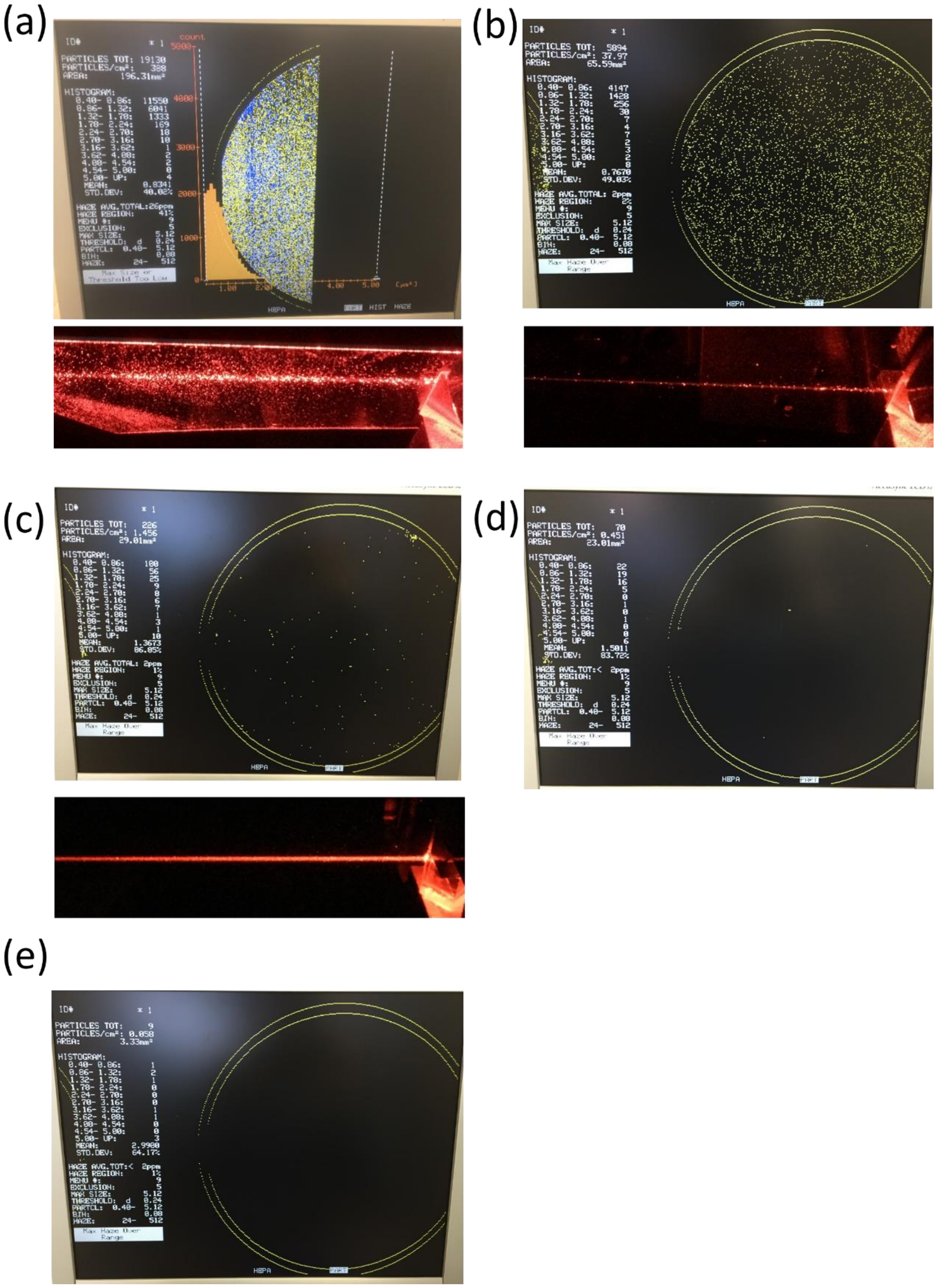

```
ID#                *1

PARTICLES TOT:  19130
PARTICLES/cm²:    388
AREA:        196.31mm²

HISTOGRAM:
  0.40- 0.86:   11550
  0.86- 1.32:    6041
  1.32- 1.78:    1333
  1.78- 2.24:     169
  2.24- 2.70:      18
  2.70- 3.16:      10
  3.16- 3.62:       1
  3.62- 4.08:       2
  4.08- 4.54:       2
  4.54- 5.00:       0
  5.00- UP:         4
  MEAN:        0.8341
  STD.DEV:     40.02%

HAZE AVG.TOTAL:26ppm
HAZE REGION:      41%
MENU #:             9
EXCLUSION:          5
MAX SIZE:        5.12
THRESHOLD:  d    0.24
PARTCL:  0.40-   5.12
BIN:             0.08
HAZE:       24-   512
   Max Size or
Threshold Too Low
```

```
ID#               *1

PARTICLES TOT:   5894
PARTICLES/cm²:  37.97
AREA:         65.59mm²

HISTOGRAM:
  0.40- 0.86:    4147
  0.86- 1.32:    1428
  1.32- 1.78:     256
  1.78- 2.24:      30
  2.24- 2.70:       7
  2.70- 3.16:       4
  3.16- 3.62:       7
  3.62- 4.08:       2
  4.08- 4.54:       3
  4.54- 5.00:       2
  5.00- UP:         8
  MEAN:        0.7670
  STD.DEV:     49.03%

HAZE AVG.TOTAL: 2ppm
HAZE REGION:       2%
MENU #:             9
EXCLUSION:          5
MAX SIZE:        5.12
THRESHOLD:  d    0.24
PARTCL:  0.40-   5.12
BIN:             0.08
HAZE:       24-   512
 Max Haze Over
     Range
```

```
ID#               *1

PARTICLES TOT:    226
PARTICLES/cm²:  1.456
AREA:         29.01mm²

HISTOGRAM:
  0.40- 0.86:     100
  0.86- 1.32:      56
  1.32- 1.78:      25
  1.78- 2.24:       9
  2.24- 2.70:       8
  2.70- 3.16:       6
  3.16- 3.62:       7
  3.62- 4.08:       1
  4.08- 4.54:       3
  4.54- 5.00:       1
  5.00- UP:        10
  MEAN:        1.3673
  STD.DEV:     86.85%

HAZE AVG.TOTAL: 2ppm
HAZE REGION:       1%
MENU #:             9
EXCLUSION:          5
MAK SIZE:        5.12
THRESHOLD:  d    0.24
PARTCL:  0.40-   5.12
BIN:             0.08
HAZE:       24-   512
 Max Haze Over
     Range
```

```
ID#               *1

PARTICLES TOT:     70
PARTICLES/cm²:  0.451
AREA:         23.01mm²

HISTOGRAM:
  0.40- 0.86:      22
  0.86- 1.32:      19
  1.32- 1.78:      16
  1.78- 2.24:       5
  2.24- 2.70:       0
  2.70- 3.16:       1
  3.16- 3.62:       0
  3.62- 4.08:       1
  4.08- 4.54:       0
  4.54- 5.00:       0
  5.00- UP:         6
  MEAN:        1.5011
  STD.DEV:     83.72%

HAZE AVG.TOT:<  2ppm
HAZE REGION:       1%
MENU #:             9
EXCLUSION:          5
MAX SIZE:        5.12
THRESHOLD:  d    0.24
PARTCL:  0.40-   5.12
BIN:             0.08
HAZE:       24-   512
 Max Haze Over
     Range
```

```
ID#               *1

PARTICLES TOT:      9
PARTICLES/cm²:  0.058
AREA:          3.33mm²

HISTOGRAM:
  0.40- 0.86:       1
  0.86- 1.32:       2
  1.32- 1.78:       1
  1.78- 2.24:       0
  2.24- 2.70:       0
  2.70- 3.16:       0
  3.16- 3.62:       1
  3.62- 4.08:       1
  4.08- 4.54:       0
  4.54- 5.00:       0
  5.00- UP:         3
  MEAN:        2.9980
  STD.DEV:     64.17%

HAZE AVG.TOT:<  2ppm
HAZE REGION:       1%
MENU #:             9
EXCLUSION:          5
MAX SIZE:        5.12
THRESHOLD:  d    0.24
PARTCL:  0.40-   5.12
BIN:             0.08
HAZE:       24-   512
 Max Haze Over
     Range
```

Figure B.1 *Surface scan and Metricon results of: (a) 400 nm* *Ta_2O_5* *film deposited before conditioning, (b) 400 nm* *Ta_2O_5* *film deposited after 14 loops (c) 400 nm* *Ta_2O_5* *film deposited after 29 loops, (d) 2 µm thermally grown* *SiO_2* *and (e) foundry made virgin Silicon wafer.*

Table B.1 shows the particle size dependent scattering counts for all five wafers shown in *Figure B.1*. With 29 loops of conditioning process, the scattering counts between 0.4 and 0.86 μm^2 can be reduced to the minimum value of 100. It can be seen that the conditioning process helped reduce scattering counts by more than 300 times, ensuring the best quality for optical guiding.

*Table B.1 Scattering counts for different particle sizes of different samples (*estimated by assuming a uniform scattering distribution across the whole wafer)*

Size of scattering (μm^2)	**(a)**	**(b)**	**(c)**	**(d)**	**(e)**
0.40 – 0.86	*34650**	*4147*	*100*	*22*	*1*
0.85 – 1.32	*18123**	*1428*	*56*	*19*	*2*
1.32 – 1.78	*3999**	*256*	*25*	*16*	*1*

Appendix C Operation of OMS in Helios Pro XL

In Helios, the deposition thickness can be controlled by using an optical monitoring system (OMS). The principle of the OMS is based on thin film interference. Light waves that are reflected by the upper and lower boundaries of the thin film interfere with each other. The interference either enhances or reduces the measured reflected light depending on the optical path difference (OPD) between the two reflected light waves.

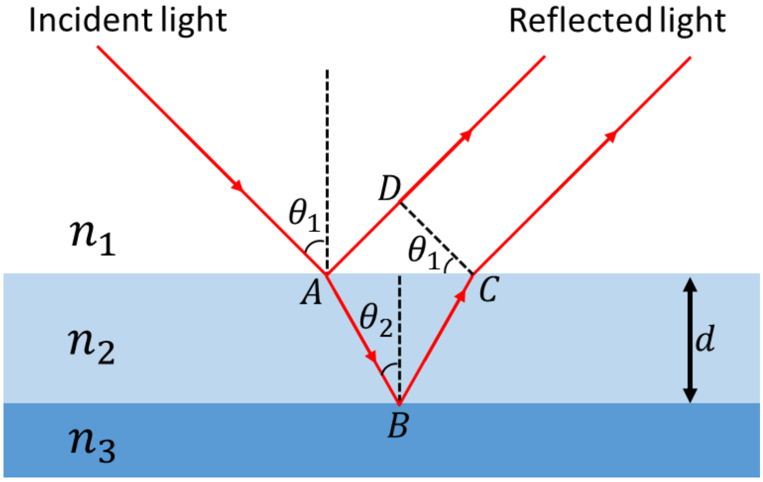

Figure C.1 Schematic of optical path difference (OPD) for light reflected from the upper and lower boundaries of the thin film

The light waves that are reflected by a thin film are shown in *Figure C.*1. The OPD is given by:

$$OPD = L_{path2} - L_{path1} \qquad Eq.C-1$$

where L_{path1} and L_{path2} are the optical path of two reflected waves, which can be expressed as:

$$L_{path1} = n_1\overline{AD} = n_1 2d\tan\theta_2\sin\theta_1 \qquad Eq.C-2$$

$$L_{path2} = n_2\left(\overline{AB}+\overline{BC}\right) = n_2\left(\frac{2d}{\cos\theta_2}\right) \qquad Eq.C-3$$

Applying Snell's law, $n_1\sin\theta_1 = n_2\sin\theta_2$, the optical path difference can be re-written as:

$$OPD = n_2\left(\frac{2d}{\cos\theta_2}\right) - 2d\tan\theta_2\, n_2\sin\theta_2 = 2n_2 d\cos\theta_2 \qquad Eq.C-4$$

During the OMS measurement, the incident light is perpendicular to the thin film surface, i.e. $\theta_2 = 0$. Hence the OPD is:

$$OPD = 2n_2 d \cos 0 = 2n_2 d \qquad Eq.C-5$$

The interference is constructive if the OPD equals to integer multiples of the light wavelength, as both reflected waves would be in phase, as expressed in the following equation:

$$2n_2 d = m\lambda \qquad Eq.C-6$$

The interference is destructive if the OPD equals to integer multiples minus half of the light wavelength due to the 180° phase shift between the two reflected waves. The relationship between film thickness and incident light wavelength in air is given by:

$$2n_2 d = \left(m - \frac{1}{2}\right)\lambda \qquad Eq.C-7$$

The intensity change with respect of thin film thickness can be plotted as shown in *Figure C.2*. Therefore, by counting the number of maximum and minimum intensity points (i.e. turning points of the measured intensity) the thickness of the thin film can be determined.

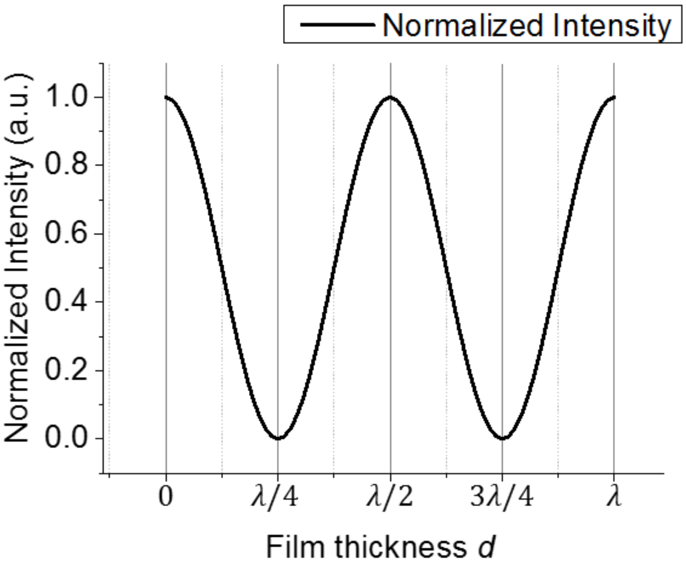

Figure C.2 Normalized reflected light intensity versus thin film thickness

The number of turning points k for the stop condition can be calculated by using the equation:

$$k = \frac{4nd}{\lambda} \qquad Eq.\mathrm{C}-8$$

where n is the refractive index of the deposited material measured at wavelength λ, and d is the desired film thickness.

Appendix D Different Types of Dicing Blades

The Loadpoint Microace 3 dicing saw uses two kinds of blades: resin or hubbed blade. *Figure D.1* (a) shows the picture of the resin blade. The resin blade is usually used for cutting glass substrates and certain hard materials. It has a thick and rough blade that creates a 500 µm wide cutting line with a rough finish. The hubbed blade shown in *Figure D.1* (b) is used to dice Si substrates and softer materials. It has a much finer blade (~40 µm blade thickness) that can provide a relatively smoother facet with only 50 µm cutting line. Therefore, the hubbed blade can minimize the damage at the cutting edge of each chip and leave enough margin if the chip needs a deep polishing.

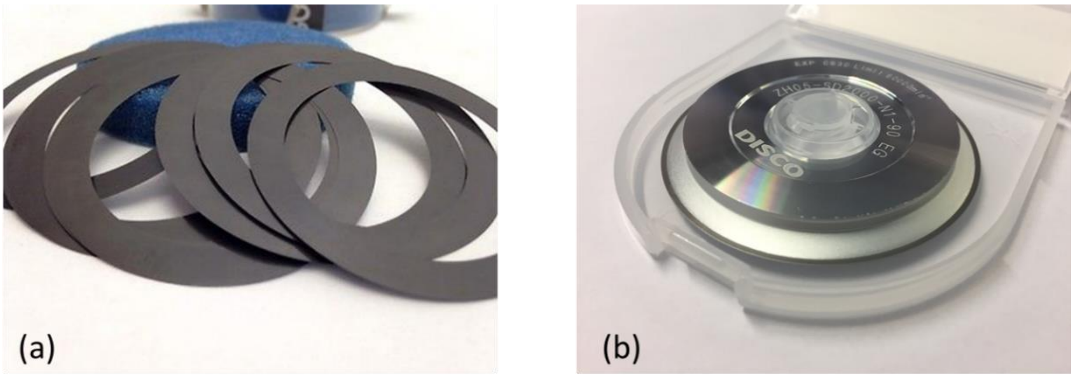

Figure D.1 Photos of (a) Resin blade and (b) Hubbed blade

During the dicing process, the blade was accelerated to 3000 rpm which results in the off-cut particles to rotate at a very high speed. Part of these particles hit the protective shield that covers the top and the side of the blade (shown in *Figure D.2*), and the rest of the particles will bombard the sample surface. Although the actual waveguide structure has been buried into, and is protected by, the SiO_2 top cladding, it still is better to have a layer of photoresist on top for extra protection.

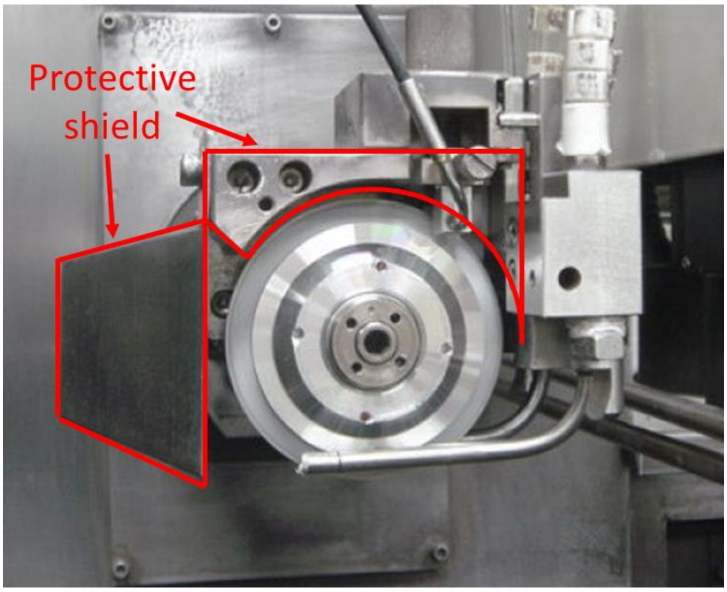

Figure D.2 Photo of dicing blade assembly

Appendix E Yb Rate Equation Derivation

The Yb^{3+} ion has an energy diagram containing only two energy levels $^2F_{5/2}$ and $^2F_{7/2}$. These levels can be called manifolds as each of them can be split into several sub-levels known as Stark level. Due to there being no reference for the energy of each Stark level for Yb^{3+} in the Ta_2O_5 host, only a schematic diagram showing the detailed energy levels of Yb^{3+} ion is presented in *Figure E.1*. The $^2F_{7/2}$ manifold contains four Stark levels, from a to d, and the $^2F_{5/2}$ manifold contains three Stark levels, from e to g. This energy diagram can be used for precise rate equation modelling if the transition parameters are known.

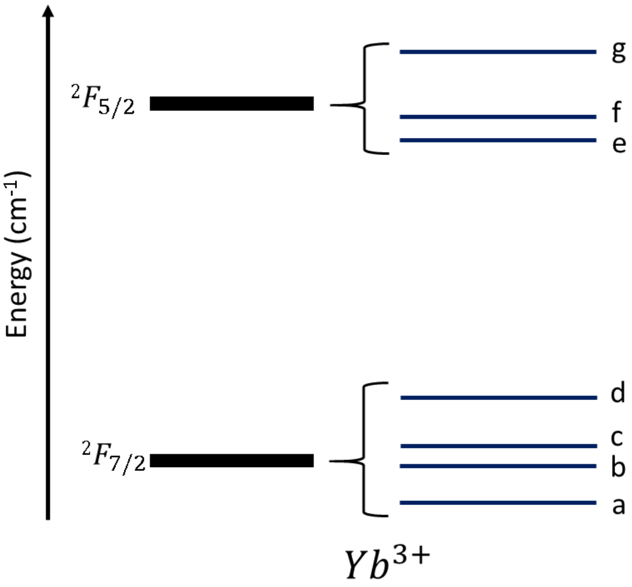

Figure E.1 Detailed energy diagram of Yb^{3+}

The dynamics of populations of different energy levels in the laser gain medium can be modelled using the rate equations. These equations are a series of differential equations that describe the temporal evolution of the energy level population under the influence of transitions between energy levels. The rate equations can be used as a part of a comprehensive model for simulating the operation of a laser gain medium.

As mentioned in Chapter 2, the Yb^{3+} has a quasi-three-level system. The lower laser level (level 1) and ground level (level 0) are quite close to each other (i.e. ~500 cm^{-1}). Because of this the two levels are so close together, that the lower laser level will be depopulated quite fast by phonon relaxation, making the population inversion easy to achieve. On the other hand, at high temperature, the small energy difference between these levels allows the lower laser level to be populated due to thermally induced transitions. Therefore, results in reabsorption of the laser signal by the states at lower laser level. However, in waveguide designs, the length of the waveguide is too short for the reabsorption to have a significant effect. Hence, having those levels close together is more beneficial than harmful for the waveguide design.

To simplify the rate equation modelling, only three levels out of seven levels will be consider in the model. *Figure E.2* gives the structure of the three-level system and the transitions between each level that Yb^{3+} has. The green lines are the absorption transitions that occur in the system. The dashed and solid red lines are the spontaneous and stimulated emissions of the system, respectively. The grey dashed lines are the non-radiative decay.

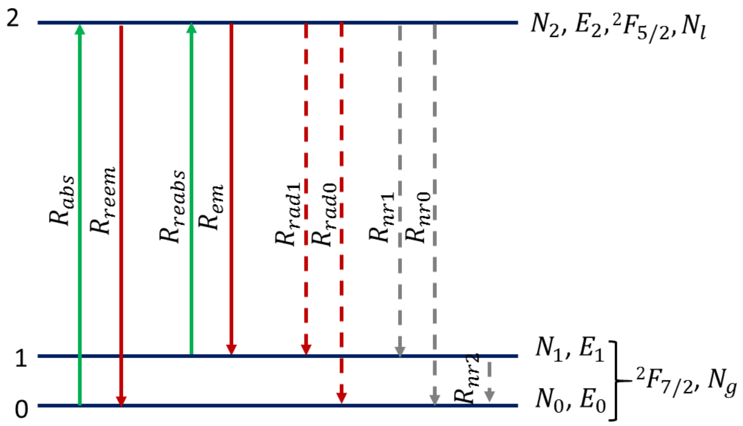

Figure E.2 Schematic of quasi-three level system of Yb^{3+}

In the diagram, N_2, N_1, and N_0 are the population of states in level 2,1 and 0; E_2, E_1 and E_0 are the energy of level 2, 1 and 0; R_{abs} and R_{reem} correspond to the absorption rate and the re-emission rate of the pump light; R_{em} and R_{reabs} represent the emission rate and re-absorption rate of the signal light; R_{rad1} and R_{rad0} are the radiative decay rate from level 2 to level 1 and 0, respectively; R_{nr2}, R_{nr1} and R_{nr0} are the non-radiative decay rate between level 2, 1 and 0. In addition, we define the population in $^2F_{7/2}$ as N_g, which equals the sum of N_1, and N_0. The population in $^2F_{5/2}$ is N_l and $N_l = N_2$.

Therefore, the rate equations of this system can be written as follows:

$$\frac{dN_2}{dt} = R_{abs}N_0 - R_{reem}N_2 + R_{reabs}N_1 - R_{em}N_2 - R_{rad1}N_2 - R_{rad0}N_2 - R_{nr1}N_2$$

$$-R_{nr0}N_2 - R_{nr0}N_1 \qquad Eq.\mathrm{E}-1$$

$$\frac{dN_1}{dt} = -R_{reabs}N_1 + R_{em}N_2 + R_{rad1}N_2 + R_{nr1}N_2 - R_{nr0}N_1 \qquad Eq.\mathrm{E}-2$$

$$\frac{dN_0}{dt} = -R_{abs}N_0 + R_{reem}N_2 + R_{rad0}N_2 + R_{nr0}N_2 + R_{nr0}N_1 \qquad Eq.\mathrm{E}-3$$

$$N = N_0 + N_1 + N_2 = N_g + N_l \qquad Eq.\text{E} - 4$$

where N is the total number of dopants.

The rates used above are given as:

$$R_{abs} = \sigma_{02}\frac{I_p}{h\upsilon_p} \qquad Eq.\text{E} - 5$$

$$R_{reem} = \sigma_{20}\frac{I_p}{h\upsilon_p} \qquad Eq.\text{E} - 6$$

$$R_{em} = \sigma_{21}\frac{I_s}{h\upsilon_s} \qquad Eq.\text{E} - 7$$

$$R_{reabs} = \sigma_{12}\frac{I_s}{h\upsilon_s} \qquad Eq.\text{E} - 8$$

$$R_{rad1} = \frac{1}{\tau_{r21}} \qquad Eq.\text{E} - 9$$

$$R_{rad0} = \frac{1}{\tau_{r20}} \qquad Eq.\text{E} - 10$$

$$R_{nr2} = \frac{1}{\tau_{nr10}} \qquad Eq.\text{E} - 11$$

$$R_{nr1} = \frac{1}{\tau_{nr21}} \qquad Eq.\text{E} - 12$$

$$R_{nr0} = \frac{1}{\tau_{nr20}} \qquad Eq.\text{E} - 13$$

where σ_{ij} is the transition cross section for the transition from level i to level j; h is the Plank's constant; ν_p is the frequency of the pump source, ν_s is the frequency of the signal (i.e. the emission generated from level 2 to level 1); I_p is the optical intensity of the pump, I_s is the optical intensity of the signal; τ_{rij} and τ_{nrij} are the radiative and non-radiative decay time from the level i to level j , respectively.

By calculating the temporal integration of the equations, the temporal evolution of the populations for each involved energy levels can be obtained. However, in the equations, the transitions are not in the same time scales (e.g. fast process may in ns scale slow process may in µs scale). This fact forces one to use a small temporal step size to ensure the accuracy of the solution of the rate equation. Owing to the existence of slow processes, the temporal evolution must be calculated over a long time span. As a result, it is inefficient to directly calculate the rate equations to get the population in steady-state.

An alternative way to calculate the steady-state populations is to assume the system is already under steady-state and derive the rate equations. Before doing this, several factors need to be introduced to reduce the complexity of the equation.

Because of the level 0 and level 1 belong to ${}^2F_{7/2}$ manifold, by introducing fraction factors f_0 for level 0 and f_1 for level 1, the relationship between N_1, N_0 and N_g is given by:

$$N_1 = f_1 N_g \qquad Eq.\text{E} - 14$$

$$N_0 = f_0 N_g \qquad Eq.\mathrm{E}-15$$

$$f_1 + f_0 = 1 \qquad Eq.\mathrm{E}-16$$

By considering the fraction factor of the stark levels, the transition cross section for the two stark level can be related to the absorption and emission cross section for pump and signal wavelengths by the relationships:

$$\sigma_{02} f_0 = \sigma_{ap} \qquad Eq.\mathrm{E}-17$$

$$\sigma_{12} f_1 = \sigma_{as} \qquad Eq.\mathrm{E}-18$$

$$\sigma_{20} = \sigma_{ep} \qquad Eq.\mathrm{E}-19$$

$$\sigma_{21} = \sigma_{es} \qquad Eq.\mathrm{E}-20$$

where σ_{ap} and σ_{as} is the absorption cross section of the pump and signal, respectively; σ_{ep} and σ_{es} is the emission cross section of the pump and signal, respectively.

In addition, the rate of spontaneous radiative decay R_{rad} and non-radiative decay R_{nr} between the two manifolds can be calculated by:

$$R_{rad} = R_{rad1} + R_{rad0} \qquad Eq.\mathrm{E}-21$$

$$R_{nr} = R_{nr1} + R_{nr0} \qquad Eq.\mathrm{E}-22$$

Using Eq. E-5 to Eq. E-22, the rate equations can be simplified to:

$$\begin{aligned}\frac{dN_g}{dt} &= -\left(\sigma_{ap}\frac{I_p}{h\upsilon_p} + \sigma_{as}\frac{I_s}{h\upsilon_s}\right)N_g \\ &\quad + \left(\sigma_{ep}\frac{I_p}{h\upsilon_p} + \sigma_{es}\frac{I_s}{h\upsilon_s} + R_{rad} + R_{nr}\right)N_l \qquad Eq.\mathrm{E}-23\end{aligned}$$

$$\begin{aligned}\frac{dN_l}{dt} &= \left(\sigma_{ap}\frac{I_p}{h\upsilon_p} + \sigma_{as}\frac{I_s}{h\upsilon_s}\right)N_g \\ &\quad - \left(\sigma_{ep}\frac{I_p}{h\upsilon_p} + \sigma_{es}\frac{I_s}{h\upsilon_s} + R_{rad} + R_{nr}\right)N_l \qquad Eq.\mathrm{E}-24\end{aligned}$$

When the system is in steady-state, at each point of the gain medium,

$$\frac{dN_g}{dt} = \frac{dN_l}{dt} = 0 \qquad Eq.\mathrm{E}-25$$

Therefore, the ratio of the population in ${}^2F_{7/2}$ and ${}^2F_{5/2}$ manifolds can be derived:

$$\frac{N_l}{N_g} = \frac{\sigma_{ap}\frac{I_p}{h\upsilon_p} + \sigma_{as}\frac{I_s}{h\upsilon_s}}{\sigma_{ep}\frac{I_p}{h\upsilon_p} + \sigma_{es}\frac{I_s}{h\upsilon_s} + R_{rad} + R_{nr}} \qquad Eq.\mathrm{E}-26$$

Introducing a population inversion factor β between manifold $^2F_{5/2}$ and manifold $^2F_{7/2}$, we can express their populations relating to the total number of dopants by:

$$N_l = \beta N \qquad Eq.\mathrm{E}-27$$

$$N_g = (1-\beta)N \qquad Eq.\mathrm{E}-28$$

Using Eq.E-27 and Eq.E-28 in Eq.E-26 yields:

$$\beta = \frac{\sigma_{ap}\frac{I_p}{h\upsilon_p} + \sigma_{as}\frac{I_s}{h\upsilon_s}}{(\sigma_{ep}+\sigma_{ap})\frac{I_p}{h\upsilon_p} + (\sigma_{es}+\sigma_{as})\frac{I_s}{h\upsilon_s} + R_{rad} + R_{nr}} \qquad Eq.\mathrm{E}-29$$

Thus, for given pump and signal intensity, the population inversion factor under steady state can be calculated. By using this equation, we are able to build a mathematical model of the Yb doped sample in Matlab and subsequently compare the results with the simulation results obtained by commercial simulation software.